ISSN 0038-531X

*Russian Original Vol. 48, No. 3, March 1980*

September, 1980

SATEAZ 48(3) 153–222 (1980)

# SOVIET ATOMIC ENERGY

АТОМНАЯ ЭНЕРГИЯ
(ATOMNAYA ÉNERGIYA)

TRANSLATED FROM RUSSIAN

CONSULTANTS BUREAU, NEW YORK

# SOVIET ATOMIC ENERGY

*Soviet Atomic Energy* is a translation of *Atomnaya Energiya*, a publication of the Academy of Sciences of the USSR.

An agreement with the Copyright Agency of the USSR (VAAP) makes available both advance copies of the Russian journal and original glossy photographs and artwork. This serves to decrease the necessary time lag between publication of the original and publication of the translation and helps to improve the quality of the latter. The translation began with the first issue of the Russian journal.





Consultants Bureau journals appear about six months after the publication of the original Russian issue. For bibliographic accuracy, the English issue published by Consultants Bureau carries the same number and date as the original Russian from which it was translated. For example, a Russian issue published in December will appear in a Consultants Bureau English translation about the following June, but the translation issue will carry the December date. When ordering any volume or particular issue of a Consultants Bureau journal, please specify the date and, where applicable, the volume and issue numbers of the original Russian. The material you will receive will be a translation of that Russian volume or issue.

Subscription (2 volumes per year)

Vols. 46 & 47: $147.50 per volume (6 Issues)
Vols. 48 & 49: $167.50 per volume (6 Issues)

Single Issue: $50
Single Article: $7.50

Prices somewhat higher outside the United States.

**CONSULTANTS BUREAU, NEW YORK AND LONDON**

227 West 17th Street
New York, New York 10011

Published monthly. Second-class postage paid at Jamaica, New York 11431.

*Soviet Atomic Energy* is abstracted or indexed in *Chemical Abstracts, Chemical Titles, Pollution Abstracts, Science Research Abstracts, Parts A and B, Safety Science Abstracts Journal, Current Contents, Energy Research Abstracts,* and *Engineering Index.*

# SOVIET ATOMIC ENERGY

A translation of *Atomnaya Énergiya*

September, 1980

**Volume 48, Number 3** **March, 1980**

## CONTENTS

# CONTENTS

(continued)

Engl./Russ.



**The Russian press date (podpisano k pechati) of this issue was 2/25/1980. Publication therefore did not occur prior to this date, but must be assumed to have taken place reasonably soon thereafter.**

## ARTICLES

# TECHNOLOGY OF INCREASING THE QUALITY OF URANIUM ORE DURING EXTRACTION AND PRIMARY PROCESSING*

M. A. Temnikov

UDC 622.349.5:622.79

The expansion in nuclear power engineering calls for an increase in the extraction of uranium ore, and consequently in the productivity of mines. This has led to the use of a system for processing deposits involving mass methods of breaking down ores and completely working out the ores. The cost of hydrometallurgical processing of such ores is high, but it can be reduced by chemical concentration methods.

The present article examines the use of radiometry methods for increasing the quality of the ore during extraction and primary processing.

Figure 1 gives a scheme for checking the quality of the ore in systems involving selective and mass breakdown of the ore respectively. The roman numerals denote the radiometric methods for increasing the quality of the ore. These are based on hydrometallurgical processing.

Let us now examine each of these methods in greater detail:

We know that the gamma radiation from uranium ores can be used to determine the concentration of uranium directly in the ore body by a radiometric method. The method of determining the uranium content and power of mineralization at the outcrop of the ore is conventionally known as gamma sampling, in the same way that determination in cores and boreholes is known as core gamma sampling or gamma logging [4-6].

The gamma sampling of a shothole is used during selective cutting of ore and rock to determine the contours of the ore body. The holes are drilled at the points at which the samples are needed. Gamma sampling is carried out either by determining the difference in effect achieved by the use of special lead screens installed on the detectors of portable radiometers, or by the radiometers of a directional γ-radiation detector.

*A version specially written for this journal of a paper read at the MAGATE symposium on estimating reserves of uranium and mining techniques, Buenos Aires, 1-4 October, 1979.

TABLE 1. Experimental Data on the Sorting of the Same Ore Mass in Dumpers on Route to the Ore Chute and in Rail Wagons (RTS) after Leaving the Ore Chute

| Deposit | System of mining | Waste from sorting process, % | | Abs. inc. in tailings, % | Notes |
|---|---|---|---|---|---|
| | | stope (face) sorting | RTS | | |
| A | Horizontal bed, cutting downwards | 24,5 | 7,9 | 16,6 | Averaged data |
| | Substage stoping | 11,5 | 2,0 | 9,5 | The same |
| B | Substage and bed (partial) breakdown | 53,0 | 34,0 | 19,0 | Separate experiments |
| | | 4,2 | 1,7 | 2,5 | |
| | | 27,0 | 0,0 | 27,0 | |
| | | 17,3 | 10,8 | 6,5 | |
| | | 25,4 | 11,6 | 13,8 | Averaged data |

Translated from Atomnaya Énergiya, Vol. 48, No. 3, pp. 139-143, March, 1980. Original article submitted December 7, 1979.

0038-531X/80/4803-0153$07.50  

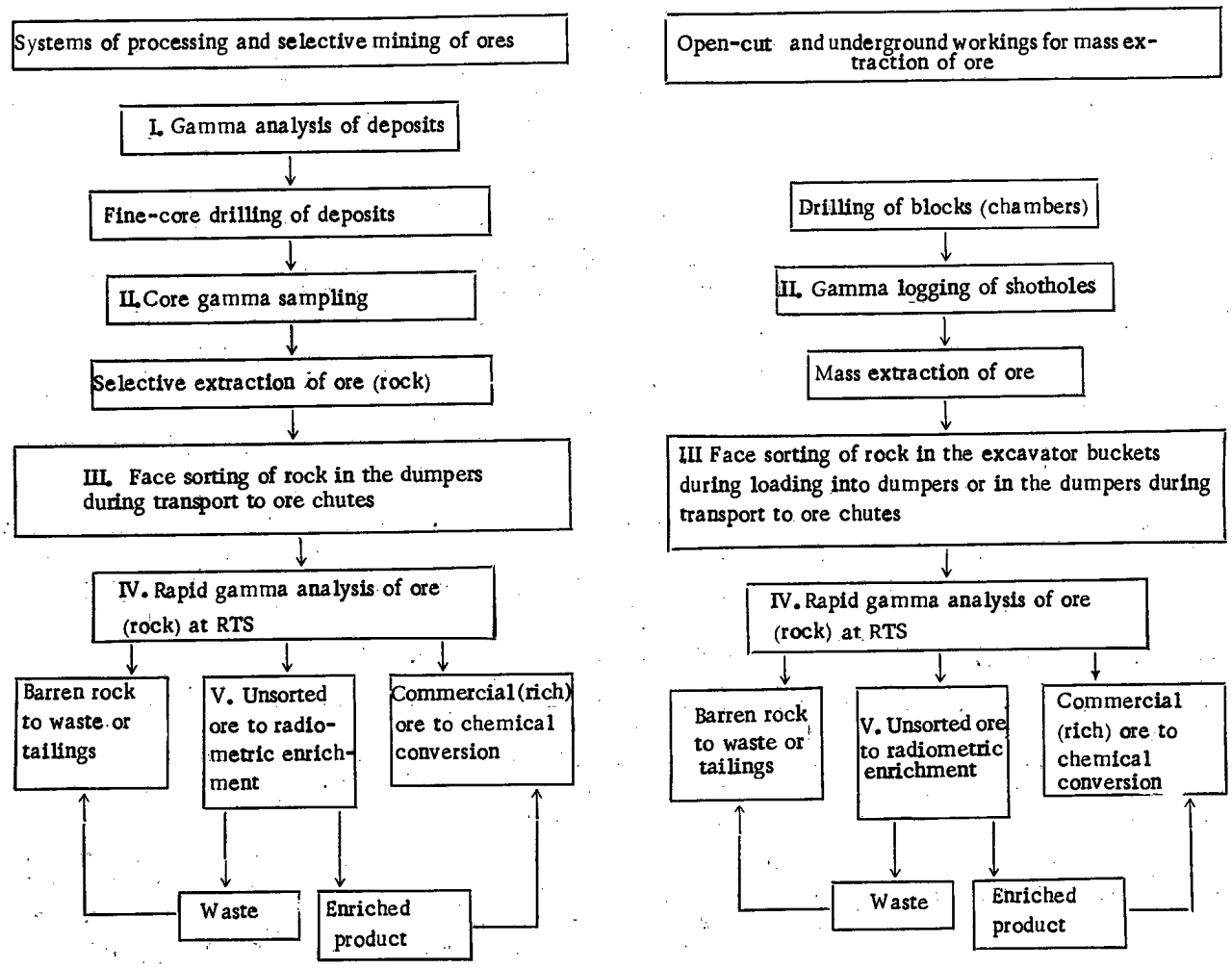


Fig. 1. Scheme for checking the quality of uranium ore during mining and primary processing (RTS: radiometric test station).

Shothole gamma sampling is used for the quantitative assessment of mineralization and for defining the boundaries of ore bodies, using the holes drilled for blasting. The shotholes are checked for the correct charge of explosive to ensure selective cutting of the rock.

The fact that the results are obtained directly at the measurement site, coupled with the simplicity and availability of the methods used, has ensured their widespread use as a means of increasing ore quality.

Gamma logging of holes is used during the development of deposits by systems that involve mass recovery of the ore. The shotholes are gamma logged prior to being charged with explosive, in order to define the boundaries of mineralization and to select the sites for

TABLE 2. Results of Tests on Various Types of Uranium Ore

| Type of ore | No. of containers meas. | Rel. error in analysis, % | | | |
|---|---|---|---|---|---|
| | | of whole ore batch | av. of individual analy. | max. individual analy. | |
| I | 59 | −0,7 | ±31,0 | +90,0 | −36,0 |
| II | 50 | +1,4 | ±23,0 | +72,0 | −31,4 |
| III | 137 | 0,0 | ±6,9 | +22,5 | −26,6 |
| IV | 85 | −5,1 | ±6,9 | +43,3 | −66,7 |
| V | 42 | −6,0 | ±22,7 | +38,5 | −62,3 |
| VI | 18 | +5,8 | ±22,4 | +91,3 | −36,9 |
| VII | 25 | +1,2 | ±24,0 | +36,0 | −43,8 |
| VIII | 7 | −1,8 | ±18,1 | +56,2 | −43,4 |

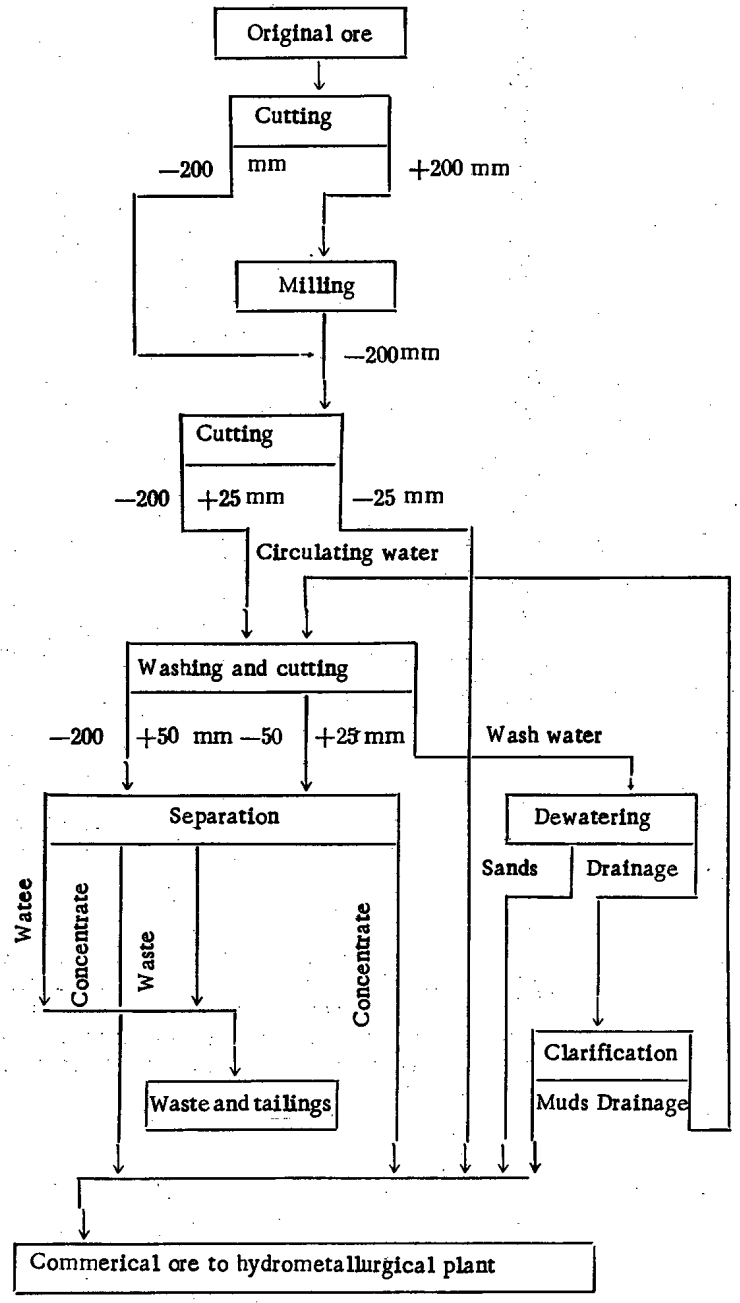


Fig. 2. Ore enrichment scheme.

the setting of charges. This enables one to carry out shot firing with minimum disturbance and mixing of the ore.

By gamma logging the holes and selectively cutting the rock and ore in a single deposit, we can achieve a considerable enrichment (18%) of the extracted ore in certain parts of the chamber, compared with bulk mining throughout the whole depth of the fold. Under these circumstances, the output of the unconditioned ore mass can be increased by a factor of 1.38.

Radiometric sorting of the extracted ore mass in the face, by taking measurements in the excavator buckets or in the dumpers, can be used as a means of primary enrichment of the ore. This technique is being rapidly developed, due to the use of large wagons, dump trucks, and rail dumper cars in uranium mines and quarries. Unfortunately, the radiometric contrast or the variation in the distribution of the radioactive component of the ore tends to fall with an increase in the size of the loads subject to sorting. At the same time, radiometric sorting of extracted ore at the stope in turn enables one to mine whole formations or just individual parts of the formations, or in certain cases to abandon unproductive systems of selective mining and change over to more productive systems of mass or semimass mining.

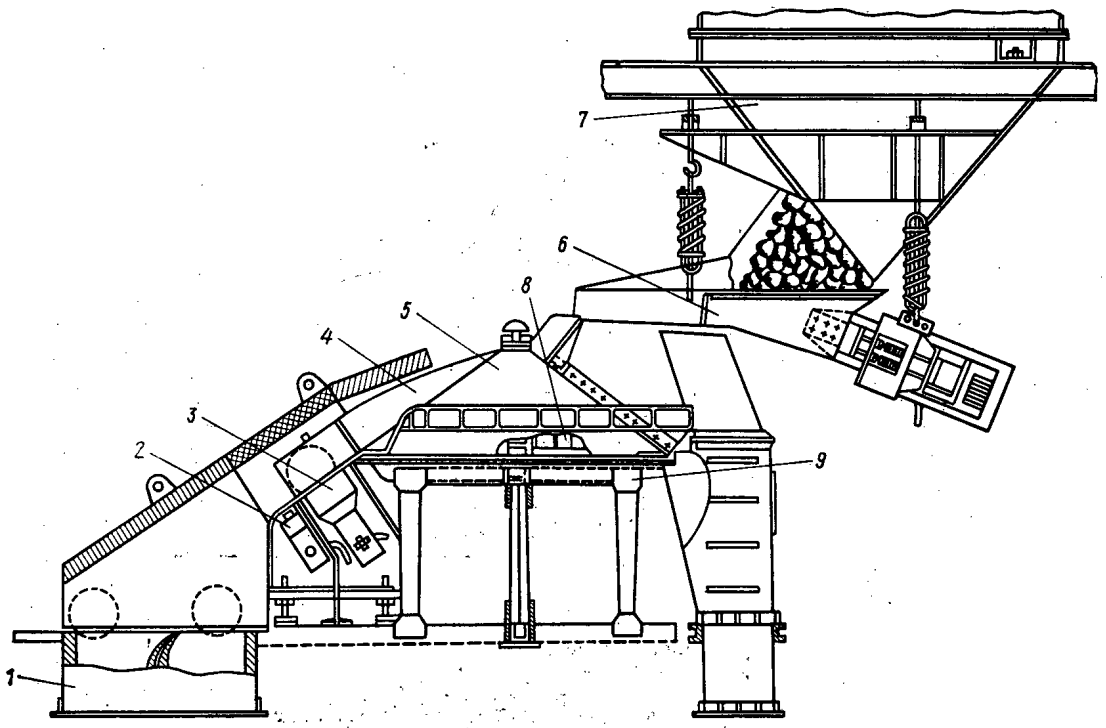


Fig. 3. "Granat" separator for sorting ore size −200+50 mm: 1) sorting hopper; 2) electropneumatic valve; 3) radiometer detector; 4) fixed spiral of conical pick-up feeder; 5) conical pick-up feeder; 6) vibro feed; 7) bunker; 8) drive to conical pick-up feeder; 9) frame of separator.

The extracted ore is sorted in the buckets of the excavators by means of special instruments, each consisting of a control board mounted in the cabin of the excavator and detectors with special shock absorbers mounted on the bucket and equipped with special protective screens made of steel and lead.

The following data serve to illustrate the effectiveness of bucket screening. The average depletion factor of ores in opencut workings was 25.1-31.0% prior to the introduction of bucket sorting (as high as 48% in certain blocks), with a standardized depletion of 20%. The introduction of bucket radiometric sorting enabled this to be reduced to 19.2% on an average, with a maximum of 22.8%.

As we have already noted, the output of tailings and the content of uranium in the commercial ore become lower as the mass of the sorted portion of ore deposit is increased, for a constant minimum workable content of uranium. For example, when a six (cubic) meter excavator bucket was replaced by four meter and three meter buckets on one quarry, the tailings of the sorting process increased by 3 and 5-5.5%, respectively. At the same time, the content of uranium in the ore increased by 3.3 and 5.7-6.0%, while the depletion factor fell by 2.9 and 5.2%, respectively.

Increasing the efficiency of the radiometric sorting in the excavator bucket in some cases facilitated a reduction in the height of the excavator berm. For example, drilling and blasting is carried out at a height of 15 m, while the ore is excavated in two or three subberms, i.e., at a height of 7.5 or 5 m.

In the case of underground uranium workings, the quality of the ore loaded in the dumpers is determined at the instant it is moved to the ore chute, with the aid of a radiometer mounted on the machine. The machine will then load the material in one chute or another, depending upon its quality (ore or waste). Stope or face sorting avoids the need to move the rock to the ore chute for measurement, acting virtually as a primary enrichment process for the extracted ore.

Table 1 gives experimental data on stope sorting prior to the ore being transported to the ore chute, together with rapid gamma analysis of the same ore mass after leaving the ore

chute. We can see from the table that radiometric sorting ahead of the ore chute leads to an increase in the tailings of 9.5-16.5%, which in turn leads to an increase of 8-15% in the uranium content of the ore.

Rapid gamma analysis of the rock in the transport containers (rail wagons, dumpers, etc.) has long been an integral part of ore processing for the rapid sampling of the ore mass as a whole. A high degree of accuracy in the sampling of the ore in wagons, and the possibility this offers of changing the content of the sorted rock being carried, enables us to treat the rapid ore analysis method as a primary method of ore enrichment, in much the same way as radiometric sorting. Radiometric test stations for rapid gamma analysis have been set up both underground and on the surface for sorting the extracted rock and for calculating the uranium content of the extracted ore. **Radiometric test stations are equipped** with special radiometers based on gas-discharge or scintillation counters [3, 4]. Where necessary, the stations are equipped with balances, and in recent years they have been furnished with equipment for recording analytical data on magnetic or punched tape, and with teletype machines for transmitting the data to a computer for processing.

The error in gamma analysis depends upon the uniformity in the distribution of the uranium throughout the ore, the dimensions of the portion of ore being analyzed, the state of radioactive equilibrium, the radon emission from the ore, the weather conditions, and other factors. It can reach a level of ±20-30% in individual analyses. However, the error in analyzing batches of ore does not exceed ±5-6% and satisfies the conditions for the chemical analysis of uranium ore [3] (Table 2).

Where there is no provision for face or stope analysis at the mine, its function can be taken over by the radiometric test station, generally by testing the whole of the extracted rock. The quantity of waste that is generated by this method of sorting comprizes from 0 to 34% (see Table 1).

Consequently, the use of radiometric methods as part of the ore processing cycle of the mine and the use of various types of electronic apparatus lead to a significant primary enrichment of the ore, either during the blasting operation or during the transport of the extracted ore.

This type of sorting operation is carried out prior to chemical refining operations and more thorough sorting or radiometric separation (enrichment) of the industrial ore is carried out on radiometric test stations at a radiometric enrichment plant [2]. Radiometric separation relies on the same properties of the uranium ore as are employed in gamma sampling and borehole logging, face sorting and rapid analysis of ore in the dumpers. For roughly half of the type of uranium ore, radiometric separation is not just a method of primary processing, it is the only method of mechanical enrichment employed. The advantages of this process lie in its cheapness, and also in the fact that it does not require milled ore, does not use reagents, requires very little electrical energy, and produces virtually no products that are harmful to the environment.

The most serious of the drawbacks to radiometric separation is the limited enrichment that is possible with low grade ores. For this reason, it is very important not to overreduce the ore when blasting and to strive for the range of sizes most suitable for separation: —150+30 mm.

The technology of radiometric separation has its own special features. Figure 2 gives the schematic of a radiometric enrichment plant. We can see from this that such plants involve the following main operations [1]:

1) reduction (this plays an insignificant role). The purpose of the reduction process is to ensure the maximum size of rock suitable for separation, usually not larger than 200-250 mm. Only the larger rocks (+200 mm) are crushed;

2) screening, which is one of the basic preparatory operations for separating the unsorted fines (particles below 15 mm, for example) and dividing the sorted material into two or three "machine" size classes in order to eliminate any large differences in the weight of the rocks passing through the machines;

3) washing the machine classes to remove any radioactive mud coating the rocks. Otherwise, barren material would become radioactive and would not be rejected. Sometimes, the operations of screening and washing are combined, since they can be carried out on the same piece of apparatus;

4) the sorting of the "machine" classes, i.e., dividing them into concentrate (commercial ore) and waste, is carried out on ore-sorting machines known as radiometric separators. Despite the range of structural designs employed for this purpose, all separators have the following basic parts, used for the same purposes (Fig. 3):

a bunker outlet for ensuring an even flow of material from the bunker for sorting;

a vibratory feed with an electromagnetic drive;

a cone-shaped pick-up feeder with a fixed spiral for spreading out the rocks throughout the measurement zone;

a radiometer with scintillation counters and a count-resolving system, to provide a quantitative estimate of the content of radioactive component in the rock and to send a signal to the actuator;

an actuator (pneumatic valve or throttle) for mechanically segregating the rocks;

a sorting discharge hopper for accumulating the sorted material and passing it to the appropriate conveyer.

The throughput rate of the separators varies from 40 to 100 tonnes/h for the size class −200+50 mm, 10-15 tonnes/h for class −50+25 mm, and 4-5 tonnes/h for class −25+15 mm.

The radiometric enrichment plants in existance at the present time generate wastes of from 25 to 43% of the original ore, or from 50 to 80% of the sorted class, the output of which varies from 45.0 to 64.5% for the various types of ore. The content of uranium in the waste from the radiometric separators varies from 0.010 to 0.015%. Under these circumstances, the enrichment factor of the final product leaving the plant for chemical processing equals 1.25-1.64.

Consequently, the concept of increasing the quality of extracted uranium bearing ores by the widespread introduction of radiometric methods and instruments during the mining process itself and during primary processing of the ore enables us to increase the uranium content of the commercial ore that is passed on for chemical refining. This leads to a considerable reduction in the cost of the raw material for nuclear fuel.

LITERATURE CITED

1. A. I. Gorshkov et al., Proceedings of the MAGATE International Conference on Nuclear Power Engineering and Its Fuel Cycle, Salzburg, May 2-13, 1977, IAEA-CN-36/321.
2. V. A. Mokrousov et al., Theoretical Fundamentals of the Radiometric Enrichment of Radioactive Ores [in Russian], Nedra, Moscow (1968).
3. L. N. Posik et al., Radiometric Rapid Analysis of Extracted Ores [in Russian], Atomizdat, Moscow (1960).
4. M. I. Prutkina and V. L. Shashkin, Manual of Radiometric Surveying and Radiometric Analysis [in Russian], Atomizdat, Moscow (1975).
5. I. M. Tenenbaum, Fundamentals of Ore Radiometry [in Russian], Gosatomizdat, Moscow (1961).
6. V. L. Shashkin, Analyzing Radioactive Ores by Gamma Radiation [in Russian], Atomizdat, Moscow (1972).

# USING DETERMINATIONS OF PROTACTINIUM WHEN ASSESSING URANIUM SHOWINGS AT THE PROSPECTING STAGE*

G. N. Kotel'nikov and I. P. Shumilin

UDC 550.8.835

A group of uranium ores known to prospectors is formed by the leaching of uranium and radium from ore deposits and the subsequent deposition of these elements near to the surface. Showings of this type are often highly radioactive and conditioned at the outcrop, but tend to die away rapidly at depth. Such showings are known as "rootless," "insolated," "false," etc., and are difficult to diagnose at the surface. A great deal of time and material can go into the mining of such deposits before they are found to be commercially useless.

In certain geochemical settings connected with processes of hypergenesis, we observe intensive transport of uranium and radium in the outcrops of conditioned ore bodies. In such cases, weak anomalies only are maintained at the surface, while analysis shows a balanced concentration of uranium, which does not correspond to the real content in the primary ores. This group of showings is most often passed over or classed as noncommercial, particularly during small-scale surveys. At best, they tend to be mined as a last resort.

The features of prospecting and methods of assessing anomalies in which there is a loss of equilibrium between uranium and radium have been described in [1], but these methods are not always suitable for the showing that presently concerns us. An efficient method of primary assessment of showings, based on the complex determination of protactinium, uranium, and radium in samples taken over the anomalies is recommended.

The nuclide $^{231}Pa$ is a product of the decay of $^{235}U$ and is found in company with it in a definite ratio. The halflife of $^{231}Pa$ is $3.248 \cdot 10^4$ yr. Protactinium has a considerably lower migration capacity than uranium or radium and is retained better at the outcrop of the ore body, even under intense conditions of hypergenesis. This allows us to use it as a "datum" and employ it to determine the intensity and direction of the transport of uranium and radium. The directivity of the migration processes (acquisition and transport) is an important factor when assessing showings and deciding whether or not to mine a particular deposit.

All the variety of features of the various uranium showings reduce in the final analysis to three types of uranium—protactinium ratios (see Table 1), which characterize the direction and intensity of the migratory processes and also govern their preliminary assessment.

In showings of the first type, where U/Pa is equal to or close to unity, we see a weak transport of uranium and radium. Surveys of this type of showing have indicated that the uranium contents at the surface and at deep horizons are roughly the same, and that the mineralization represents the primary minerals of uranium: pitchblende, coffinite, etc. The second type of showing is characterized by the prevalence of uranium over protactinium ($U/Pa > 1$), which indicates an intensive acquisition of uranium. In this case, the content of uranium at deeper horizons is lower than at the surface, and frequently approximates to a Clarke distribution. The uranium mineralization is represented by colored secondary minerals. In showings of the third type, the content of protactinium is considerably higher than the uranium content ($U/Pa < 1$), which indicates an intensive transport of uranium into the surface parts of the showing and a high content of uranium in the primary ores. The content of uranium in boreholes and workings at deep horizons is several times greater than at the surface. The uranium mineralization is either absent altogether in the hypergenesis zone or takes the form of traces of secondary minerals.

*A version adapted for this journal of a paper read at the MAGATE symposium on assessing uranium resources and mining techniques, Buenos Aires, October 1-4, 1979.

Translated from Atomnaya Énergiya, Vol. 48, No. 3, pp. 144-145, March, 1980. Original article submitted June 4, 1978.

0038-531X/80/4803-0159$07.50 

TABLE 1. Radiological Features of Showings in Relation to the Direction of Migration of Radioactive Elements

| Type of showing | Content of radioactive elements, % | | | U/Pa | Ra/Pa | Ra/U |
|---|---|---|---|---|---|---|
| | U | Pa | Ra | | | |
| I | 0,070 | 0,075 | 0,060 | 0,93 | 0,80 | 0,86 |
| II | 0,07 | 0,05 | 0,08 | 1,40 | 1,60 | 1,15 |
| III | 0,05 | 0,17 | 0,08 | 0,29 | 0,47 | 1,6 |

Note. The contents of protactinum and radium are given in units of equilibrium with uranium.

The results we have obtained give us reason to recommend the determination of protactinium in all anomalies observed during prospecting, in order to assess the uranium content in the primary ores up to the point at which they are disrupted at the outcrop. The proposed method of assessing uranium showings during the prospecting stage has been made possible by the development by I. P. Shumilin of a radiometric method and the necessary transducers for rapid analysis of samples of uranium, radium, radon, protactinium, and thorium (the determination of potassium is also possible) [2, 3].

The analyses can be carried out on standard commercially available apparatus. The transducer takes the form of a crystal of NaI(Tl) measuring 100 × 100 or 80 × 60 mm on which six β counters type STS-6 are arranged in two or three rows, with additional removable filters 0.2 g/cm$^2$ in density. The milled samples, weighing from 20 to 150 g, are measured in one cuvette (or alteratively several cuvettes, to increase the accuracy of the β measurements), 120 cm$^2$ in area, in layers that are intermediate or saturated for β-radiation. The measurements are conducted simultaneously through six channels.

The uranium is determined from the high energy β-radiation, while the radon is determined by means of the total γ-radiation with a discrimination threshold of 300 keV. The protactinium is determined in two parts of the spectrum: in the energy ranges 82 and 270 keV, which enables us to duplicate the protactinium analyses. The radiation of Ra is determined in the energy region 186 keV, while that of thorium is determined in the 2620 keV region. On the basis of such measurements, we have compiled a system of six equations and determined U, Ra, Rn, Pa (two results), and Th. To increase the accuracy of the analyses, we can raise the temperature of the samples to 800-1000°C. Under these conditions, the samples lose about 90% of their radon, and the intensity of the radiation from the radon, whose presence has an adverse effect on the analysis, is reduced by an order of magnitude. The analysis as a whole occupies a period of 10-15 min.

LITERATURE CITED

1. G. N. Kotel'nikov, At. Energ., 24, No. 6, 154 (1968).
2. I. P. Shumilin, At. Energ., 37, No. 5, 384 (1974).
3. I. P. Shumilin, Second All-Union Conference on the Chemistry of Uranium [in Russian], Nauka, Moscow (1978), p. 130.

# PROBLEMS OF DIAGNOSTICS OF PHYSICAL CHARACTERISTICS OF RBMK REACTORS ACCORDING TO NEUTRON NOISE

B. A. Vorontsov, I. Ya. Emel'yanov,
L. N. Podlazov, V. D. Rogova,
V. I. Ryabov, and B. M. Svecharevskii

UDC 621.039.562:621.039.514

The operation of high-capacity atomic power plants requires that the physical and dynamic characteristics of the reactor be monitored not only in the stage of start-up and entry into steady-state recharging conditions but also throughout the entire period of operation. The latter is due in particular to the fact that rapid advances in the fabrication of fuel elements make it possible to improve the technical and economic characteristics of reactors already in service. The final assessment of the effect of such measures on the characteristics of an atomic power plant should be made through full-scale tests.

In experimental studies of power reactors the principal of minimal changes in their operating conditions is most important. It is therefore advisable and promising to introduce into the practice of operational tests statistical methods excluding interference in the operating conditions of the atomic power plant. One such method is based on analysis of the neutron power, whose noise contains information about practically all processes and properties of the reactor [1]. The literature contains information about the use of analysis of neutron noise from power reactors to predict resonant instability [2], to diagnose vibrations and displacements of elements of the reactor construction [3, 4], etc.

In the present paper on the basis of experimental and computational-theoretical investigations we substantiate the possibility and the promise of using statistical methods for operational monitoring and diagnosis of changes in the steam coefficient of reactivity of reactors of the RBMK type under the conditions of commercial operation.

Formulation of the Problem. In a qualitative examination of the oscillograms of the neutron power (Fig. 1) of the RBMK-1000 reactor of the first unit of the Leningrad Atomic Power Plant it was found that the character of these fluctuations changed with entry into the steady-state recharging conditions along with the change in the reactivity coefficients and some dynamic characteristics of the reactor. This was the basis for studies on the pertinent quantitative relations. The method of solving this problem was refined after preliminary analysis of the autocorrelation functions (ACF) of the neutron noise, which were obtained in special experiments.

Description of the Experiment. From the measuring part of the regular control and safety system (CSS) the neutron-noise signal, being the relative deviation of the neutron power from the prescribed value, was fed into two recorders: a sensitive electronic recording potentiometer and a magnetograph. The use of a multichannel magnetograph enhanced the quality of the record and simplified the processing of the experimental information; at the same time, the noise of some other thermohydraulic parameters of the reactor installation was recorded in parallel. The experiments were performed with steady-state operation of the reactor at 85% nominal power. A study was made of the effect of the operation of the automatic pressure (APR) and level (ALR) regulators in drum separators (DS) on the spectrum of neutron noise. As a result, we obtained a series of realizations for the following modes of operation: all regulators switched on (nominal mode of operation); only the APR switched off; only the ALR switched off.

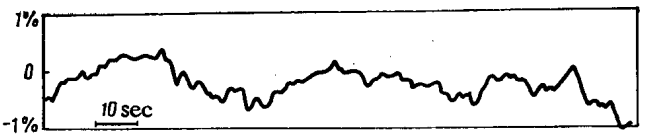


Fig. 1. Fluctuations of neutron power of RBMK-1000.

Translated from Atomnaya Énergiya, Vol. 48, No. 3, pp. 145-148, March, 1980. Original article submitted July 24, 1978.

0038-531X/80/4803-0161$07.50  

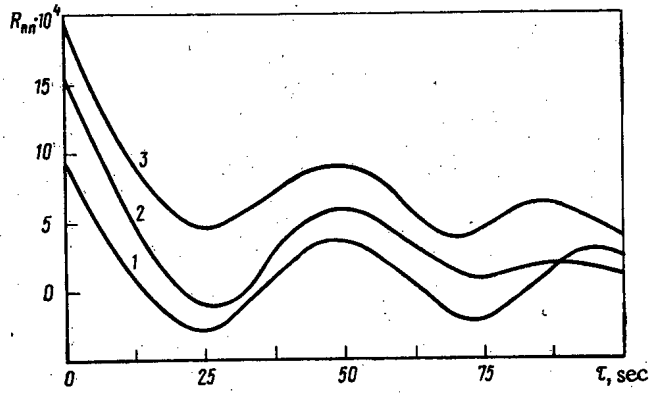


Fig. 2

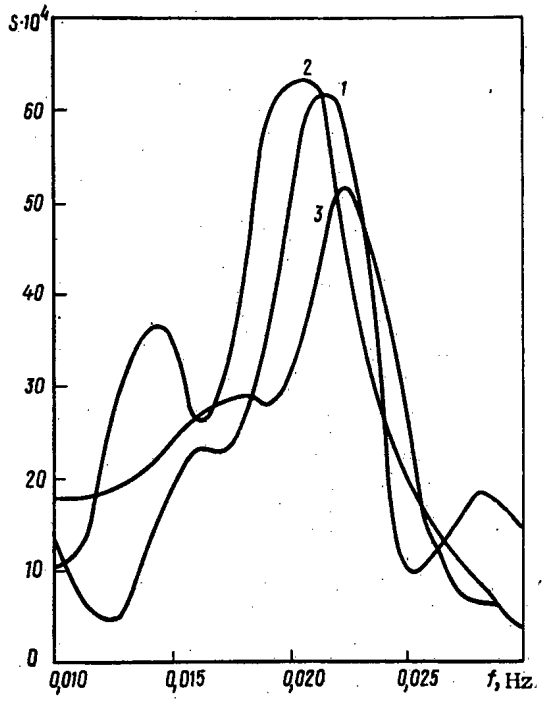


Fig. 3

Fig. 2. ACF of neutron noise: 1) all regulators switched on; 2, 3) APR and ALR, respectively, switched off.

Fig. 3. Spectral density S of neutron noise (same notation).

Computational and Theoretical Analysis and Discussion of Results. The mathematical processing of the data was carried out on a electronic computer according to a special program for calculating the ACF, the spectral densities (SD), and other statistical characteristics.

Figures 2 and 3 show the experimental ACF and SD of the neutron power for the three operating modes indicated. The ACF is in a form similar to the exponential—sinusoidal relation which is characteristic of processes excited by a wideband input signal when the object has resonant properties [1]. The cosine component implies periodicity in the signal of the neutron-power noise. The form of the ACF depends weakly on the conditions of the experiment. These features are traced in the resonance peak of spectral characteristics in the frequency region 0.021-0.022 Hz. It can also be concluded from the data of Fig. 3 that the resonance at 0.021-0.022 Hz reflects the internal resonance properties of the reactor plant.

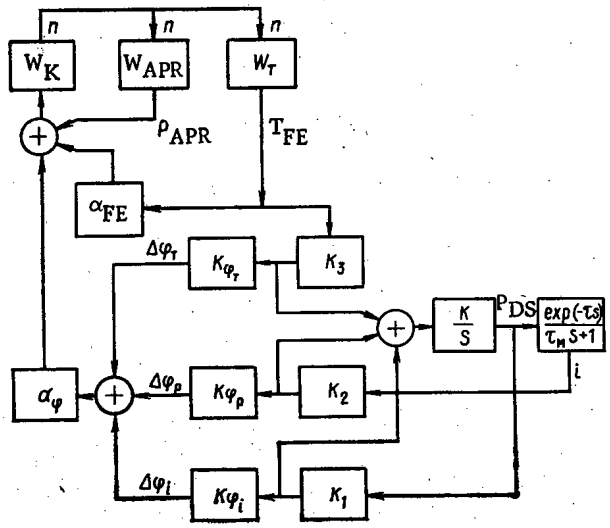


Fig. 4. Block diagram of transfer functions of RBMK-1000.

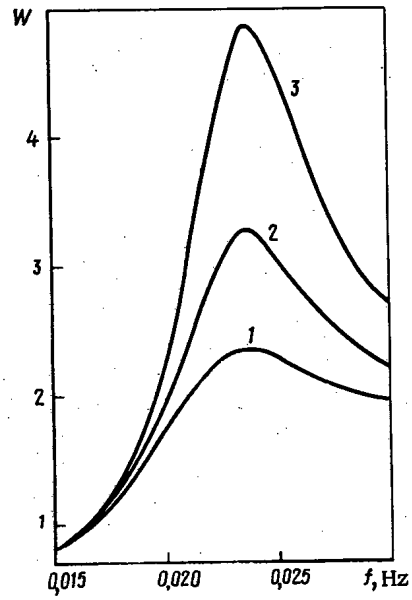


Fig. 5

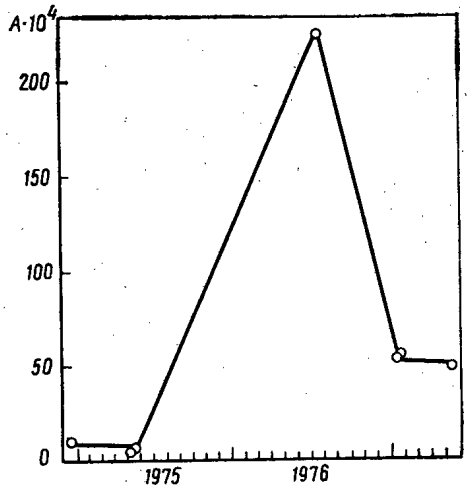


Fig. 6

Fig. 5. AFC of reactor plant for $\alpha_\varphi/\alpha_{FE} = -6.4$ (1), $-12.8$ (2), and $-19.2$ (3). ($\alpha_\varphi$ is the change in reactivity per percent steam content; $\alpha_{FE}$, the change in reactivity per degree change in fuel-element temperature.)

Fig. 6. Change in characteristic resonance during operating run of first reactor of Leningrad Atomic Power Plant (0 — experiment).

To confirm these conclusions we studied the amplitude-frequency characteristics (AFC) of a model of the reactor plant (Fig. 4). The system of automatic thermal controls of the APR and the ALR was not taken into account in the model. The following notation has been adopted in Fig. 4:

The symbol n is the deviation of the neutron power; $W_K = \left(1 - \sum_{i=1}^{6} \frac{a_i\lambda_i}{s+\lambda_i}\right)^{-1}$, the transfer function of the reactor kinetics with the assumption that $\ell dn/dt = 0$; $W_{APR} = -q(A)/s$, the transfer function of the automatic power regulator (APR); q(A), the coefficient of harmonic linearization; $W_T = \lambda_T/(s+\lambda_T)$, the transfer function of the change in the temperature gradient from the fuel elements to the coolant; $\lambda_T$, the inverse time constant of the change in the thermal power of the reactor; $\rho_{APR}$, the relative reactivity of the APR; $T_{FE}$, the dimensionless deviation of the thermal flux from the fuel elements to the coolant; $K_1$, $K_2$, $K_3$, coefficients determining the change in the steam flow rate under a change in the pressure, initial enthalpy, and thermal power of the reactor; $K\varphi_T$, $K\varphi_p$, $K\varphi_i$, coefficients determining the change in the steam content as the result of a change in the thermal power of the reactor, the pressure in the DS, and the initial enthalpy; $\Delta\varphi_T$, $\Delta\varphi_p$, $\Delta\varphi_i$, the changes in the steam content as the result of a change in the thermal power, pressure in the DS, and the initial enthalpy; K, the gain of the pressure-change transfer function; $\tau_M$, the time constant of the smearing of the temperature front in the circulation loop; $\tau$, the transport delay in the circulation loop; $\alpha_{FE}$, $\alpha_\varphi$, the reactivity according to the fuel-element temperature and the steam content; $P_{DC}$, the deviation of the pressure in the DS; and i, the deviation of the initial enthalpy.

It is seen from the block diagram of Fig. 4 that in the range of frequencies studied a change in the reactor reactivity occurs primarily because of a change in the fuel temperature and the steam content, the change in the latter being associated with a change in the thermal power (positive relation*), a change in the pressure in the DS (negative relation*) and a change in the initial enthalpy with a corresponding transport delay (positive relation*). Each process has its phase shifts and gains, and this is why resonance peaks appear in the AFC of the reactor.

*With positive $\alpha_\varphi$.

Periodic measurements during an operating run of the RBMK indicated a small change in $\alpha_{FE}$ and a substantial change in $\alpha_\varphi$. Therefore, in order to ascertain the effect of the physical characteristics of the reactor core on the AFC it was sufficient to change $\alpha_\varphi$ in the calculations. From Fig. 5, which presents some of the results of the calculations, it is seen that at 0.023 Hz there is a resonance, which is in good agreement with experimental data. It is also seen that the amplitude of the resonance increases as $\alpha_\varphi$ grows. It thus follows that in the real spectral densities of neutron noise, recorded at various times during the RBMK operating run, the resonance at these frequencies should also increase as $\alpha_\varphi$ grows.

Figure 6 shows the change in the amplitude of the resonance as found by processing neutron noise recorded at various times during the operating run of the reactor. The maximum in this plot corresponds to the state of the reactor with the highest value of $\alpha_\varphi$. The subsequent decrease in the amplitude of the resonance corresponds to a new state of the reactor core after modernization of the charge.

Thus, experimental (see Fig. 6) and computational and theoretical (see Fig. 5) data indicate that the parameters of the resonance of the spectral characteristic of the neutron noise of the RBMK-1000 at frequencies of 0.021-0.022 Hz can be conveniently used to diagnose changes in the physical and dynamic characteristics of a reactor. And on the basis of the well known relation $S_i/S_0 = |W_i|^2/|W_0|^2$, with the assumption that the perturbing action is of an unchanged character, it is possible to make a quantitative estimate of the change in $\alpha_\varphi$ at any i-th moment in the operating run if at some moment, labeled by a zero subscript, a neutron-noise spectral density $S_0$ was measured with known properties of the reactor core, i.e., in fact, with a known reactor transfer function $W_0$.

Conclusion. Studies of the neutron noise of the RBMK-1000 can be made on the basis of the existing regular CSS equipment. In studying the neutron noise it was revealed that in the frequency range 0.021-0.022 Hz the spectral characteristic displays a resonance whose amplitude depends essentially on the steam coefficient of reactivity; this makes it possible to use analysis of neutron noise to monitor and diagnose changes in the steam coefficient of reactivity of reactors of the RBMK type during normal operation. At the same time, it was established that for analysis of neutron noise in the RBMK-1000 in the frequency range indicated one can use a simplified model of the dynamics of the reactor plant.

LITERATURE CITED

1. R. E. Uhrig, Statistical Methods in Nuclear Reactor Physics [Russian translation], Atomizdat, Moscow (1974).
2. V. A. Afanas'ev et al., At. Energ., 24, No. 4, 363 (1968).
3. J. Robinson and R. Kryter, Trans. Am. Nucl. Soc., 24, 413 (1976).
4. M. Mathis et al., Trans. Am. Nucl. Soc., 23, 466 (1976).

# COMPARISON OF CERTAIN METHODS OF CALCULATING NEUTRON FLUXES IN A REACTOR FUEL CHANNEL

Yu. P. Elagin, A. S. Il'yashenko,
V. A. Lyul'ka, T. S. Poveshchenko,
and N. V. Sultanov

UDC 621.039.51.12:539.125.52

The complex of programs being developed for the detailed calculation of RBMK reactors must provide for the rapid and sufficiently accurate calculation of the neutron flux averaged over a cell of a fuel channel (FC). This problem can be solved in various ways. In the present article we investigate the surface pseudosources method (SPM) in the $G_N$ approximation with the reduction of the channel to cylindrical geometry, the SPM in the $G_N^P$ approximation, the first collision probability method (FCPM), and the generalized first collision probability method (GFCPM).

These methods are compared with the Monte-Carlo method. In addition to accuracy the machine time necessary in the various methods is also taken into account. With this in mind the following problems were treated in the one-group approximation:

1. The problem of a unit unidirectional flux of neutrons incident on the outer boundary of a FC with no internal sources; neutrons emerging from the channel are not returned.

2. Problems of a source of specified constant strength inside the FC; neutrons emerging from the channel are not returned;

3. Problems of a source of specified constant strength inside the FC; neutrons are specularly reflected inward from the outer boundary of the channel.

In these variants it is required to determine the average neutron fluxes in zones into which the FC is divided. By a FC we mean the reactor channel itself plus an adjoining layer of graphite a few centimeters thick (Fig. 1). The FC is divided into several zones with $\rho_2 = 0.9$ cm, $\rho_3 = 2.3$ cm, and $\rho_4 = 3.78$ cm; the numbers 2, 3, and 4 refer to circles counting from the center of the channel. The graphite is also divided into two or four regions by concentric circles.

Surface Pseudosources Method in the $C_N$ Approximation. In this method a calculation is first made for a two-zone cylindrical microcell consisting of the fuel element and a surrounding layer of water with an outside radius determined in the Wigner—Seitz approximation by the expression

TABLE 1. Comparison of Average Neutron Fluxes in a RBMK FC with External Sources

| Zone No. | Material | $\rho_{out}$ or $\rho_c$, cm | $\Sigma_t$, cm$^{-1}$ | $\Sigma_a$, cm$^{-1}$ | $\frac{\bar{\Phi}-\bar{\Phi}_{MC}}{\bar{\Phi}_{MC}}\cdot 100\%$ | | $\bar{\Phi}_{MC}$ (anisotropic source) | $\frac{\bar{\Phi}-\bar{\Phi}_{MC}}{\bar{\Phi}_{MC}}\cdot 100\%$ | | $\bar{\Phi}_{MC}$ (isotropic source) |
|---|---|---|---|---|---|---|---|---|---|---|
| | | | | | MGG3 | $G_3^1$ | | FCPM | GFCPM | |
| 1 | Zr | 0,75 | 0,3485 | 0,0085 | −7,5 | −3 | 1,34 (1±1,3·10$^{-2}$) | +0,8 | −3,4 | 1,32 (1±1,3·10$^{-2}$) |
| 2 | $H_2O$ | 2,3 | 2,1318 | 0,0075 | −4,5 | −0,6 | 1,52 (1±0,6·10$^{-2}$) | +0,7 | −2,0 | 1,51 (1±0,6·10$^{-2}$) |
| | $UO_2$ | 1,6 | 0,6114 | 0,2455 | −2,5 | −0,8 | 1,34 (1±0,7·10$^{-2}$) | +3,5 | −0,9 | 1,33 (1±0,7·10$^{-2}$) |
| 3 | $H_2O$ | 4,0 | 2,1318 | 0,0075 | +1,3 | +0,3 | 3,08 (1±0,3·10$^{-2}$) | +0,3 | −1,0 | 3,06 (1±0,3·10$^{-2}$) |
| | $UO_2$ | 3,09 | 0,6114 | 0,2455 | +0,42 | +0,2 | 2,36 (1±0,3·10$^{-2}$) | −1,7 | +0,3 | 2,35 (1±0,3·10$^{-2}$) |
| 4 | Zr | 4,4 | 0,3485 | 0,0085 | +0,43 | +0,2 | 4,64 (1±0,3·10$^{-2}$) | −3,5 | −1,0 | 4,59 (1±0,3·10$^{-2}$) |
| 5 | C | 5,4 | 0,3809 | 0,0002 | +0,39 | +1,2 | 5,10 (1±0,2·10$^{-2}$) | −3,7 | −1,2 | 5,07 (1±0,2·10$^{-2}$) |
| 6 | C | 6,4 | 0,3809 | 0,0002 | +0,70 | +1,2 | 5,60 (1±0,2·10$^{-2}$) | −3,2 | −1,2 | 5,68 (1±0,1·10$^{-2}$) |
| 7 | C | 7,7 | 0,3809 | 0,0002 | +0,33 | +0,30 | 6,09 (1±0,2·10$^{-2}$) | −3,1 | −1,3 | 6,06 (1±0,2·10$^{-2}$) |
| 8 | C | 9,0 | 0,3809 | 0,0002 | +0,80 | +1,1 | 6,47 (1±0,1·10$^{-2}$) | −3,0 | −0,8 | 6,49 (1±0,2·10$^{-2}$) |

Translated from Atomnaya Énergiya, Vol. 48, No. 3, pp. 148-151, March, 1980. Original article submitted March 26, 1979.

0038-531X/80/4803-0165$07.50  

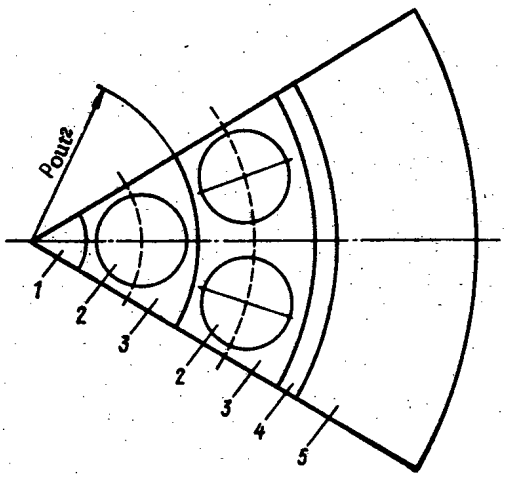


Fig. 1. One sixth of a RBMK fuel channel; 1) zirconium rod; 2) water or steam-water mixture; 3) fuel element; 4) zirconium tube; 5) graphite; ---) radii of centers of fuel slugs of first and second rows.

$$R^M = \sqrt{\frac{\rho_3^2 - \rho_2^2}{6}} = \sqrt{\frac{\rho_4^2 - \rho_3^2}{12}},$$

where $\rho_2$ and $\rho_3$ are respectively the inside and outside radii of the homogenized zone (Fig. 1), and the superscript M characterizes quantities referring to the microcell.

The choice of neutron source in the calculation of a microcell depends on the model problem. For problem 1 a unit difference current of incoming neutrons is specified on the outer boundary of the microcell for the "sink at infinity" boundary condition [1]. For problem 2 uniform volume sources of unit strength are specified in water with diffuse reflection at the outer boundary of the microcell. Diffuse reflection is achieved by introducing an additional zone with a large total cross section and a small absorption cross section. From microcell calculations performed by the PRAKTINETs 3F program [2], the disadvantage factor $d = \Phi^M_{H_2O}/\Phi^M_{UO_2}$ and the macroscopic cross section of the homogenized annular zone containing the fuel elements are determined by the expression*

$$\Sigma^g_{a(s)} = \frac{\int_V \Sigma^M_{a(s)} \Phi^M(r)\, dr}{\int_V \Phi^M(r)\, dr}. \qquad (2)$$

Here superscript g indicates the homogenized value. A macrocell is also calculated by the PRAKTINETs 3F program.

Average neutron fluxes over the microcell in the homogenized region were determined by using the disadvantage factors d and the balance condition

$$\Sigma^M_{a_{UO_2}} V^M_{UO_2} \overline{\Phi}^M_{UO_2} + \Sigma^M_{a_{H_2O}} V^M_{H_2O} \overline{\Phi}^M_{H_2O} = \Sigma^g_a V^g \overline{\Phi}^g. \qquad (3)$$

Surface Pseudosources Method in the $G_N{}^P$ Approximation. The development of the surface pseudosources method for determining neutron distributions in complex two-dimensional cells was reported in [3]. Using the algorithm obtained, N. V. Sultanov wrote a PRAKTINEK program [3] for calculating neutron fluxes averaged over zones of a FC in the $G_N{}^P$ approximation; N is the number of spherical harmonics; and P, the number of axial harmonics.

First-Collision-Probability Method. It has frequently been pointed out in the literature [4, 5] that the FCPM is a fruitful method of calculating the spatial and angular distributions of neutrons in a lattice of a heterogeneous reactor. The calculation of $P_{ij}$, the

*This method of averaging can lead to an appreciable error for $\Sigma_s{}^g$, but this does not have a large effect on the final result.

TABLE 2. Comparison of Average Neutron Fluxes in a FC of a RBMK Reactor with Internal Sources

| Zone No. | Material | $\rho_{out}$ or $\rho_c$, cm | $\Sigma_t$, $cm^{-1}$ | $\Sigma_a$, $cm^{-1}$ | $q_v$, $cm^{-3}$ | $\frac{\bar{\Phi}-\bar{\Phi}_{MC}}{\bar{\Phi}_{MC}}\cdot 100\%$ | | | $\bar{\Phi}_{MC}$ | $\frac{\bar{\Phi}-\bar{\Phi}_{MC}}{\bar{\Phi}_{MC}}\cdot 100\%$ | | $\bar{\Phi}^*_{MC}$ |
|---|---|---|---|---|---|---|---|---|---|---|---|---|
| | | | | | | $G_3^1$ | FCPM | GFCPM | | MGG3 | $G_3^1$ | |
| 1 | Zr | 0,75 | 0,3475 | 0,0075 | 0,00755 | 0,4 | —10,2 | —1,4 | 0,137 $(1\pm1{,}9\cdot10^{-2})$ | —0,1 | —1,0 | 0,103 $(1\pm2{,}8\cdot10^{-2})$ |
| 2 | $H_2O$ | 2,3 | 1,434 | 0,0102 | 0,8196 | 0,2 | —3,4 | —1,4 | 0,144 $(1\pm0{,}8\cdot10^{-2})$ | —1,8 | —0,6 | 0,112 $(1\pm1{,}2\cdot10^{-2})$ |
| | $UO_2$ | 1,6 | 0,6708 | 0,3233 | 0 | 0,0 | —0,8 | —0,6 | 0,114 $(1\pm0{,}8\cdot10^{-2})$ | —0,8 | 0,4 | 0,0905 $(1\pm1{,}2\cdot10^{-2})$ |
| 3 | $H_2O$ | 4,0 | 1,434 | 0,0102 | 0,8196 | —0,7 | 0,0 | —0,7 | 0,140 $(1\pm0{,}5\cdot10^{-2})$ | 1,9 | 0,0 | 0,157 $(1\pm0{,}8\cdot10^{-2})$ |
| | $UO_2$ | 3,09 | 0,6708 | 0,3233 | 0 | 0,0 | 0,0 | 0,0 | 0,112 $(1\pm0{,}6\cdot10^{-2})$ | 0,7 | —0,2 | 0,1210 $(1\pm0{,}7\cdot10^{-2})$ |
| 4 | Zr | 4,4 | 0,3475 | 0,0075 | 0,0075 | 1,1 | 0,0 | 0,8 | 0,125 $(1\pm0{,}7\cdot10^{-2})$ | —0,0 | —0,2 | 0,197 $(1\pm1{,}0\cdot10^{-2})$ |
| 5 | C | 6,4 | 0,4 | 0,0003 | 0,0636 | 0,9 | —1,8 | 0,0 | 0,109 $(1\pm0{,}6\cdot10^{-2})$ | 0,4 | 1,4 | 0,214 $(1\pm0{,}8\cdot10^{-2})$ |
| 6 | C | 9,0 | 0,4 | 0,0003 | 0,0636 | 0,75 | —1,2 | —1,5 | 0,0665 $(1\pm0{,}5\cdot10^{-2})$ | 0,9 | 0,4 | 0,233 $(1\pm1{,}0\cdot10^{-2})$ |

*Closed channel.

probability of a neutron created in zone i from a uniform isotropic source experiencing its first collision in zone j, plays a fundamental role in this method. Unfortunately, the approximate version of the FCPM, the so-called method of geometrical characteristics, cannot be applied directly to an actual FC since it was developed only for two-component (moderator-fuel) media, and a FC has a more complex structure involving at least three components. Therefore, $P_{ij}$ must be calculated by the exact method using double integrals,* and this increases the computation time. The calculations were performed by V. A. Lyu'lka and Yu. P. Elagin.

Generalized First-Collision-Probability Method. In this method the flux is expanded in a set of orthogonal polynomials in Cartesian coordinates. We present the results of calculations performed by T. S. Poveshchenko using the generalized first-collision-probability method in the linear approximation; the neutron flux in a zone is represented by a linear function of the x and y coordinates.

Monte-Carlo Method. In principle, high accuracy can be achieved with this method (e.g. [4]). Therefore, we take the results obtained by A. S. Il'yashenko using the results of the Monte-Carlo method as bench marks.

Results of Calculations. The accuracy of neutron flux averages over zones of a FC calculated by various methods was determined by comparison with the same averages calculated by the Monte-Carlo method. The first calculation was for a channel with neutrons entering from the outside. In calculations by the surface pseudosources method in the $G_N^P$ approximation and the $G_N$ approximation with the reduction of the FC to cylindrical geometry, the neutrons entering the cell through the outer boundary had a linearly anisotropic angular distribution with an anisotropic fraction of 7.25%. In calculations with the ordinary and generalized first collision probability methods the angular distribution of the neutrons entering the cell was isotropic. The calculations with the Monte-Carlo method were made with both angular distributions of the entering neutrons.

The input data and calculated results are listed in Table 1, where $\bar{\Phi}_{MC}$ is the average neutron flux calculated by the Monte-Carlo method. In order to compare results the calculations were normalized to the same number of neutrons absorbed in the channel per unit time. This variant of the calculation is the most complicated because of the large gradient of the neutron flux toward the center. Therefore, we discuss it in more detail.

In the calculation by the surface pseudosources method in the $G_3$ approximation with the reduction of the FC to cylindrical geometry (we denote it as the MGG3 approximation) the channel was divided into zones as shown in Fig. 1. The fluxes were averaged over the zones by the expression

$$\bar{\Phi} = \int \Delta\Phi dV/\Delta V. \qquad (4)$$

*The integral is triple, but the inner integral is tabulated beforehand.

In all zones the approximate neutron fluxes differ from the bench mark values by ∿1% except in the central rod (−7.5%) and the water zone adjoining the first row of fuel slugs (−4.5%).

The division into zones for calculations by the surface pseudosources method in the $G_3$ approximation is shown in Table 1. The error of the calculation is ∿1% (3% in the central zone). In the FCPM the FC is divided into zones as shown in Fig. 1, but each fuel element and the water surrounding it are further divided into two parts (dashed curves). Thus, the channel is divided into 16 zones. The maximum error of the calculation is ∿3%. In the GFCPM the FC is divided into zones as shown in Fig. 1, i.e. into 12 zones. The accuracy of the calculation of the neutron flux in the fuel elements is somewhat better than in the FCPM with division into 16 zones.

In the second stage of comparison of the accuracy of the approximate methods a calculation was made of a channel with internal neutron sources. The calculations were normalized to one neutron absorbed in the channel. The input data and results of the calculations are listed in Table 2.

In order to compare the results of the SPM calculation in the $G_N^P$ approximation, the FCPM, and GFCPM with bench-mark values, a channel was chosen with a vacuum outside it. These boundary conditions were established exactly in all the methods considered except in the SPM where at the outer boundary of the channel the integrated current of incoming neutrons from the FCPM calculation was specified. The neutron source density in zones of the channel was assumed proportional to the slowing-down power of the medium $\xi\Sigma_s$. The error of the SPM calculation in the $G_3^1$ approximation and the GFCPM was 1%; the FCPM has the same error except in the average neutron flux in the first and second zones where there is a systematic underestimation of the flux by ∿10%.

SPM calculations with the reduction of the FC to cylindrical geometry and in the $G_N^P$ approximation were compared with the bench mark value by calculating a "closed" channel, i.e. a channel with internal neutron sources and zero neutron current at the outer boundary of the channel.

The results of calculations in the $G_3^1$ approximation differ from the accurate values by 1%; the calculations in the $G_3$ approximation also differ by 1% except for water zones where the flux differs by 1.9%.

The values presented show that the SPM with the reduction of the channel to cylindrical geometry requires considerably less machine time and is not far inferior in accuracy to the SPM in the $G_3^1$ approximation and to the GFCPM.

The computation times of a FC of a RBMK on a BÉSM-6 computer by the MGG3, $G_3^1$, FCPM, and GFCPM are 3, 30, and 90 sec, and 4 min; by the Monte-Carlo method the times are 2 h for variant a and 15 min for variant b.

## LITERATURE CITED

1. N. I. Laletin, in: Methods of Calculating Thermal Neutron Distributions in Reactor Lattices [in Russian], Atomizdat, Moscow (1974), p. 238.
2. N. V. Sultanov, Preprint IAÉ-2143, IAÉ-2144, Moscow (1971).
3. N. I. Laletin and N. V. Sultanov, At. Energ., 46, 148 (1979); N. V. Sultanov, Preprint IAÉ-3005, Moscow (1978).
4. I. M. Sobol, The Monte Carlo Method, Univ. of Chicago Press (1975).

# CALCULATION OF EFFECTIVE BOUNDARY CONDITION AT THE SURFACE OF A MULTIREGION CYLINDRICAL SLUG

B. P. Kochurov

UDC 539.125.52:621.039.51.12

In heterogeneous reactor theory [1] the effective boundary condition at the surface of a slug is specified in terms of the thermal constant

$$\gamma = 2\pi D\rho \left[\partial N(\rho)/\partial\rho\right]/N(\rho), \tag{1}$$

where D is the neutron diffusion coefficient in the moderator, $\rho$ is the radius of the slug, and $N(\rho)$ is the asymptotic neutron flux in the moderator extrapolated at the surface of the slug. Many papers have been devoted to the calculation of $\gamma$ or the related quantity $\Gamma$:

$$\Gamma = N(\rho)/l\left[\partial N(\rho)/\partial\rho\right] = 2\pi D\rho/l\gamma \tag{2}$$

based on various methods of neutron transport theory and applying mainly to one-region slugs in an infinite moderator, generally assumed not to absorb neutrons [2, 3]. A more detailed bibliography can be found in [4].

We consider the calculation of $\Gamma$ for a multiregion cylindrical slug, based on a numerical solution of the integral neutron transport equation [5], specifically in a finite cell.

Suppose the slug is located in an infinite moderator. Assuming isotropic scattering, or in the transport approximation, the neutron flux in the one-velocity theory satisfies the integral equation

$$HN = 0; \quad H = 1 - L;$$
$$LN = \int K(\mathbf{r}, \mathbf{r}')\,\Sigma_s(\mathbf{r}')\,N(\mathbf{r}')\,d\mathbf{r}'. \tag{3}$$

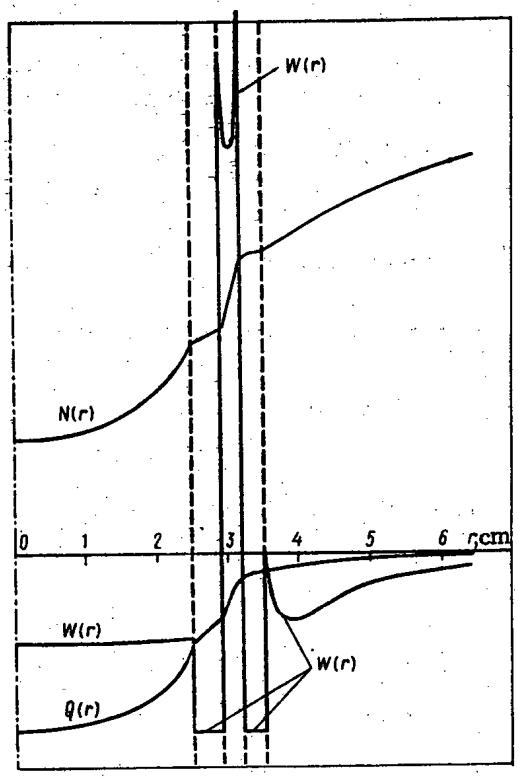


Fig. 1. Distribution of neutron flux N (r), the source Q (r), and the weight function W (r). The moderator is 8.4 cm thick.

Translated from Atomnaya Énergiya, Vol. 48, No. 3, pp. 151-153, March, 1980. Original article submitted April 2, 1979.

0038-531X/80/4803-0169$07.50 

TABLE 1. Effective Boundary Condition Γ of Black Slugs, Obtained by Using a Numerical Method and from Data in [4]

| a | c=0,9999 | | | c=0,99 | | | c=0,9 | | |
|---|---|---|---|---|---|---|---|---|---|
| | Γ | Γ [4] | δΓ, % | Γ | Γ [4] | δΓ, % | Γ | Γ [4] | δΓ, % |
| 0,1 | 1,2010 | 1,2058 | —0,40 | 1,2207 | 1,2216 | —0,07 | 1,3979 | 1,3856 | 0,89 |
| 0,2 | 1,1300 | 1,1362 | —0,55 | 1,1480 | 1,1502 | —0,19 | 1,3046 | 1,2951 | 0,74 |
| 0,3 | 1,0802 | 1,0858 | —0,52 | 1,0969 | 1,0985 | —0,15 | 1,2368 | 1,2284 | 0,68 |
| 0,5 | 1,0103 | 1,0149 | —0,46 | 1,0249 | 1,0255 | —0,06 | 1,1395 | 1,1336 | 0,52 |
| 0,7 | 0,9622 | 0,9662 | —0,42 | 0,9753 | 0,9755 | —0,02 | 1,0720 | 1,06851 | 0,33 |
| 1,0 | 0,9122 | 0,9159 | —0,41 | 0,9239 | 0,9237 | +0,02 | 1,0025 | 1,0016 | 0,09 |
| 2,0 | 0,8286 | 0,8318 | —0,39 | 0,8384 | 0,8374 | +0,12 | 0,8479 | 0,8459 | 0,15 |
| 5,0 | 0,7632 | 0,7623 | +0,12 | 0,7715 | 0,7664 | +0,67 | 0,8082 | 0,8062 | 0,36 |
| 8,0 | 0,7521 | 0,7429 | +1,24 | 0,7540 | 0,7466 | +0,99 | 0,7876 | 0,7836 | 0,52 |

Here $K(\mathbf{r}, \mathbf{r}') = \exp(-\tilde{\Sigma}R)/4\pi R^2$; $R = |\mathbf{r} - \mathbf{r}'|$, $\tilde{\Sigma}R$ is the optical path between $\mathbf{r}$ and $\mathbf{r}'$. Let $H_0$ and $L_0$ be the corresponding operators for an infinite moderator:

$$L_0 N = \int K_0(\mathbf{r}, \mathbf{r}')\, \Sigma_s N(\mathbf{r}')\, d\mathbf{r}';$$
$$K_0(\mathbf{r}, \mathbf{r}') = \exp(-\Sigma R)/4\pi R^2, \tag{4}$$

where $\Sigma_S$ and $\Sigma$ are the scattering and total cross sections of the moderator.

The regular solution $N_0$ and the Green's function $G_0(\mathbf{r}, \mathbf{r}_0)$ for the operator $H_0$ are

$$H_0 N_0 = 0; \quad N_0 \equiv I_0(\varkappa r);$$
$$H_0 G_0(\mathbf{r}, \mathbf{r}_0) = \delta(\mathbf{r}, -\mathbf{r}_0), \tag{5}$$

where $\varkappa$ is a root of the equation (the asymptotic parameter)

$$(\Sigma_s/2\varkappa) \ln[(1 + \varkappa/\Sigma)/(1 - \varkappa/\Sigma)] = 1, \tag{6}$$

and the Green's function for large $|\mathbf{r} - \mathbf{r}_0|$ has the asymptotic representation

$$G_{0,ac}(\mathbf{r}, \mathbf{r}_0) = g(c, l) K_0(\varkappa|\mathbf{r} - \mathbf{r}_0|); \quad c = \Sigma_s/\Sigma;$$
$$l \equiv 1/\Sigma; \quad g(c, l) = \frac{\varkappa^2(1 - \varkappa^2 l^2)}{\pi(\varkappa^2 l^2 - 1 + c)}. \tag{7}$$

At large distances from the surface of the slug (more than one to two neutron mean free paths in the moderator) the azimuthally symmetric solution of Eq. (3) has the form

$$N_{ac}(\mathbf{r}) = A[I_0(\varkappa r) + uK_0(\varkappa r)], \tag{8}$$

where the parameter u is uniquely related to γ or Γ;

$$a/\Gamma = \frac{z[I_1(z) - uK_1(z)]}{I_0(z) + uK_0(z)}; \quad a \equiv \rho l; \quad z \equiv \varkappa\rho. \tag{9}$$

A closed functional expression can be obtained for the parameter u. Rewriting Eq. (3) in the form,

$$HN = H_0 N + (H - H_0) N = 0 \tag{10}$$

and using the Green's function, we find

$$N_{ac}(r) = g(c, l) K_0(\varkappa r) \int I_0(\varkappa r_0)(L - L_0) N d\mathbf{r}_0, \tag{11}$$

where the addition theorem for Bessel functions [1] has been applied to $K_0(\varkappa|\mathbf{r} - \mathbf{r}_0|)$. Comparing Eqs. (8) and (11), we obtain

$$u = [g(c, l)/A] \int I_0(\varkappa r_0)(L - L_0) N = [g(c, l)/A] \int (L^+ - L_0^+) I_0 N(\mathbf{r}_1)\, d\mathbf{r}_1. \tag{12}$$

Thus, u is found as a functional for the solution, determined by the weight

$$W(r) = [g(c, l)/A] \int [\Sigma(r) K(\mathbf{r}, \mathbf{r}_0) - \Sigma K_0(\mathbf{r}, \mathbf{r}_0)] I_0(\varkappa r_0)\, d\mathbf{r}_0, \tag{13}$$

in which the integration in Eq. (12) is extended over the slug and part of its neighborhood. The function W (r) is damped out exponentially at distances from the slug of the order of the neutron mean free path in the moderator.

TABLE 2. Parameters u and Γ of Two Four-Region Cylindrical Slugs ($\Delta_i$ is the layer thickness in cm)

| Variant | Char. of layers | i: 1 | 2 | 3 | 4 | moderator | u; Γ |
|---|---|---|---|---|---|---|---|
| 1 | $\Delta_i$ | 5,0 | 0,1 | 0,3 | 0,04 | | |
| | $\Sigma_i$ | 0,20 | 0,09 | $3\cdot10^{-5}$ | 0,09 | 0,4001 | −0,2385; 3,059 |
| | $\Sigma_{si}$ | 0,14 | 0,08 | $3\cdot10^{-5}$ | 0,08 | 0,4000 | |
| 2 | $\Delta_i$ | 2,5 | 0,4 | 0,3 | 0,3 | | |
| | $\Sigma_i$ | 0,50 | 0,01 | 2,0 | 0,01 | 0,4001 | −0,1830; 2,922 |
| | $\Sigma_{si}$ | 0,25 | 0,01 | 1,98 | 0,01 | 0,4000 | |

Equation (3) can be solved by transforming the regular part of the solution into a certain source. Let

$$N_0(r) = AI_0(\varkappa r) \tag{14}$$

be the regular solution, continued into the slug. We find the complete solution in the form

$$N(r) = N_0(r) + N_1(r). \tag{15}$$

We rewrite Eq. (3) in the form

$$H\hat{N} = \hat{H}N_1 + (H - H_0)N_0 = 0$$

or

$$N_1 = LN_1 + Q;\ Q \equiv (L - L_0)N_0, \tag{16}$$

where the source function Q is damped out exponentially in the moderator at distances from the slug of the order of a mean free path. How do we find u or Γ from the solution of the integral equation in a cell of finite dimensions? We surround the slug with a sufficiently thick layer of moderator, and seek the solution in the form (15), where

$$N_0(r) \equiv I_0(\varkappa r) \tag{17}$$

is the fixed regular part of the solution continued into the slug, and the operators in Eq. (16) are defined for a finite cell. Sufficiently far from the slug

$$N_{1,ac}(r) = uK_0(\varkappa r) + B[I_0(\varkappa r) + uK_0(\varkappa r)] = B\left[I_0(\varkappa r) + \frac{I_1(\varkappa R)}{K_1(\varkappa R)}K_0(\varkappa r)\right], \tag{18}$$

where the first term comes from the fixed regular part of the solution $N_0$ (17), and the term $\sim B$ is related to the finite size of the cell. The latter part of Eq. (18) follows from the vanishing of the diffusion current at the cell boundary R. The coefficient B can be found by requiring the least deviation of (18) from the numerical solution in a certain asymptotic region of the moderator. Then it follows from Eq. (18) that

$$u = \frac{BI_1(\varkappa R)/K_1(\varkappa R)}{1+B}. \tag{19}$$

Equation (12) can also be used for u with A = 1 + B representing the total amplitude of the regular solution in the present case.

Table 1 lists the calculated values of Γ for black slugs surrounded by a moderator which absorbs neutrons, obtained with a program for solving an integral equation in a finite cell [5]. The condition at the cell boundary indicated above is realized as a result of the location of an infinite scattering moderator in the region r > R. The highly accurate data of [4] presented here serve essentially as tests. In the calculations it was assumed that $\Sigma_{s1} = 100\ cm^{-1}$, $\Sigma_{ss1} = 0.001\ cm^{-1}$, $\Sigma = 1$, $c = \Sigma_s/\Sigma$, $\alpha = \rho\Sigma$. The moderator layer was 4-5 mfp thick.

Table 1 shows that the divergences from [4] are generally within ±0.5%. Table 2 lists the calculated values of u and Γ for two four-region slugs which can serve as tests, with an error of no more than ±1%.

Figure 1 shows the neutron flux N (r), the source Q (r), and the weight function W (r) for variant 2 of Table 2. The functions Q (r) and W (r) are exponentially damped out in the moderator at distances of the order of a neutron mean free path.

The author thanks A. D. Galanin for helpful comments.

LITERATURE CITED

1. A. D. Galanin, Thermal Reactor Theory, Pergamon, New York (1960).
2. B. Davison, Proc. Phys. Soc., 64A, 881 (1951).
3. D. F. Zaretskii and D. D. Odintsov, in: Reactor Engineering and Reactor Theory [in Russian], Vol. 5, Izd. Akad. Nauk SSSR (1955), p. 279.
4. A. Kavenoky, Nucl. Sci. Eng., 65, 514 (1978).
5. A. Ya. Burmistrov and B. P. Kochurov, Preprint ITEF-49, Moscow (1976).

# NEUTRON IMPORTANCE AND SENSITIVITY COEFFICIENTS IN ITERATION SYNTHESIS METHODS

A. M. Kuz'min, K. S. Rafaev, and V. V. Khromov

UDC 539.125.52:621.039.51.12

In the practice of neutron-physical calculations of reactors extensive use has been made of iteration synthesis methods in which the space—energy distribution of neutrons is presented as a product of functions, each of which depends on one variable. These methods include methods of conditional separation of variables [1] and methods of synthesis in the class of continuous functions [2]. These methods served as the basis for high-speed programs (18-4RZ-15 [3] and its up-to-date modification SINVAR, SYNHAX [4], etc.) which make it possible, with sufficient accuracy for optimization studies, to calculate the neutron distribution and to determine the physical characteristics in reactors of complex form.

However, the application of these methods in calculations from the formulas of perturbation theory and with automation of the search for the optimal reactor parameters (e.g., by the method of successive linearization [5]) was hindered by the lack of algorithms for the solution of the pertinent equations for the neutron importance. In the present paper within the framework of the methods mentioned we formulate equations for the neutron importance, describe an iteration scheme for solving these equations, and give the results of calculations of the sensitivity coefficients for a typical fast sodium reactor with oxide fuel. For simplicity, we confine ourselves to consideration of problems in which the neutron flux density $\Phi(x, y)$ depends on two variables (extension of the discussion to the case of a large number of variables does not entail any major difficulties). As follows from [1, 2], to find the distribution $\Phi(x, y)$ it is necessary to solve the system of nonlinear equations

$$\begin{aligned} -\hat{L}(\xi)\,\psi + \lambda\hat{Q}(\xi)\,\varphi = 0; \\ -\hat{L}(\eta)\,\psi + \lambda\hat{Q}(\eta)\,\psi = 0 \end{aligned} \tag{1}$$

for the auxiliary vector functions $\varphi(x)$ and $\psi(y)$, whose boundary values $\varphi_S$ and $\psi_S$ satisfy the conditions $\Gamma_1(\varphi_S) = 0$ and $\Gamma_2(\psi_S) = 0$. In the course of the solution there are the nonlinear transformations

$$\xi = \hat{P}(\psi); \quad \eta = \hat{S}(\varphi) \tag{2}$$

to the vector functions $\xi(y)$ and $\eta(x)$, on the basis of which the operators of Eq. (1) are constructed: $\hat{L}(\xi)$ and $\hat{L}(\xi)$, operators "kindred" to operator $\hat{L}$ of the neutron transport equation describing the spatial displacement, absorption, and scattering of neutrons, as well as $\hat{Q}(\xi)$ and $\hat{Q}(\eta)$, operators "kindred" to operator $\hat{Q}$ of the transport equation characterizing the creation of secondary neutrons. In this case $\lambda$ is the leading eigenvalue of the problem and is proportional to the neutron-multiplication factor $k_{eff}$ while the operators $\hat{L}(\xi)$, $\hat{L}(\eta)\hat{Q}(\xi)$, and $\hat{Q}(\eta)$ depend in a known way on the perturbation parameter u (the

Translated from Atomnaya Énergiya, Vol. 48, No. 3, pp. 154-157, March, 1980. Original article submitted July 13, 1979.

 0038-531X/80/4803-0172$07.50 

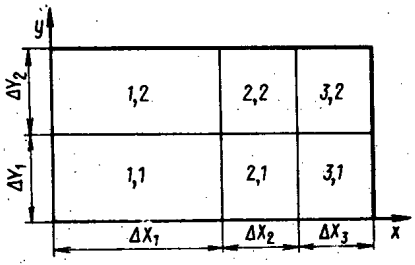


Fig. 1. Scheme of reactor:
$\Delta X_1 = 109{,}0$; $\Delta X_2 = 43{,}3$; $\Delta X_3 = 50{,}0$;
$\Delta Y_1 = 52.0$; and $\Delta Y_2 = 50.0$ cm.

concentration of any element, e.g., can be taken for such a parameter). The concrete form of these operators and the mappings $\hat{P}(\psi)$ and $\hat{S}(\varphi)$ were described in detail in the papers indicated above.

We shall assume that:

with a fixed value $u = u_0$ the eigenvalue $\lambda_0$ and the corresponding solutions $\varphi_0$ and $\psi_0$ are obtained;

in the proximity of the solution the products $\hat{M}_\xi(\xi_0)$; $\hat{M}_\eta(\eta_0)$; $\hat{P}_\psi(\psi_0)$; $\hat{S}_\varphi(\varphi_0)$; $\hat{M}_u(\xi_0)$; and $\hat{M}_u(\eta_0)$ are definite and continuous, so that

$$\hat{M}_\xi(\xi_0)\varphi_0 = -\frac{\partial \hat{L}(\xi_0)\varphi_0}{\partial \xi} + \lambda_0 \frac{\partial \hat{Q}(\xi_0)\varphi_0}{\partial \xi};$$

$$\hat{P}_\psi(\psi_0) = \frac{\partial \hat{P}(\psi_0)}{\partial \psi};\quad \hat{M}_\eta(\eta_0)\psi_0 = -\frac{\partial \hat{L}(\eta_0)\psi_0}{\partial \eta} + \lambda_0 \frac{\partial \hat{Q}(\eta_0)\psi_0}{\partial \eta};$$

$$\hat{S}_\varphi(\varphi_0) = \frac{\partial \hat{S}(\varphi_0)}{\partial \varphi};\quad \hat{M}_u(\xi_0)\varphi_0 = -\frac{\partial \hat{L}(\xi_0)\varphi_0}{\partial u} + \lambda_0 \frac{\partial \hat{Q}(\xi_0)\varphi_0}{\partial u};$$

$$\hat{M}_u(\eta_0)\psi_0 = -\frac{\partial \hat{L}(\eta_0)\psi_0}{\partial u} + \lambda_0 \frac{\partial Q(\eta_0)\psi_0}{\partial u};$$

there exist adjoint operators $\hat{L}^+(\xi_0)$, $\hat{Q}^+(\xi_0)$ and $L^+(\eta_0)$, $\hat{Q}^+(\eta_0)$ $\hat{Q}^+(\eta_0)$ in the class of functions $\varphi^+(x)$ and $\psi^+(y)$, respectively, which satisfy the adjoint boundary conditions $\Gamma_1^+(\varphi_S^+) = 0$ and $\Gamma_2^+(\psi_S^+) = 0$.

The orthogonality conditions

$$\{\hat{S}_\varphi(\varphi_0)\varphi_0\}_x = 0;\ \{\hat{P}_\psi(\psi_0)\psi_0\}_y = 0 \tag{3}$$

are satisfied; here, $\{\ \}_x$ and $\{\ \}_y$ denote the integration of the expression in braces over the range of variables x and y, respectively. The latter condition is easily verified with due account for the properties of transformation (2), as described in [1, 2].

Suppose that $u_0$ has changed by $\delta u$. A new eigenvalue $\lambda = \lambda_0 + \delta\lambda$ and new distributions $\varphi = \varphi_0 + \delta\varphi$ and $\psi = \psi_0 + \delta\psi$ correspond to the value $u = u_0 + \delta u$. As a result, any physical characteristic F, which is a functional of the neutron flux, experiences an increment $\delta F$. To obtain the perturbation theory relations associating $\delta F$ and $\delta u$, we employ discussions similar to those in [6]. In this case it is easily shown that to estimate the variation $\delta\lambda$ it is necessary to successively solve the adjoint equations

$$\begin{aligned} -\hat{L}^+(\eta_0)\psi_k^+ + \lambda_0\hat{Q}^+(\eta_0)\psi_k^+ &= -\hat{P}_\psi^+(\psi_0)\{\varphi_{k-1}^+, \hat{M}_\xi(\xi_0)\varphi_0\}_x; \\ -\hat{L}^+(\xi_0)\varphi_k^+ + \lambda_0\hat{Q}^+(\xi_0)\varphi_k^+ &= -\hat{S}_\varphi^+(\varphi_0)\{\psi_k^+, \hat{M}_\eta(\eta_0)\psi_0\}_y, \end{aligned} \tag{4}$$

where $k = 1, 2, \ldots$.

As the first approximation we can take the distribution $\varphi_0^+$ which satisfies the homogeneous equation

$$-\hat{L}^+(\xi_0)\varphi_0^+ + \lambda_0\hat{Q}^+(\xi_0)\varphi_0^+ = 0. \tag{5}$$

Solutions $\varphi_k^+$ and $\psi_k^+$ ($k = 1, 2, \ldots$) exist since by conditions (3) the equations

$$\{\psi_0, \hat{P}_\psi^+(\psi_0)\{\varphi_{k-1}^+, \hat{M}_\xi(\xi_0)\varphi_0\}_x\}_y = \{\varphi_0, \hat{S}_\varphi^+(\varphi_0)\{\psi_{k-1}^+, \hat{M}_\eta(\eta_0)\psi_0\}_y\}_x = 0$$

TABLE 1. Properties of Reactor Zones

| Cross section, $cm^{-1}$ | Zone No. | | | |
|---|---|---|---|---|
| | 1,1 | 1,2 and 2,2 | 2,1 | 3,1 and 3,2 |
| $\Sigma_{tr}$ | 0,2353 | 0,2548 | 0,2354 | 0,3119 |
| $10^2\Sigma$ | 0,5286 | 0,4123 | 0,5690 | 0,5555 |
| $10^2\nu\Sigma_f$ | 0,5610 | 0,1090 | 0,6781 | 0,1518 |

are satisfied and can be obtained by well-known methods [7]. It is of interest to use an iterationless scheme, described in [8], since the eigenvalue $\lambda_0$ is known.

If the iteration process (4) is truncated at the step of number k = n, we get

$$-\delta\lambda W = \{\varphi^+,\ \hat{M}_u(\xi_0)\,\varphi_0\delta u\}_x + \{\psi^+,\ \hat{M}_u(\eta_0)\,\psi_0\delta u\}_y + \Delta_n, \tag{6}$$

where

$$W = \{\varphi_0^+,\ \hat{Q}(\xi_0)\,\varphi_0\}_x;\quad \varphi^+ = \sum_{k=0}^{n-1}\varphi_k^+ + \alpha\varphi_n^+;\quad \psi^+ = \sum_{k=1}^{n}\psi_k^+;$$

$$\Delta_n = \alpha\{\delta\psi,\ \hat{P}_\psi^+(\psi_0)\{\varphi_n^+,\ \hat{M}_\xi(\xi_0)\,\varphi_0\}_x\}_y + (1-\alpha)\{\delta\varphi, \hat{S}_\varphi^+(\varphi_0)\{\psi_n^+,\ \hat{M}_\eta(\eta_0)\,\psi_0\}_y\}_x; \tag{6a}$$

where $\alpha = \begin{cases} 0 & \text{if the n-th iteration ended in the determination of } \psi_n^+; \\ 1 & \text{if the n-th iteration ended in the determination of } \varphi_n^+. \end{cases}$

The value of $\Delta_n$ characterizing the error of calculation of $\delta\lambda$ in the n-th approximation will be smaller the weaker the nonlinearity of the initial equations (1) and (2). It is also obvious that the final result (as $n\to\infty$) for $\delta\lambda$ should not change if the iteration process is begun by finding the solution $\psi_0^+$ of the homogeneous equation

$$-\hat{L}^+(\eta_0)\,\psi_0^+ + \lambda_0\hat{Q}^+(\eta_0)\,\psi_0^+ = 0,$$

having simultaneously changed the sequence in which the functions $\psi_k^+$ and $\varphi_k^+$ are found in each k-th step in the system (4) and in Eq. (6a).

To estimate the variation F of any linear-fractional functional $F(\varphi, \psi)$ of the neutron flux it is necessary to obtain the sequential solution of equations of the form of Eqs. (4), taking for the initial distributions the solutions of the inhomogeneous equations

$$-\hat{L}^+(\eta_0)\,\psi_0^+ + \lambda_0\hat{Q}^+(\eta_0)\,\psi_0^+ = -F_\psi(\varphi_0,\ \psi_0);$$

$$-\hat{L}^+(\xi_0)\,\varphi_0^+ + \lambda_0\hat{Q}^+(\xi_0)\,\varphi_0^+ = -F_\varphi(\varphi_0,\ \psi_0)\ -\hat{S}_\varphi^+(\varphi_0)\{\psi_0^+,\ \hat{M}_\eta(\eta_0)\,\psi_0\}_y, \tag{7}$$

where $F_\psi(\varphi_0, \psi_0)$ and $F_\varphi(\varphi_0, \psi_0)$ are the functional products in $\psi(y)$ and $\varphi(x)$, respectively, calculated for $u = u_0$; $\varphi = \varphi_0$ and $\psi = \psi_0$.

For simplicity we shall assume that the functional $F(\varphi, \psi)$ does not depend explicitly on the parameter u. Then for the variation $\delta F$ we get an expression of the same form as in the right-hand member of Eq. (6). In this case

$$\varphi^+ = \sum_{k=0}^{n-1}\varphi_k^+ + \alpha\varphi_n^+;\quad \psi^+ = \sum_{k=0}^{n}\psi_k^+.$$

By way of illustration of the efficacy of the schemes described for solving adjoint equations, we give some results obtained for a two-dimensional, cylindrical, multiple-zone reactor, symmetric about a central axis (x = 0) and the diametral plane (y = 0). The scheme

TABLE 2. Sensitivity Coefficients of Functionals $K_{eff}$ and $F_0$

| Sensitivity coefficient, $10^4$ cm | Calculation by perturbation-theory formulas (with $\Delta_n = 0$) | | | | | | Calculation from Eq. (8) |
|---|---|---|---|---|---|---|---|
| | n = 0 | | n = 1 | | n = 2 | n = 7 | |
| | α = 1 | α = 0 | α = 1 | α = 0 | α = 1 | α = 1 | |
| $L$ | −0,9727 | −0,9786 | −0,9804 | −0,9806 | −0,9809 | −0,9811 | −0,9817 |
| $L_0$ | 0,6667 | 3,8763 | 3,9601 | 3,9688 | 3,9816 | 3,9864 | 3,9869 |

of the reactor is given in Fig. 1 and the properties of the zones are given in Table 1. It is assumed that each zone of thickness $\Delta X_i$ ($i = 1, 2, 3$) and height $\Delta Y_j$ ($j = 1, 2$) is labeled by two subscripts (i, j) denoting, respectively, the number of the i-th radial layer and the j-th height layer of the reactor. For macroscopic cross sections of neutron interaction we introduced the following notation: $\Sigma$, absorption cross section; $\Sigma_{tr}$, transport cross section; $\nu\Sigma_f$, product of number $\nu$ of secondary neutrons and the fission cross section $\Sigma_f$.

The distribution of the density of neutron fluxes was calculated in the one-group diffusion approximation by the method of conditional separation of variables [1]. Within the framework of the modification of this method used, the components of the vector functions $\varphi(x)$ and $\psi(y)$ had the sense of neutron-flux distributions integrated over the thicknesses of the respective layers of the reactor. The components of the vector functions $\eta$ (or $\xi$), defined only on the boundaries of the zones with coordinates $x = X_i$ (or $y = Y_j$), are numerically equal to the ratio of one-sided neutron currents, obtained in the distributions $\varphi(x)$ [or $\psi(y)$], to the neutron fluxes integrated over the volumes of the adjacent reactor zones. In constructing the adjoint operators, for the initial equations (1) we took the finite-difference analogs of the respective equations of the method of conditional separation of variables.

Let us examine the convergence of the iteration schemes and the values of the variations for two functions F: $K_{eff}$, the effective coefficient of neutron multiplication, and $F_0$, the ratio of the integral neutron flux density in zone (2, 1) to the integral flux density in zone (1, 1). As the perturbation parameter u we take the absorption cross section $\Sigma$ for zone (1, 1). Calculations showed that iteration schemes of the form of Eq. (4) converge quite rapidly. For example, no more than 7 iterations were required ($n = 7$ and in each iteration two corrections $\psi_k^+$ and $\varphi_k^+$) in order that, with an accuracy of $\varepsilon = 10^{-5}$, there be simultaneous satisfaction of the inequalities

$$\{|\varphi_n^+|\}_x \leqslant \varepsilon \{|\sum_{k=0}^{n} \varphi_k^+|\}_x \text{ and } \{|\psi_n^+|\}_y \leqslant \varepsilon \{|\sum_{k=1}^{n} \psi_k^+|\}_y.$$

Let us note that the value $K_{eff} = 0.92985$, the corresponding distribution $\varphi_0(x)$, $\psi_0(y)$, $\varphi_0^+(x)$, and $\psi_0^+(x)$ and the value $F_0 = 0.63777$ were obtained with great accuracy since with iterative solution of the system (1) it was required to have satisfaction of the inequalities

$$|K_{i,j}^{(l)} - K_{i,j}^{(l-1)}| \leqslant \varepsilon |K_{i,j}^{(l)}|, \; i = 1, 2, 3; \; j = 1, 2,$$

where $K_{i,j}^{(l)}$ is the value of $K_{eff}$ in the $l$-th iteration, estimated by the functions integrated over zone (i, j). This was done with a view to excluding, as much as possible, the errors caused in the distributions $\varphi^+(x)$ and $\psi^+(y)$ by inaccuracies in our knowledge of the leading eigenvalue $\lambda_0 = 1/K_{eff}$ and the corresponding eigenfunctions.

In practical problems there is probably no need of a high accuracy in the calculation of functions $\varphi^+(x)$ and $\psi^+(y)$ since frequently the values of the variations of the functions ($\delta K_{eff}$, $\delta F_0$) and the coefficients of sensitivity $L = K_{eff}/\delta\Sigma$ and $L_0 = \delta F_0/\delta\Sigma$ rather than the importance distributions are of concern. Table 2 gives approximate values of the sensitivity coefficients, obtained by using relations of the form of Eq. (6) in which the remainder $\Delta_n$ is assumed to be zero. For comparison, Table 2 also gives values of the sensitivity coefficients found from

$$L = \frac{K_{eff}^+ - K_{eff}^-}{2\delta\Sigma}; \; L_0 = \frac{F_0^+ - F_0^-}{2\delta\Sigma}, \tag{8}$$

where $K_{eff}^+$, $F_0^+$ and $K_{eff}^-$ and $F_0^-$ are the "perturbed" values of the functionals $K_{eff}$ and $F_0$, found by solving Eqs. (1) for $\Sigma + \delta\Sigma$ and $\Sigma - \delta\Sigma$, respectively. In the calculations we assigned the increment $\delta\Sigma = 0.01\Sigma$. It is seen that the zeroth approximation ($n = 0$, $\alpha = 1$) of perturbation theory for L gives a relative error of less than 1%. To obtain roughly the same magnitude of error in estimating $L_0$ it is necessary to go over to calculation of the neutron importance in the first approximation ($n = 1$, $\alpha = 0$).

LITERATURE CITED

1. V. V. Khromov and A. M. Kuz'min, At. Energ., 21, No. 5, 406 (1966).
2. V. V. Khromov, in: Nuclear Reactor Physics. A Collection of Articles by the Moscow Engineering Physics Institute [in Russian], No. 3, Atomizdat, Moscow (1973), p. 5.

3. V. V. Khromov et al., in: Nuclear Reactor Physics. A Collection of Articles by Moscow Engineering Physics Institute [in Russian], No. 1, Atomizdat, Moscow (1968), p. 159.
4. V. A. Apse and V. V. Khromov, in: Nuclear Reactor Physics. A Collection of Articles by the Moscow Engineering Physics Institute [in Russian], No. 5, Atomizdat, Moscow (1977), p. 58.
5. V. V. Khromov, A. M. Kuz'min, and V. V. Orlov, Method of Successive Linearization in Problems of Optimization of Fast Reactors [in Russian], Atomizdat, Moscow (1978).
6. A. M. Kuz'min, in: Nuclear Reactor Physics [in Russian], No. 8, Atomizdat, Moscow (1979), p. 26.
7. L. N. Usachev, At. Energ., 15, No. 6, 472 (1963).
8. B. P. Kochurov, At. Energ., 35, No. 1, 52 (1973).

# PRODUCTION OF DEFECTS IN MOLYBDENUM BY A DEUTERIUM GLOW DISCHARGE PLASMA

V. N. Chernikov, G. A. Arutyunova, Yu. N. Sokurskii, and A. P. Zakharov

UDC 620.192:669.28

Processing in glow discharge plasmas is a powerful technique for working the surface structure of metals and modifying their properties [1, 2].

Cathode bombardment of polycrystalline molybdenum foils in a hydrogen glow discharge plasma is known [3] to lead to the formation of many dislocation loops in the volume of the foil and to the formation of regularly oriented surface dislocations. It was of vital importance to learn what type of loops are formed during bombardment and determine their character, that is, to find whether they are injection or subtraction loops.

## Experimental Technique

The foils which were to undergo bombardment and subsequent electron microscopy were prepared from a monocrystalline rod of molybdenum that had been doubly purified by electron beam zone melting. The rod axis formed an angle of about 5° with the [111] direction of the crystal lattice of the metal. The rod was cut perpendicular to its axis with an erosion-spark apparatus into wafers with a thickness of about 1.5 mm. The wafers were then polished on both sides to yield a thickness of 300-400 μm, and 3 mm-diameter discs were then cut from the wafers by the erosion-spark technique. The discs were then finely polished to a thickness of 200-250 μm. A standard "Tenupol" jet electropolishing apparatus with an electrolyte based on sulfuric acid and methyl alcohol (1:3) at a voltage of 15 V and a minimum electrolyte feed rate was then used to thin them electrolytically from both sides until a small hole appeared in the central region. In this way monocrystalline molybdenum foils with their [111] axes almost perpendicular to the plane of the foil were obtained.

Cathode bombardment was done in a diode-type discharge chamber mounted on an Edwards 306 pumping station, and spectrally pure deuterium was employed. The potential on the chamber electrodes was 500 V, the total current density was 4.5 mA/cm$^2$, the gas pressure was 1670 Pa, the temperature was 800°C, and the irradiation time was 30 min. The integrated dose was thus about $5 \cdot 10^{19}$ particles/cm$^2$. Upon completion of the processing in the plasma, the foils were examined with an EM-301G electron microscope with an accelerating voltage of 100 kV. The existence of a goniometer and a special sample holder made it possible to tilt the sample at angles of up to ±60° and rotate it azimuthally at angles of up to ±180°.

## Experimental Results

A microphotograph of a new foil is shown in Fig. 1a and a typical light-field microphotograph of a foil after irradiation in the plasma is shown in Fig. 1b. Structural defects in the form of loops and dark points are visible. The observed contrast is caused by lattice defects rather than by coherent inclusions formed with the participation of ex-

Translated from Atomnaya Énergiya, Vol. 48, No. 3, pp. 157-161, March, 1980. Original article submitted April 2, 1979; revision submitted November 30, 1979.

 0038-531X/80/4803-0176$07.50 

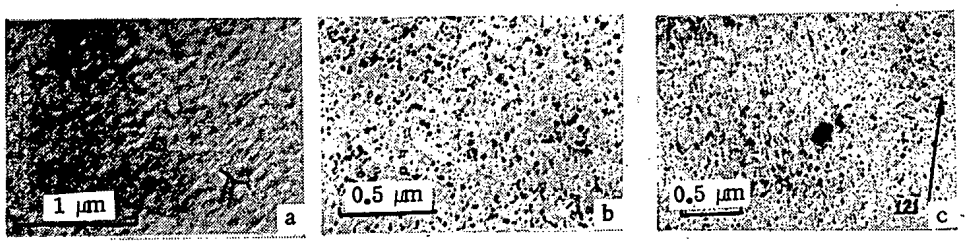


Fig. 1. Structure of an initial (a) and irradiated (b, c) monocrystalline foils of molybdenum (Fig. 1c shows a complete analysis of the dislocation loops).

**traneous atoms injected during irradiation.** A layer analysis of a massive sample by mass spectrometry of secondary ions demonstrated that deuterium was not present in greater than equilibrium amounts and, to judge from microdiffraction patterns, the irradiated foils did not contain new phases. A certain amount of broadening of the interference maxima and the appearance of a background in the electron diffraction patterns are quite natural for a crystal with a large number of defects [4].

The volume density of observed defects estimated for the volume of a 1000-Å-thick foil (1 Å = $10^{-10}$ m) is $6.5 \cdot 10^{15}$ $cm^{-3}$. If we assume that these defects are dislocation loops of a single type, then over the same volume they should contain $6 \cdot 10^{-3}$ at.% point defects.

Figure 2 shows a plot of the function $\Delta N/\Delta d = f(d)$ which characterizes the distribution of defects with respect to the diameter d for part of the microphotograph of Fig. 1b. The diameter of the loops was measured along the line of zero contrast. The existence of two maxima at $d_1 = (50 \pm 10)$ Å and $d_2 = (150 \pm 50)$ Å is characteristic. If this curve is represented as the sum of two symmetric curves, then the ratio of the number of primary point defects in the loops for the two curves is <0.1; that is, the bulk of the point defects enter in the formation of the set of loops that are characterized by large mean diameters. When it was being examined with the electron microscope the foil was turned with its irradiated side downward. Stereomicroscopic examination revealed that all the defects were concentrated on this side in a layer several hundred angstroms thick.

Determination of the Burgers Vectors. According to the Frank criterion, the vectors $\mathbf{b} = a/2$ <111> and $a$ <100> are stable Burgers vectors for body centered cubic crystals [5], but sometimes small loops with **b** equal to $a/2$ <110> are observed, for example, in niobium [6, 7]. Clearly, these types of vectors exhaust all the possible variants in our case as well.

Figure 1c shows a microphotograph of part of a foil which has more than 2000 secondary defects resolvable in the electron microscope. The largest of them are characterized by an extremely wide range of contrast because of the strong dependence of contrast features in images of fine loops on a number of diffraction and orientational parameters [8-10].

Light-field microphotographs were obtained for $s > 0$ in the $\pm\mathbf{g}$ reflections of type <200>, <110>, and <211>. In terms of typical contrast forms, the more than 200 loops with diameters of at least 100 Å that were analyzed could be divided into 21 groups. Schematic repre-

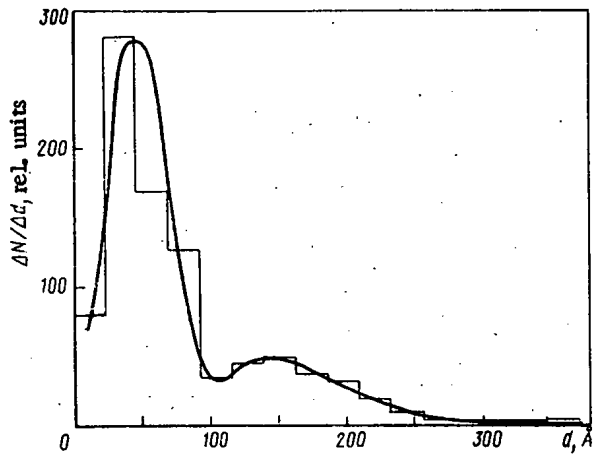


Fig. 2. Size distribution of secondary defects for part of the foil in Fig. 1b (N = 885).

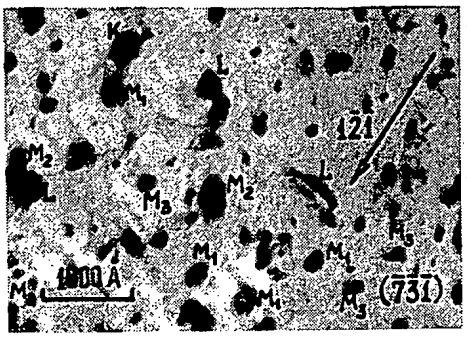


Fig. 3

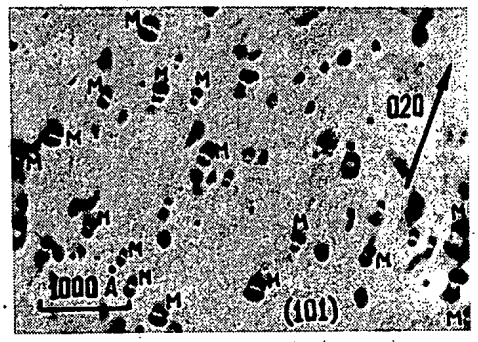


Fig. 4

Fig. 3. Fragment of part of the structure shown in Fig. 1c; g is $1\bar{2}\bar{1}$; only loops with $\mathbf{b} = a/2[\bar{1}\bar{1}1]$ lose contrast; loops denoted K have $\mathbf{b} = a/2[\bar{1}1\bar{1}]$, L, $a/2[\bar{1}11]$, $M_1$, $a[\bar{1}00]$, $M_2$, $a[0\bar{1}0]$, $M_3$, $a[00\bar{1}]$.

Fig. 4. Dislocation loops with Burgers vector $\mathbf{b} = a[0\bar{1}0]$ (denoted by M); g is 020.

sentations of the contrat for eight of these groups of dislocation loops in the 200, 020, and 002 reflections are shown in Table 1. There the crystallographic indices of the plane (hkl) perpendicular to the electron beam are enclosed in parentheses. This kind of "catalog" of the images of all groups of dislocation loops in the three main reflections made it much easier to identify the loops on photographs obtained in other reflections. For fixed s and g the different contrast types in the small loops are the result of different Burgers vectors b with unlike orientations of the planes of the loops and, often, of the crystal with respect to the electron beam. The depth of the defect is also quite important; however, in the present case this factor evidently has little effect because of the concentration of defects at the surface of the foil.

In analyzing the conditions for fade-out of the contrast, it was found that the dislocation loops had Burgers vectors of the $a/2\langle 111\rangle$ and $a\langle 100\rangle$ types. In order to test this the contrast strengths were compared with the magnitude of the product $\mathbf{g}\cdot\mathbf{b}$ [11]. A study of the distribution of loops in these groups showed that dislocation loops with Burgers vectors $a[\bar{1}00]$, $a[0\bar{1}0]$, and $a[00\bar{1}]$ occur in roughly equal amounts and that the same can be said of loops with Burgers vectors $a/2[1\bar{1}\bar{1}]$, $a/2[\bar{1}1\bar{1}]$, and $a/2[\bar{1}\bar{1}1]$. In addition, it was possible to identify a few small loops with $\mathbf{b} = a/2[\bar{1}\bar{1}\bar{1}]$.*

Determination of the Character of the Loops. The determination of the character of the loops was based on a study of the changes in size of the loops under different diffraction conditions (see Table 7.1 of [8]) since loops with both types of Burgers vectors were edge or almost edge loops. It is somewhat difficult to use the simple standard methods of finding the normal n to the plane of a complete dislocation loop [12] when the loops have diameters <250 Å. Although the most reliable data can only be obtained with the aid of computer calculations of the contrast of an image [9], in this case the traditional analysis methods were used while taking experience gained in working with molybdenum into account [12].

Loops with Burgers Vector $a/2\langle 111\rangle$. It was first established that the defects lie on the lower surface of the foil by noting the change (during tilting) of the image of several fairly large segments of the same type whose contrast group was the same as in part of a loop with $\mathbf{b} = a/2\langle 111\rangle$ (Fig. 3). The possible indices n were determined from the locus of the poles in combination with one of the three standard techniques [12]. According to the "catalog" (see Table 1), the loops of each of the three types (b equal to $a/2[1\bar{1}\bar{1}]$, $a/2[\bar{1}1\bar{1}]$, and $a/2[\bar{1}\bar{1}1]$) manifest up to six contrast types. It was thus concluded that part of the loops with $\mathbf{b} = a/2\langle 111\rangle$ lies in planes perpendicular to b and part lies in planes whose normals are inclined at an angle of up to roughly 20° to the <111> direction. According to extensive data on molybdenum subjected to neutron irradiation at elevated temperatures [13,

*An uncertainty remains in choosing the sign of the vector b because of a lack of knowledge of the type of loop. Thus, for concreteness the signs of all the vectors have been chosen as if all the loops were edge injection loops and the [111] direction of the crystal were opposite to the direction of motion of the electrons.

TABLE 1. Contrast Patterns of Dislocation Loops

| Group No. / Diffr. vect. | 200 (011) | 020 (100) | 002 (310) | Burgers vector type |
|---|---|---|---|---|
| 1 |  | | | a<100> |
| 2 | |  | | |
| 3 | | |  | |
| 4 |  |  |  | a/2<111> |
| 5 |  |  |  | |
| 6 |  |  |  | |
| 7 |  |  |  | |
| 8 |  |  |  | |

~200 Å

14] or to irradiation followed by annealing (at up to 750°C) [15, 16], injection loops with this Burgers vector lie in the {110}, {111}, and {321} planes. Since the poles of the {110} planes are inclined at an angle >35° to the <111> direction (i.e., an angle much greater than the observed inclinations), it was concluded that in this case the dislocation loops with $\mathbf{b} = a/2$ <111> lie not only in planes of type {111}, but also in the type {321} planes nearest to them whose normals form an angle of 22°12' with the directions of the <111> Burgers vectors. Thus, these loops are prismatic, nearly or purely edge loops. As each direction <111> is surrounded by six nearest directions of type <321>, seven different contrast types can be formed at loops with a given Burgers vector. This is in general agreement with the experimental data. From the standard rules [5] it was established that all loops with a Burgers vector $\mathbf{b} = a/2$ <111> were injection loops.

Loops with Burgers Vector $a$<100>. A characteristic feature of the contrast of images of these loops when working in the diffraction base vectors **g** 200, 020, and 002 is the strict (or nearly so) perpendicularity of the line of zero contrast to the effective diffraction vector (Fig. 4). It can be assumed, as in [17], that these loops are located in planes of type {100} or close to it, that is, perpendicular or almost perpendicular to the **g** vectors in which their images appear (it follows from Table 1 that a loop with a specific Burgers vector of the type $a$ <100> is visible only in one of the three principal reflections). The absence of an image in the form of a single dark line, as is typical in these cases, is apparently explained by the fact that the image of a dislocation when $\mathbf{g}\cdot\mathbf{b} = 2$ is highly asymmetric with respect to the projection of the nucleus of the dislocation and consists of two peaks of different intensity [18]. An analysis of the planes of the dislocations by the method described previously confirmed this assumption and, furthermore, established that besides the type {100} planes, type {117} and {115} planes can also meet this requirement (they form angles of 12 and 17°, respectively, with the nearest {100} planes). Thus, it was demonstrated that the loops are edge loops or nearly so. Then, using the rules of [5] it was established that all loops with Burgers vectors $a$ <100> were injection loops.

A comparison of the size distribution curve for loops that have $\mathbf{b} = a$ <100> with the curve of Fig. 2 made it possible to analyze the two maxima in the curve fairly unambiguously: the first peak ($d_1 \approx 50$ Å) is due to loops with a Burgers vector $a$ <100> and the second ($d_2 \approx 150$ Å) is due to loops with a Burgers vector $a/2$ <111>.

## Discussion of Results

These experiments showed that bombardment of molybdenum in a deuterium glow discharge plasma causes the formation of a high density of radiation defects in the metal. Besides deuterium ions, impurity ions and ions of the cathode material are involved in defect formation. It was established that all dislocation loops with diameters greater than 100 Å are injection loops. The dark points are also apparently injection defects. It thus follows that in the surface layer of the irradiated metal, a sufficient supersaturation of interstitial atoms is established (despite the closeness of the surface — a powerful sink — and the large diffusion coefficient of interstitial atoms in a bcc crystal [19]) for the nucleation and growth of injection loops. This can be explained by the fact that during low-energy bombardment the interstitial atoms are injected into the depth of the metal as a result of focussing substitution collisions with the surface, similar to the situation observed in face centered cubic metals [20].

In the experiments on bombardment of a monocrystalline molybdenum surface oriented almost perpendicular to the <111> direction, dislocation loops with Burgers vectors of type $a/2$ <111> and $a$ <100> were observed. Loops with $\mathbf{b} = a/2$ <111> are often observed during bombardment of molybdenum by ions and neutrons over a wide range of temperatures [13-16, 21, 22], while loops with $\mathbf{b} = a$ <100> are a rare occurrence in bcc crystals [6, 23-26]. A mechanism has been proposed [27, 28] by which loops with Burgers vectors $\mathbf{b} = a/2$ <111> and $\mathbf{b} = a$ <100> are formed from the nuclei of loops consisting of interstitial atoms in the {110} planes and having vectors $\mathbf{b} = a/2$ <110>. The orientation of the latter is directly coupled to the orientations of the split interstitial configurations [29]. These nuclei contain a packing defect which is eliminated by one of the displacement reactions

$$a/2\ [110] + a/2\ [00\bar{1}] \rightarrow a/2\ [11\bar{1}]; \quad (1)$$

$$a/2\ [110] + a/2\ [\bar{1}10] \rightarrow a\ [010]. \quad (2)$$

The minimum elastic energy is reached as a result of reorientation of the still relatively small loops into edge or nearly edge loops. It can be assumed on the basis of this mechanism that in the present case inhomogeneous elastic compressive stresses in the anisotropic matrix aid the formation of an anomalously large number of loops with a Burgers vector $\mathbf{b} = a$ <100> (see Figs. 3 and 4). These stresses arise as a result of a large local supersaturation in interstitial defects in the surface layer and they aid displacement in the <110> direction in the {110} planes according to reaction (2). Such displacements usually involve the expenditure of considerable energy and are thus unlikely [27]. Compressive stresses in the surface layer are, in our opinion, also the main reason that the number of loops with $\mathbf{b} = a/2\ [\bar{1}\bar{1}\bar{1}]$ constitute a negligibly small fraction of the number of the remaining loops with $\mathbf{b} = a/2$ <111>. In fact, planes of type {110}, in which nuclei are formed for the two comparable groups of loops, have different orientations relative to the surface. This causes the difference in activation of the displacements in the <100> direction according to reaction (1).

This analysis indicated that all the dislocation segments on the observed portion of the foil as well as a number of large dislocation loops (see Fig. 3) had the same vector $\mathbf{b} = a/2\ [\bar{1}11]$. Here it appeared that during the irradiation the [111] direction of the crystal was inclined at 3-5° from the normal to the surface of the foil in the direction of the $[\bar{1}11]$ direction. This fact is evidence of the strong effect of orientation on the formation of defects under these irradiation conditions, which is also evidently connected with the stressed state near the surface. The existence of stresses in the surface layer was confirmed in studies of the structure of monocrystalline molybdenum with different orientations after it had been irradiated in similar fashion in deuterium plasmas.

## CONCLUSIONS

Cathode bombardment of monocrystalline molybdenum surfaces oriented perpendicular to the [111] direction in a deuterium glow discharge plasma at a burning voltage of 500 V with a discharge current density of 4.5 mA/cm$^2$ and a temperature of 800°C leads to formation in

the surface layer of edge and nearly edge loops with Burgers vectors $\mathbf{b} = a/2$ <111> lying in the {111} and {321} planes and the Burgers vectors $\mathbf{b} = a$ <100> lying in the {100}, {115}, and {117} planes. All loops with diameters >100 Å were injection loops. It is proposed that the smaller defects that can be seen in an electron microscope are also aggregates of interstitial atoms. The formation of dislocation loops with Burgers vectors $\mathbf{b} = a$ <100> has been explained in terms of the large compressive stresses which arise in the surface layer of the foil during bombardment. The production of a large number of highly mobile interstitial atoms in the surface layer of a single crystal by the deuterium plasma and their subsequent diffusion to sinks probably play a dominant role in radiation-enhanced self- and heterogeneous diffusion.

LITERATURE CITED


1. A. A. Babad-Zakhryapin and M. I. Lagutkin, Metalloved. Term. Obrab. Met., No. 7, 70 (1976).
2. A. A. Babad-Zakhryapin and G. D. Kuznetsov, Chemical and Thermal Processing in Glow Discharges [in Russian], Atomizdat, Moscow (1975).
3. V. N. Chernikov, A. E. Gorodetskii, and A. P. Zakharov, in: The Interaction of Atomic Particles with Solids [in Russian], Kharkov State Univ., XIV (1976), Part III, p. 170.
4. M. Wilkens and P. Rapps, Phys. Status Solidi, a44, 173 (1977).
5. J. P. Hirth and J. Lothe, Theory of Dislocations, McGraw-Hill (1967).
6. M. Ruhle et al., in: Proc. 4th European Reg. Conf. on Electron Microscopy, Rome (1968), Vol. I, p. 377.
7. J. Narayan and S. Ohr, J. Nucl. Mater., 63, 454 (1976).
8. S. N. Grigorov et al., Electron Microscopic Imaging of Dislocations and Packing Defects [in Russian], Nauka, Moscow (1976), pp. 100, 101, 104.
9. R. Bullough, D. Maher, and R. Perrin, Phys. Status Solidi, b43, 689 (1971).
10. D. Maher, B. Eyre, and R. Perrin, in: Proc. 6th European Conf. on Electron Microscopy, Jerusalem (1976), p. 239.
11. J. Edington, Interpretation of Transmission Electron Micrographs, Philips Gloeilampenfabrieken, Eindhoven (1975), p. 26.
12. D. Maher and B. Eyre, Characterisation of Small Resolved Perfect Dislocation Loops by Transmission Electron Microscopy, Harwell (1970), Pt. I, p. 16.
13. J. Brimhall, B. Mastel, and T. Bierlein, Acta Met., 16, 781 (1968).
14. J. Brimhall and B. Mastel, Rad. Effects, 3, 203 (1970).
15. J. Brimhall, B. Mastel, and T. Bierlein, J. Appl. Phys., 36, 2585 (1965).
16. B. Mastel and J. Brimhall, Acta Met., 13, 1109 (1965).
17. D. Brandon and P. Bowden, Phil. Mag., 6, 707 (1961).
18. P. Hirsch et al., Electron Microscopy of Thin Crystals [Russian translation], Mir, Moscow (1968), p. 262.
19. E. Simonen and J. Brimhall, in: Proc. of Int. Conf. on Fundamental Aspects of Radiation Damage in Metals, Vol. II (1975), p. 1196.
20. P. Bowden and D. Brandon, J. Nucl. Mater., 9, 348 (1963).
21. P. Rao and G. Thomas, Acta Met., 15, 1153 (1967).
22. C. English et al., op. cit., ref. 19, p. 910.
23. J. Meakin, A. Lawley, and R. Koo, Appl. Phys. Lett., 5, 133 (1964).
24. B. Masters, Phil. Mag., 11, 881 (1965).
25. J. Bentley, B. Eyre, and M. Loretto, op. cit., ref. 19, p. 925.
26. B. Eyre, J. Phys. F: Met. Phys., 3, 422 (1973).
27. B. Eyre and R. Bullough, Phil. Mag., 12, 31 (1965).
28. R. Bullough and R. Perrin, Proc. R. Soc. A305, 541 (1968).
29. R. Johnson, Phys. Rev., 134, A1329 (1964).
30. V. N. Chernikov, Interaction of Atomic Particles with Solids [in Russian], Part I, Izd. MRTI (1978), p. 76.

# EROSION OF THE FIRST WALL OF TOKAMAKS

M. I. Guseva, E. S. Ionova,
and Yu. V. Martynenko

UDC 539.12.04:121.039.616

Erosion of the surface of the first wall of a thermonuclear reactor as a consequence of bombardment by corpuscular and electromagnetic radiation may have a double effect. On the one hand, it causes a reduction in the thickness of the wall, thereby reducing the lifetime of the vacuum chamber, and, on the other hand, as a result of erosion, particles of wall material are injected into the plasma, which enhance radiative energy losses from the plasma, thereby reducing the plasma temperature and the pulse length of the reactor.

It has been demonstrated in several studies [1-3] that the main physical process responsible for erosion of the first wall surface is sputtering of the wall material by $D^+$, $T^+$, and $He^+$ ions. At the beginning of a discharge pulse the desorption of surface contaminants (primarily oxygen and carbon) by electron impact and electromagnetic irradiation may have an important effect. Hence a reactor must include facilities for cleaning the chamber surface prior to a working pulse by means of special conditioning discharges. It has been shown [3] that the electron desorption coefficient, which plays a dominant role, must be reduced to $10^{-6}$ mole/electron.

Over a certain period of operation of the reactor, helium blistering may also contribute significantly to erosion of the wall [2]. An estimate of the rate of erosion of the wall due to sputtering and blistering requires knowledge of the fluxes and energies of the particles which go from the plasma to the wall, of the sputtering coefficients S (equal to the ratio of the number of target atoms removed from the surface during sputtering to the number of particles incident on the surface), and of the erosion coefficients S* for blistering.

During radiation blistering and flaking pieces of the surface layer of size 1-100 μm are removed, but for the sake of uniformity the erosion coefficient S* is also expressed in units of atoms/ion. The overall erosion coefficient is equal to the sum of the sputtering coefficient and the erosion coefficient for blistering. We shall examine the T-20 tokamak as an example of a large-scale tokamak.

The rate of wall erosion is conveniently characterized by the thickness d removed from the wall during a year of continuous operation. For erosion due to sputtering alone,

TABLE 1. Sputtering Coefficients for $H^+$, $D^+$, $T^+$, and $He^+$ Ions, Wall Erosion after 1 year of Reactor Operation, and Values of $\bar{S}_\Sigma Z^2$ for Various Materials

| Material | $\bar{S}_H$, atoms/ion | $\bar{S}_D$, atoms/ion | $\bar{S}_T$, atoms/ion | $\bar{S}_{He}$, atoms/ion | $d$, cm | $\bar{S}_\Sigma Z^2$ | Ref. |
|---|---|---|---|---|---|---|---|
| Be | $2{,}8\cdot10^{-2}$ [9] | $6{,}8\cdot10^{-25}$ [10, 11] | $1{,}3\cdot10^{-2}$ [10,11] | 0,54 [10, 11] | $6{,}4\cdot10^{-2}$ | 13,2 | [9], [6, 11] |
| B | $1{,}5\cdot10^{-2}$ | $5{,}8\cdot10^{-2}$ | $1{,}2\cdot10^{-1}$ | 0,41 | $5{,}5\cdot10^{-2}$ | 15,2 | [9] |
| Carbon pyrocer. | $6{,}5\cdot10^{-3}$ | $2{,}2\cdot10^{-2}$ | $4{,}45\cdot10^{-2}$ | 0,13 | $2{,}4\cdot10^{-2}$ | 7,2 | [12, 6] |
| Al | $1{,}3\cdot10^{-3}$—$-2{,}2\cdot10^{-2}$ | $4\cdot10^{-3}$—$-5\cdot10^{-2}$ | $7\cdot10^{-3}$—$-2{,}7\cdot10^{-1}$ | $1{,}9\cdot10^{-2}$—$-7{,}4\cdot10^{-1}$ [11—13] | $6{,}3\cdot10^{-3}$—$-2{,}5\cdot10^{-1}$ | 8,5—182,8 | [11, 13] |
| Ti | $4{,}7\cdot10^{-3}$ [2] | $1{,}2\cdot10^{-2}$ | $2{,}4\cdot10^{-2}$ | $6{,}4\cdot10^{-2}$ [11] | $2{,}7\cdot10^{-2}$ | 51,2 | [2], [11,6] |
| V | $8{,}3\cdot10^{-3}$ | $2{,}3\cdot10^{-2}$ | $4{,}3\cdot10^{-2}$ | 0,12 | $3{,}9\cdot10^{-2}$ | 101,8 | [6, 11] |
| 0Kh16N15M3B | $1\cdot10^{-2}$ | $3{,}4\cdot10^{-2}$ | $10^{-2}$ | 0,23 | $6{,}4\cdot10^{-2}$ | 213 | |
| Mo | $1{,}3\cdot10^{-3}$ | $7{,}5\cdot10^{-3}$ | $2\cdot10^{-2}$ | $5{,}6\cdot10^{-2}$ | $1{,}9\cdot10^{-2}$ | 150 | [2] |
| W | $3\cdot10^{-4}$ | $8\cdot10^{-4}$ | $2{,}3\cdot10^{-3}$ | $1{,}1\cdot10^{-2}$ | $2{,}7\cdot10^{-3}$ | 79 | [11, 6] |
| SiC | $7\cdot10^{-3}$ | $2{,}3\cdot10^{-3}$ | $4{,}1\cdot10^{-2}$ | 0,12 | $1{,}4\cdot10^{-2}$ | 19,2 | [2] |
| TiC | $6\cdot10^{-3}$ | $1{,}76\cdot10^{-2}$ | $3\cdot10^{-2}$ | $8{,}4\cdot10^{-2}$ | $2\cdot10^{-2}$ | 27 | [9, 6] |
| BeO | $4\cdot10^{-2}$ | 0,13 | 0,24 | 0,86 | $1\cdot10^{-1}$ | 57,6 | [9, 6] |
| $B_4C$ | $1{,}1\cdot10^{-2}$ | $4{,}3\cdot10^{-2}$ | $9{,}5\cdot10^{-2}$ | 0,34 | $4{,}1\cdot10^{-2}$ | 69,7 | [9, 6] |
| $Al_2O_3$ | $2{,}4\cdot10^{-2}$ | 0,135 | 0,24 | 0,75 | $1{,}1\cdot10^{-1}$ | 44 | [9, 6] |
| $SiO_2$ | $4\cdot10^{-2}$ | 0,13 | 0,23 | 0,69 | $2\cdot10^{-1}$ | 109 | [9, 6] |
| $TiB_2$ | $1{,}2\cdot10^{-2}$ | $3{,}86\cdot10^{-2}$ | $6{,}7\cdot10^{-2}$ | 0,18 | $3{,}3\cdot10^{-2}$ | 33,4 | [9, 6] |

Translated from Atomnaya Énergiya, Vol. 48, No. 3, pp. 162-166, March, 1980. Original article submitted June 4, 1979.

 0038-531X/80/4803-0182$07.50 

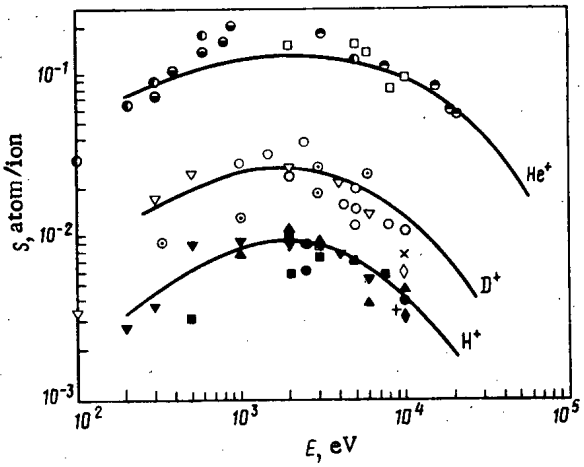


Fig. 1

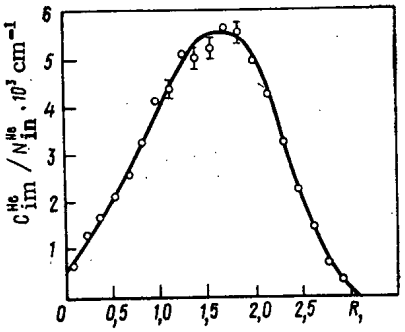


Fig. 2

Fig. 1. Energy dependence of the sputtering coefficients for various stainless steels by $H^+$, $D^+$, and $He^+$ ions: ×, experiment for EP-125; ◇, for 01Kh18N40M5; ▲, for AS-9; ▼, for EI-847; ◆, for 4S-43P; ◒, ◐, ◓, □, ▽, ○, ⊙, ■, ●, +, experiments for 304 and 316 steels [5].

Fig. 2. Concentration profile of 3.5 MeV α particles in stainless steel with the angular distribution of the α particles taken into account [8].

where A and ρ are the atomic mass and density of the wall material; $\bar{S}$, the average sputtering coefficient over the energy spectrum; q, the fluxes of D, T, and He ions and atoms; $\bar{S}_S$, the average sputtering coefficient for the target material by ions; β, a coefficient which specifies the fraction of sputtered atoms which are thermalized in the plasma and return to the wall; and α, a coefficient which takes into account the reduction by the divertor of the ion flux to the wall. Following [4] we assume $\beta = 0.1$. For these estimates, we also set $q_D = q_T = 10^{15}$ $cm^{-2} \cdot sec^{-1}$ and $\alpha = 1$.

The energy spectrum of the fast D and T atoms which go from the tokamak plasma to the wall can be well approximated by a Maxwellian distribution with a temperature corresponding to the outer layer of the plasma [3]. For a rough estimate of the energy distribution of the fast atoms incident on the wall we assume the temperature of the outer layer to be 1 keV. This is evidently an upper limit on the possible temperature.

Figure 1 shows the sputtering coefficients S due to $H^+$, $D^+$, and $He^+$ ions for a number of American [5] and Soviet steels. Using these experimental data we have calculated the average sputtering coefficients $\bar{S}$ due to these particles with a Maxwellian distribution at a temperature of 1 keV: $\bar{S} = 3.4 \cdot 10^{-2}$ atom/ion and $\bar{S}_D = 7 \cdot 10^{-2}$ atom/ion [6]. The sputtering coefficient of iron due to these ions with an energy of 1 keV is 2 atoms/ion [7].

As for the α particles, it has been found that at least 75% of the high-energy $He^+$ ions produced in a large-scale tokamak would be retained in the plasma [8]. According to [8], in the approximation of a uniform plasma, the relative number of α particles going from the plasma column to the wall for the parameters of the T-20 [7] is 0.26. In reality the confinement of α particles in the plasma will be significantly better since only those α particles produced in the periphery of the plasma column will go to the chamber walls [7]. For a plasma with a parabolic radial distribution of parameters, the number of high-energy ions which reach the wall is much lower. In T-20 [7] the ratio of the maximum value of the α particle flux to the chamber wall for a plasma with a parabolic radial distribution to that for a uniform plasma is $3 \cdot 10^{-3}$. When the parabolic plasma distribution is taken into account, those parts of the chamber which are characterized by small azimuthal angles θ close to $|\theta| \approx$ 50-60° [6, 7] will be subject to the greatest interaction with α particles.

The spread of the α particles with respect to the angle of incidence will result in a spreading of the distribution profile of the $He^+$ ions which are driven into the wall and in a reduction in their penetration depth.

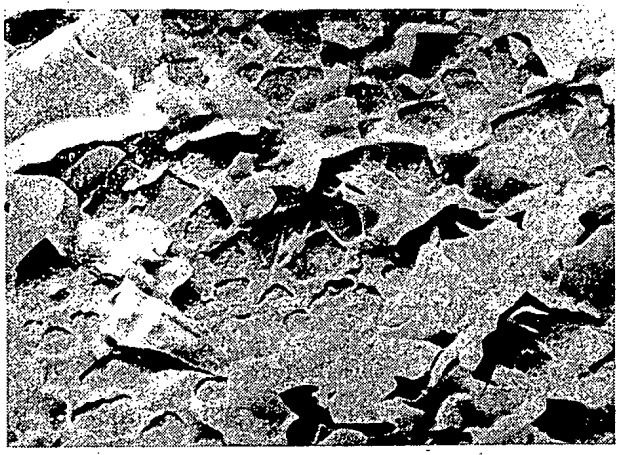

Fig. 3. Microscopic structure of an ÉI 847 stainless-steel surface after irradiation by 100-keV $He^+$ ions with $T_{irrad} \approx 200°C$ and $D_{irrad} = 1.5 \cdot 10^{18}$ $cm^{-2}$.

Figure 2 shows a calculated profile [8] of the concentration of α particles with energies of 3.5 MeV in stainless steel including the angular distribution of the α particles. The average penetration depth is $R_p \approx 1.6$ μm and the mean spread in the depths is $\Delta R_p \approx 2.5$ μm while for normal incidence of 3.5 MeV $He^+$ ions, $R_p \approx 7.5$ μm and $\Delta R_p$ 0.3 μm [5]. For the expected energy distribution of $He^+$ ions, roughly 80% of the integrated dose will lie in the interval 100-350 keV (when scaled to normal incidence).

It follows from [7] that for a plasma density on the column axis of $\sim 10^{14}$ $cm^{-3}$ and $T_0 =$ 15 keV, the maximum flux of α particles to the wall for $\theta \approx 60°$ is $8 \cdot 10^{11}$ $cm^{-2} \cdot sec^{-1}$. It has been shown [8] by a computer calculation that the average flux of α particles to the wall corresponds to approximately half the peak value for $\theta \approx 60°$. On the basis of this result we assume that the mean flux of α particles to the chamber wall of T-20 will be $q_{He} = 4 \cdot 10^{11}$ $cm^{-2} \cdot sec^{-1}$.

The sputtering coefficient of stainless steel for 100-keV $He^+$ ions is 0.02 atom/ion. Substituting these values for $q_{He}$ and $\bar{S}_{He}$ together with the analogous values for deuterium and tritium ($q_D = q_T \approx 10^{15}$ $cm^{-2} \cdot sec^{-1}$; see table) into the equation given above, we find that the rate of erosion of a stainless steel wall due to sputtering by $T^+$, $D^+$, $He^+$, and $Fe^+$ ions will be 0.26 mm/year (without a divertor). Here the sputtering of the wall by high-energy helium ions will be negligibly small compared to the sputtering action of hydrogen isotope ions whose fluxes to the wall are more than three orders of magnitude greater than the flux of α particles. Thus, over five years of operation a wall layer 1.3 mm thick will have been sputtered off.

As noted previously, radiation blistering may play an important role together with sputtering in the destruction of the first wall [1, 2, 5]. Figure 3 shows a typical picture of the damage to an ÉI-847 stainless-steel surface following irradiation by 100-keV $He^+$ ions. The rate of erosion S* calculated from microphotographs is 0.71 atom/ion. The extent of damage due to helium blistering depends strongly on the temperature and irradiation dose. The maximum erosion for various austenitic stainless steels occurs in the temperature range $(0.34\text{-}0.43)T_m$ (where $T_m$ is the melting temperature) [14, 15]. In particular, for ÉI-847 stainless steel the rate of ionization is greatest when $T_{irrad} = 400°C$ and when the dose is $2 \cdot 10^{19}$ $cm^{-2}$, S* = 0.95 atom/ion.

For a rough estimate of the rate of erosion of the first wall of T-20 due to implantation of helium ions we take S* = 1 atom/ion. For the fluxes of high-energy $He^+$ ions expected in T-20, in a year of continuous operation $2.5 \cdot 10^{19}$ ions/$cm^2$ will be injected into the wall. Thus, the erosion is $3 \cdot 10^{-2}$ mm/year, that is, two orders of magnitude smaller than that due to the combined sputtering by $D^+$ and $T^+$ ions.

It should be kept in mind, however, that all the experiments done up to now have been basically model experiments in which the effect of various corpuscular emissions from the plasma have been studied separately, while under real conditions the material would be irradiated by all these particles simultaneously. Because of the synergetic effect, the integral

effect of the corpuscular plasma radiation on the wall may be quite different from a simple arithmetic sum of the separate effects due to the components. First, the synergetic effect may have a large effect on the characteristics of blister formation. It is to be expected that the cutoff doses for blistering [16] will be substantially reduced due to sputtering of the blister shells by intense beams of $D^+$ and $T^+$ ions. On the other hand, the critical doses for blister formation during simultaneous irradiation by helium and hydrogen ions are reduced and surface erosion is enhanced.

Studies of the role of synergism and the behavior of materials under conditions close to those to be expected in real thermonuclear reactors will be needed in the near future.

Thus, a rough analysis shows that wear of the first wall surface in T-20 will mainly be determined by sputtering due to low-energy hydrogen isotope ions. Over a five-year operating period in a reactor the loss of stainless-steel wall material will be 1.3 mm (neglecting the effect of a divertor). In order to ensure reliable heat transfer and prevent mechanical stresses due to the temperature drop, the wall thickness must not exceed about 2 mm. Furthermore, because of the high atomic numbers of the constituents of stainless steel, the stainless steel erosion products which enter the plasma cause it to cool by radiation. The radiation power is roughly proportional to $\bar{S}_\Sigma Z^2$ [3]. Since the radiation will remove 30-50% of the plasma energy, the use of a stainless-steel first wall will significantly reduce the efficiency of a reactor. If stainless steel is used as a first-wall material, the problem of protecting the wall may be solved as follows:

1. Develop coatings which are renewed within the reactor during its stops between working pulses.

2. Make a screen which carries all the radiation and thermal load (except neutrons). Heat is removed from this screen by radiation. The screen must be made of heat resistant materials.

3. Develop nonrenewable coatings whose rate of erosion is an order of magnitude lower than that of stainless steel. The erosion of the coating should be no more than 0.1 mm over a 5-year operating period.

The basic specifications for the materials and screen coatings are the following:

1) heat resistance; the screen must work with radiation cooling;

2) the coatings put on the screen must have good adhesion during thermal loading (including thermal cycling) and during ion bombardment;

3) the thickness of the coatings on the screen must be sufficient for the entire operating period;

4) the parameter $\bar{S}_\Sigma Z^2$ must be as small as possible;

5) the coatings can be deposited on various heat resistant materials.

Each element of the screen could be designed as a small plate.

The renewable and nonrenewable coatings will have basic specifications such as the following:

1) good adhesion to stainless steel under ion bombardment conditions;

2) the temperature of the coatings during operation, as the temperature of the stainless steel, must not exceed 200-400°C, but thermal cycling during operation of the reactor must be possible, and the coatings must have sufficient thermal conductivity for cooling by heat removal through a stainless-steel wall;

3) minimal $\bar{S}_\Sigma Z^2$;

4) there must be a simple technique for applying the renewable coatings to the wall without having to take the reactor apart when it is stopped and the thickness of the renewable coating must not be very great but, evidently, must be thicker than the penetration depth of helium ions with energies of about 300 keV (about 4-10 μm, depending on the coating material).

The nonrenewable coatings, as indicated above, must have low erosion coefficients such that a 0.1-mm-thick coating can endure the full effect of reactor operation.

All coatings and screens must be economical. Possible screen materials include graphite (for example, carbon pyroceramic [12]) and the carbides of the light metals [9, 17] and of silicon [18] (see Table 1).

It might be noted that at present titanium is a sufficiently well-known renewable coating material. It is also evidently appropriate to examine the possibility of using beryllium coatings. Titanium coatings have a number of advantages: the technique for applying them has been developed and was used on PLT during runs in which a plasma with a temperature of 5.5 keV was obtained; titanium coatings improve the vacuum in the chamber and aid in reducing $Z_{eff}$; the sputtering coefficients and, especially, the parameter $\bar{S}_\Sigma Z^2$ for titanium are lower than for stainless steels (see table); titanium coatings inhibit the penetration of hydrogen isotopes into a coated stainless steel wall because the solubility of hydrogen in titanium is much greater than in stainless steel; and, because of the very high solubility of hydrogen in titanium, hydrogen blistering is practically excluded.

The problem of hydrogen saturation and flaking arises for titanium coatings. However, experiments [10] have shown that thin titanium films can be regenerated from titanium hydride at much lower temperatures than massive samples. This is because in thin films the dominant process in the regeneration is dissociation of the hydride rather than diffusion of hydrogen, and the hydride dissociates at $T \approx 250°C$ [10]. Thus, $\sim$1000 Å (1 Å=$10^{-10}$ m) thick titanium films can be regenerated in about 1 second when $T \approx 300°C$. It should be noted that hydrides do not form either in thin films or in massive samples of the alloy Ti—Al—V, a material which might be used as a coating, at temperatures $\geq 300°C$. Titanium alloy coatings are promising but more detailed study is needed.

Beryllium coatings have still lower values of $\bar{S}_\Sigma Z^2$ and better thermal conductivity than titanium. However, the sputtering coefficients of beryllium are comparable with S for stainless steel (see Table 1), and beryllium coatings are less heat resistant than those of titanium. The techniques for working with beryllium are considerably more complicated.

Materials with very low sputtering coefficients are needed for nonrenewable coatings. In this regard there is great interest in the search for the creation of materials with low erosion coefficients.

It can thus be said that at present the best ways of solving the first-wall problem is to make a renewable coating of sputtered Ti—Al—V (PT-3V) alloy on stainless steel and to make a screen which bears the radiation and thermal load. Carbon pyroceramic or MPG-7 graphite at a temperature above 700°C as well as titanium carbide can be recommended as a material for this kind of screen.

## LITERATURE CITED


1. M. Kaminsky, in: Proc. Int. Summer Inst. on Surface Sci., Wisconsin (1975).
2. R. Behrisch, Plasma Wall Interaction, Pergamon Press, Oxford, New York (1977).
3. V. M. Gusev et al., Preprint IAÉ-25456 (1975).
4. G. Kulchinsky and G. Emmert, J. Nucl. Mater., 53, 31 (1974).
5. W. Bauer, Surface Processes in Plasma Wall Interactions, Sand. 78-86-34 (1978).
6. M. I. Guseva and Yu. V. Martynenko, Fiz. Plazmy, 2, 593 (1977).
7. Ya. I. Kolesnichenko, A. D. Fursa, and V. A. Yavorskii, Fiz. Plazmy, 2, 911 (1976).
8. W. Bauer et al., Nucl. Fusion, 19, 93 (1979).
9. D. Mattox and D. Sharp, Low Energy Hydrogen Ion Erosion Yields as Determined with a Kaufman Ion Source, Sand. 78-1029 (1978).
10. M. Malinorosky, The Desorption of $TiD_2$ Films Formed during Simulated Tokamak Gettering Cycles, Sandia Laboratories, Livermore, Ca. (1979).
11. C. Ken Knight and G. Wehner, J. Appl. Phys., 35, 322 (1964).
12. N. P. Busharov et al., At. Energ., 42, 486 (1977).
13. J. Rosenberg and G. Wehner, J. Appl. Phys., 33, 1842 (1962).
14. V. M. Gusev et al., The Temperature Dependence of Blistering under Helium Ion Irradiation, Soviet—American Topical Meeting, Argonne (1979).
15. M. Kaminsky, S. Das, and M. Sunha, J. Appl. Phys., 49, 170 (1978).
16. V. M. Gusev et al., Rad. Effects. 41, 37 (1979).
17. J. Bohdansky, H. Bay, and W. Ottenberger, J. Nucl. Mater., 76, 163 (1976).
18. R. Behrisch, in: Seventh Int. Conf. on Atomic Collisions in Solids, Moscow (1977).

# MEASUREMENT OF SPECTRUM OF FLUX OF ULTRACOLD NEUTRONS BY MAGNETIC INTEGRATING SPECTROMETER

Yu. Yu. Kosvintsev, Yu. A. Kushnir, and V. I. Morozov

UDC 539.125.516.4.07

Measurement of the spectrum of a flux of ultracold neutrons (UCN) is one of the most difficult problems in UCN experiments. Almost all existing methods of measuring such spectra are based on separating the neutrons in energy in the gravitational field of the Earth. The associated apparatus required to analyze a flux of $\sim 2 \cdot 10^{-7}$ eV ultracold neutrons is quite cumbersome. For instance, the widely used П-knee gravitational spectrometer has a neutron guide of total length not less than 4 m [1]. The complex character of the motions of neutrons in the guide makes it difficult to allow for the absorption of the UCN in the walls of the guide and for the effect of the latter on the shape of the measured spectrum.

Distortions of the spectrum due to the large number of collisions of the UCN with the spectrometer walls can be avoided by separating the UCN in energy using their ability to be reflected from the energy barrier produced by a magnetic field in a bounded region of space [2, 3]. For UCN with a spin oriented along the field, the height of the barrier $E_b = \mu B$, where $\mu$ is the neutron magnetic moment and B is the magnetic induction. Numerically, $E_b = 60.3B$ neV, where B is the magnetic induction expressed in teslas.

To obtain an energy barrier of 100 neV requires a magnetic field of 1.7 T, which can be produced with little difficulty by an electromagnet in a $\sim$1 cm gap. This makes feasible the construction of an integrating magnetic spectrometer with a short neutron guide, on traversing which the UCN will experience relatively few collisions with the wall. A magnetic-integrating spectrometer of this sort was used to measure the UCN spectra from an SM-2 reactor (Fig. 1).

The main part of the spectrometer is the electromagnet, which consists of a yoke, poles with shaped tips, and excitation coils. The ends of the pole tips have the form of rectangles of area $1 \times 10$ cm. The coil windings are cooled by compressed air. The maximum magnetic field induction in the 1 cm gap between the pole tips is 2.6 T for a current of 140 A through the exciting coils. In the electromagnet gap there is located a short neutron guide made from electropolished copper with cross section $1 \times 8$ cm in the central part and having cylindrical flanges at the ends. One of the flanges of the neutron guide is connected to a gas ($^3$He) proportional detector with an aluminum input window of area 60 cm$^2$. The other flange of the neutron guide is connected to a rotatable knee, rotation of which varies the height of the spectrometer $H_M$ above the transporting neutron guide for removing the UCN from the SM-2 reactor [4].

Neutrons entering the spectrometer with a spin oriented along the field and having, at the spectrometer input, an axial component of velocity $v_z > (2E_b/m)^{1/2}$ (m is the neutron mass) pass through the energy barrier and are recorded by the detector; neutrons with $v_z < (2E_b/m)^{1/2}$ are reflected. Ultracold neutrons with oppositely oriented spin (against the

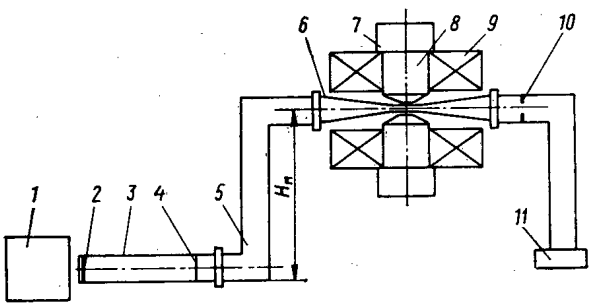


Fig. 1. Schematic diagram of magnetic-integrating UCN spectrometer. 1) Reactor core; 2) UCN converter; 3) transporting neutron guide; 4) aluminum membrane; 5) rotatable knee; 6) neutron guide of spectrometer; 7) electromagnet yoke; 8) poles; 9) exciting coils; 10) diaphragm; 11) UCN detector.

Translated from Atomnaya Énergiya, Vol. 48, No. 3, pp. 166-169, March, 1980. Original article submitted April 23, 1979.

0038-531X/80/4803-0187$07.50  

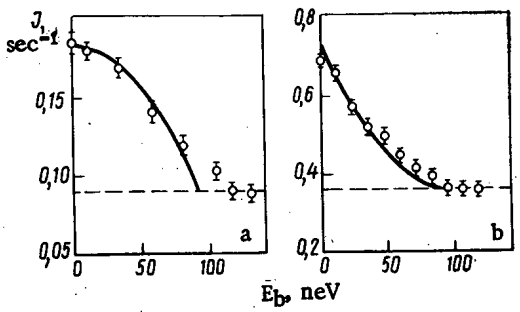


Fig. 2

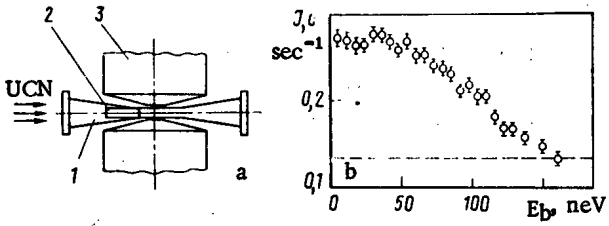


Fig. 3

Fig. 2. Dependence of UCN count rate on height of energy barrier of magnetic spectrometer operating in the (a) accumulative, (b) streaming mode. The solid curves correspond to calculation, the circles to experiment, and the dashed lines to the count rate for neutrons with spin oriented against the field.

Fig. 3. a) Experimental arrangement; b) plot of dependence of UCN count rate vs barrier height for spectrometer operating with collimator. 1) Spectrometer neutron guide; 2) collimator; 3) electromagnet; circles correspond to experimental points; dashed line corresponds to count rate for neutrons with spin oriented against the field.

field) pass through the space between the poles for any value of the magnetic field and are accelerated, acquiring an additional kinetic energy, equal to $E_b$ in the region with maximum magnetic induction. If the maximum energy of the investigated spectrum $E_{max} > E_{by}/2$, where $E_{by}$ is the boundary energy of the guide wall material (for copper $E_{by} = 172$ neV), neutrons that have gathered an energy $E > E_{by}$ can leave the confines of the neutron guide as a result of a diffuse collision and fail to enter the detector. Neutrons with an oppositely directed spin can be lost only within the magnet gap, where $E > E_{by}$, since after they have traversed the gap the ultracold neutrons are again decelerated to the previous energy.

The probability of UCN being lost from the confines of the guide is reduced greatly by placing a collimator in front of the pole tips; the collimator selects neutrons from the incident flux whose velocity lies in a narrow solid angle along the axis of the neutron guide. If $E_{max} \leq E_{by}/2$, all neutrons with spin against the field pass through the neutron guide of the spectrometer, and the need for a collimator disappears. In this case the spectrometer was used in the accumulative or streaming modes of operation.

In the accumulative mode of operation, neutrons which have passed through the barrier are gathered in the region between the detector and the poles of the magnet. For this purpose, the area of the detector input window is made much less than cross-sectional area of the neutron guide in the region of the poles. The UCN count rate depends on the height of the barrier produced by the magnetic field in the following manner:

$$J(E_b) = \text{const} \int_{E_b}^{E_{max}} \varphi(E)\, dE + J_0, \tag{1}$$

where $\varphi(E)$ is the investigated spectrum of the UCN flux; $J_0 = J(0)/2$ is the count rate for neutrons with spin against the field, where $J(0)$ is the UCN count rate for $E_b = 0$.

It can be seen from (1) that, in the accumulative mode, the spectrum of the flux can be found by differentiating $J(E_b)$:

$$\varphi(E_b) = \text{const}\, [dJ(E_b)]/dE_b. \tag{2}$$

When the spectrometer is operated in the streaming mode, neutrons which have passed through the energy barrier are immediately recorded by the detector. In this case, the area of the input window of the UCN detector is made much greater than the cross-sectional area of the neutron guide. In this case, the UCN count rate as a function of barrier height aquires the form:

$$J(E_b) = \text{const} \int_{E_b}^{E_{max}} \varphi(E)\,(1 - E_b/E)\, dE + J_0, \tag{3}$$

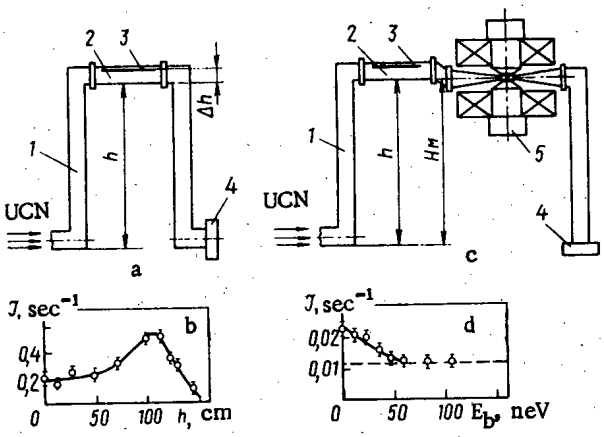


Fig. 4. Experimental arrangement and results of linewidth investigations using gravitational differential spectrometer. a) Gravitational differential spectrometer [1) knee, 2) rectangular channel, 3) UCN absorber, 4) UCN detector]. b) UCN count rate vs h, height to which knee is raised. c) Experimental arrangement for analyzing linewidth by magnetic integrating spectrometer [1) knee, 2) rectangular channel, 3) UCN absorber, 4) UCN detector, 5) magnetic spectrometer]. d) Dependence of UCN count rate on height of energy barrier of magnetic spectrometer connected at exit of rectangular channel with absorber.

where the factor $(1 - E_b/E)$ has the significance of the transmission coefficient for neutrons of energy E through a barrier of height $E_b$ averaged over angles of incidence for a UCN flux with an isotropic angular distribution.

It follows from (3) that the spectrum of the flux can be found utilizing the relationship:

$$\varphi(E_b) = \text{const}\, E_b \frac{d^2 J(E_b)}{d^2 E_b}. \qquad (4)$$

The magnetic integrating spectrometer was used in the accumulative and streaming modes of operation to measure the spectrum of the UCN flux at the outlet from the rotatable knee, lifted to a height $H_M = 104$ cm. The UCN count rate directly at the exit from the knee amounted to 10 neutrons/sec. The accumulative mode was implemented by placing a copper diaphragm with an aperture of area 2.5 $cm^2$ in front of the detector. In the streaming regime, the diaphragm was removed.

In the experiment we investigated the dependence of the count rate for UCN which traversed the neutron guide of the spectrometer as a function of the height of the energy barrier produced by the magnetic field. The results of the measurements are shown in Fig. 2. The solid curves correspond to calculation via (1) and (3) on the assumption that the UCN spectrum corresponds to the initial part of a Maxwellian flux distribution with $E_{max} = 91$ neV. This choice for the maximum energy of the spectrum was made because the upper boundary of the spectrum of ultracold neutrons taken from the transporting neutron guide amounts to 197 neV [5].

As can be seen from Fig. 2, the obtained experimental plots for the accumulative and streaming modes differ considerably, but are in satisfactory agreement with the theoretical calculations obtained on the assumption that the spectrum of the flux is Maxwellian. This demonstrates that the accumulative and streaming modes are indeed realized. The slight discrepancy between the results of experiment and calculation probably comes about because the ultracold neutrons removed from the transporting guide contain a small proportion of energy greater 197 neV.

Figure 3 shows the experimental dependence $J(E_b)$ obtained using the magnetic spectrometer to investigate the spectrum of the UCN flux directly at the exit from the transporting neutron guide. In this case $E_{max} > E_{by}/2$, and accordingly a collimator (Fig. 3a) made from polyethylene in the form of a rectangular channel of cross section $1 \times 1$ cm is placed in front of the poles. In the collimation mode of operation of the spectrometer, the spectrum of the UCN flux is connected with the UCN count rate by relationships (1) and (2), as in the accumulative mode. As can be seen from Fig. 3b, the obtained dependence coincides in its basic features with the expected form of the spectrum. The lower boundary of the spectrum, determined by the presence of the aluminum membrane ($E_{by} = 55$ neV) in the transporting guide, amounts to 50-60 neV, and the upper boundary to 160-170 neV, which differs slightly from the value obtained in the previous experiment. The discrepancy in the upper region of the spectrum is probably due to insufficient collimation of neutrons with spin oriented against the field.

The magnetic spectrometer was also used to analyze the linewidth obtained from the gravitational differential spectrometer described in [6, 7], which incorporates a П-shaped knee in the upper horizontal part of which is introduced a rectangular channel with an UCN absorber (Fig. 4a). A construction of this sort should transmit neutrons with an energy in the range $mgh < E < mg(h + \Delta h)$, where g is the acceleration due to gravity; h is the height of the lift of the knee; $\Delta h$ is the distance between the UCN absorber and the bottom of the rectangular channel ($mgh = 1.02$ neV for $h = 1$ cm).

The gravitational differential spectrometer used in the linewidth measurements had a rectangular aluminum channel 40 cm long, $\Delta h = 4$ cm; the UCN absorber was polyethylene.

Figure 4b shows the dependence of the UCN count rate on the uplift h of this knee, connected to the output from the transporting guide. The plot of J(h) is nonzero in the region $h < 54$ cm, although neutrons of energy less than 55 neV should not participate in the spectrum due to the presence of the aluminum membrane in the transporting guide of the apparatus. The existence of a nonzero count rate at energies <55 neV can be explained if it is assumed that neutrons of energy $E > mg(h + \Delta h)$ are partially transmitted through the rectangular channel of the spectrometer.

We checked this hypothesis by measuring the spectrum of the UCN flux at the exit from the rectangular channel using the magnetic integrating spectrometer. To this end the knee was lifted to a height $h = 90$ cm, and the spectrometer to a height $H_M = 90$ cm (Fig. 4c). The results of the measurements are shown in Fig. 4d. It can be seen that a considerable proportion of the neutrons transmitted through the rectangular channel have an energy of up to 50-60 neV, which considerably exceeds the linewidth $mg\Delta h = 4$ neV. In this connection, the existence of a UCN count rate at a knee uplift less than 54 cm is most likely due to the recording of neutrons of energy greater than 55 neV, rather than less, as was suggested in [7].

LITERATURE CITED

1. L. V. Groshev et al., Preprint Joint Institute for Nuclear Research, RZ-5392, Dubna (1970).
2. Yu. Yu. Kosvintsev, Yu. A. Kushnir, and V. I. Morozov, Pis'ma Zh. Tekh. Fiz., 2, No. 7, 293 (1976).
3. Yu. Yu. Kosvintsev et al., Preprint NIIAR, P-15 (281), Dmitrovgrad (1976).
4. Yu. Yu. Kosvintsev et al., Preprint Joint Institute for Nuclear Research, RZ-10238, Dubna (1976).
5. Yu. Yu. Kosvintsev et al., Pis'ma Zh. Eksp. Teor. Fiz., 28, No. 3, 164 (1978).
6. Yu. Yu. Kosvintsev et al., in: Neutron Physics, Part 1 [in Russian], Izd. TsNII-atominform (1977), p. 183.
7. V. N. Dvoretskii, Preprint IAÉ-2715, Moscow (1976).

# DIIODIDE CRYSTALS FOR γ-RAY DETECTORS

V. M. Zaletin, I. N. Nozhkina,
V. I. Fomin, N. V. Shustov,
and I. I. Protasov

UDC 539.1.074

The production of uncooled semiconductor detectors (SCD) for making effective spectrometric measurements of x-rays and γ-rays over a wide energy range is one of the important lines of development of research methods in nuclear physics. The most promising material for the construction of such detectors is mercury diiodide, $HgI_2$. Its high atomic number (Z = 80), the large width of its forbidden band (2.13 eV), and its very high resistivity ($\sim 10^{12}$ Ω-cm) make the efficiency of uncooled $HgI_2$ detectors in the spectrometric measurement of x-ray and γ quanta higher by about one order of magnitude than that of SCD using GaAs and CdTe. In recent years perfect $HgI_2$ crystals have been obtained, and these have been used in constructing x-ray and γ-ray detectors [1-6].

The initial material used was ChDA-brand (analytical-grade) mercury diiodide salt with an $HgI_2$ content ≥99.5%. The impurities were removed by three methods: recrystallization from a solution of $HgI_2$ in hydrochloric acid which was saturated at 100°C, multiple sublimation, and thermochemical distillation [7]. The data on the efficiency of each of these purification methods are shown in Table 1.

As is known, the successes achieved in obtaining perfect single crystals of $HgI_2$ are due primarily to the development of gas-phase methods [1, 3, 5]. At the same time, obtaining crystals from solutions is simpler in design, and it is clear that this method permits constant monitoring of the process and corrections as required. For this reason, we begin our investigation of processes for growing $HgI_2$ single crystals with this method.

Since mercury diiodide is practically insoluble in water, we crystallized it from the organic solvent most acceptable for these purposes — OSCh 9-5-brand (ultra-pure) acetone, with added amounts of dimethylsulfoxide, which increased the solubility of the salt, and water, which acted as a mineralizer. As the seeds we used crystals measuring 1 × 1 × 1 mm; the volume of the crystals grown from the solution was 100-200 $mm^3$.

TABLE 1. Effect of Purification Methods on the Impurities Content of $HgI_2$

| Purification method | Purification conditions | Amount of impurities in the purified $HgI_2$, % by mass | |
|---|---|---|---|
| | | sum of metals: Mn, Mg, Pb, Cr, Fe, Al, Ni, Bi, Ba, Ca, Zn, Cu, Cd, Sn | amorphous carbon-bearing residue |
| Recrystallization from HCl (1:1) | | $2{,}8 \cdot 10^{-4}$ | 0.02 |
| Triple sublimation | Vacuum, $5 \cdot 10^{-5}$ torr* | | Practically none |
| | $t_1 = 210°$ C<br>$t_{2,3} = 130°$ C | $1{,}9 \cdot 10^{-4}$ | |
| Thermochemical distillation | Vacuum, $5 \cdot 10^{-5}$ torr* | | |
| | Evaporation temperature 240°C | $1{,}3 \cdot 10^{-4}$ | Practically none |
| | Superheating temperature 400°C | | |

* 1 torr = 133.332 Pa.

Translated from Atomnaya Énergiya, Vol. 48, No. 3, pp. 169-172, March, 1980. Original article submitted March 26, 1979.

0038-531X/80/4803-0191$07.50  

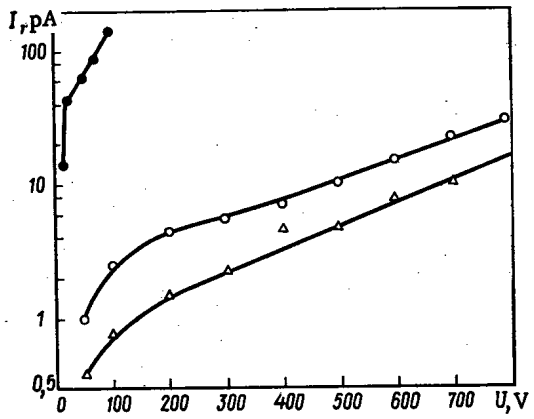


Fig. 1

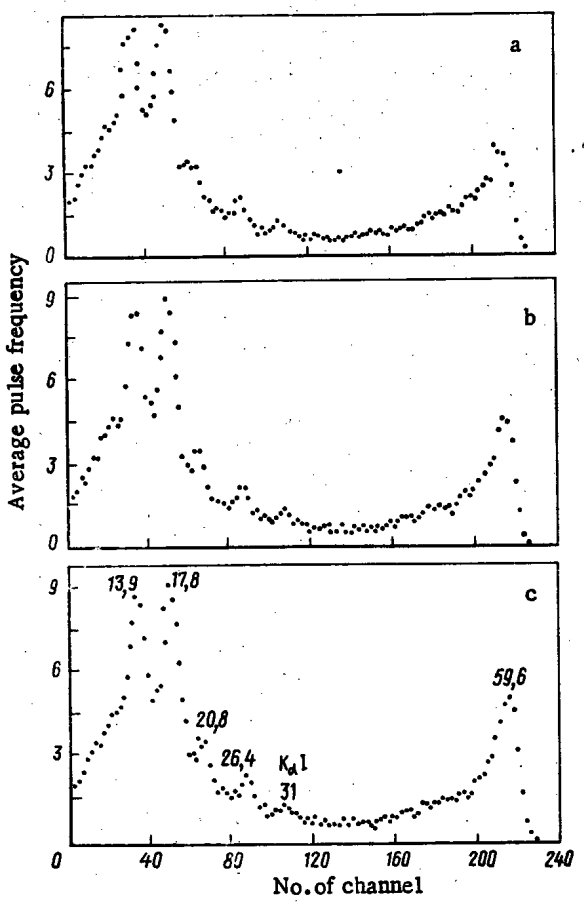


Fig. 2

Fig. 1. Volt—ampere characteristics of detector structures using $HgI_2$; ○) area of sensitive surface Sg = 13 mm$^2$, crystal grown from the gas phase; Δ) Sg = 5 mm$^2$, crystal grown from the gas phase; ●) Sg = 1.5 mm$^2$, crystal grown from solution.

Fig. 2. Variation of the energetic apparatus spectrum of $^{241}$Am as a function of the displacement voltage: a) 200 V; b) 500 V; c) 800 V (area of sensitive surface 13 mm$^2$, detector thickness 0.5 mm, no collimation).

In growing the $HgI_2$ crystals from the gas phase, we used the statistical method and the method of temperature oscillations [1, 3, 4]. Using the latter, we obtained $HgI_2$ single crystals with masses of up to 20 g.

In the process of purification of mercury iodide by multiple sublimation at 110-130°C there may be a partial violation of the stoichiometry of the $HgI_2$ because iodine is more volatile at this temperature than mercury [5, 6]. In order to avoid iodine depletion of the crystalline $HgI_2$, in the last series of experiments the iodine was introduced into an ampule with the purified material.

The degree of perfection of the crystals so grown was studied with respect to the dislocation density, reflection electronograms, and Raman scattering. The electronograms, obtained on the EF-4 electron microscope, from crystals grown by the above-mentioned methods showed that all the specimens had a single-crystal structure but had different degrees of perfection. The dislocation density was calculated on the basis of the etching holes obtained in the processing of the slip plane (001) in a solution of KI. The highest dislocation density ($5 \cdot 10^6$ cm$^{-2}$) was observed in crystals grown from solution. In the crystals obtained from the gas phase by the static method and the method of temperature oscillations the values were $(1-3) \cdot 10^5$ and $5 \cdot 10^5$ cm$^{-2}$, respectively. The lowest dislocation density was found in crystals grown by the static method with iodine supersaturation: $(1-3) \cdot 10^4$ cm$^{-2}$. We were not able to obtain the expected degree of perfection in the crystals when we used the method of temperature oscillations. The reason seems to be that the selected scheme of this method

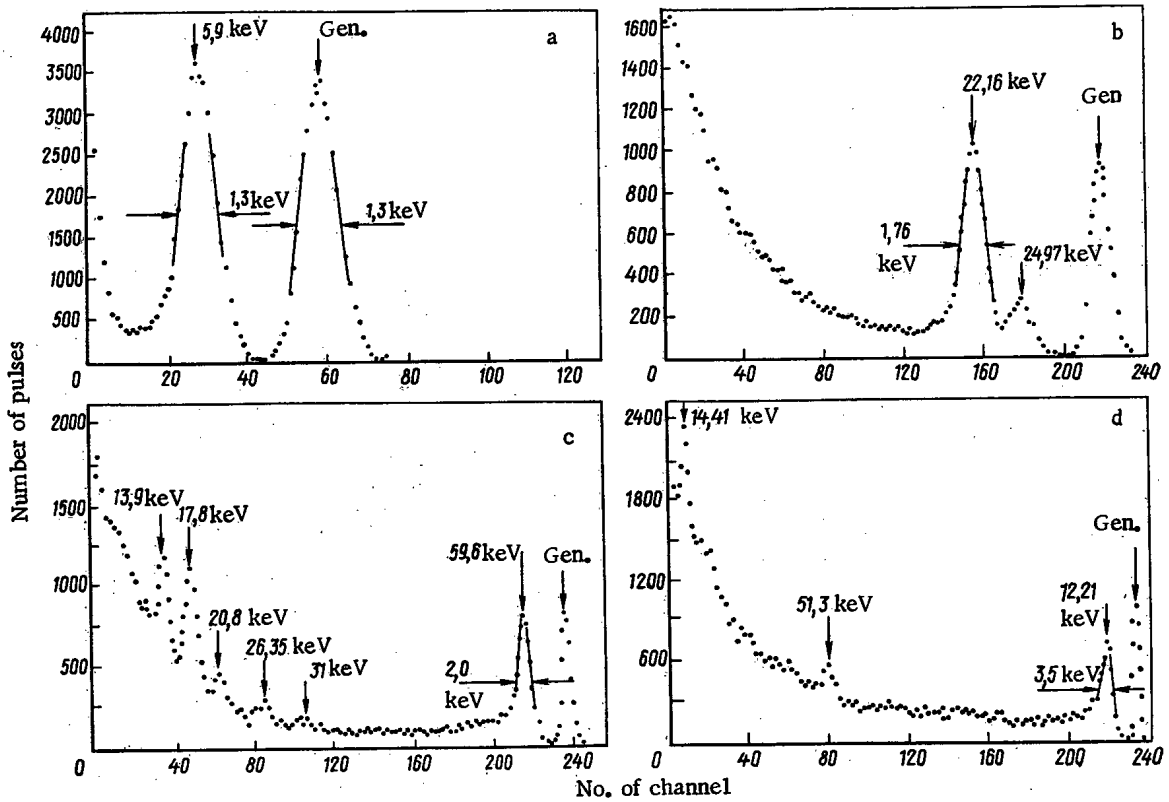


Fig. 3. Energy apparatus spectra obtained by means of $HgI_2$ detectors for $^{55}Fe$ (a), $^{109}Cd$ (b), $^{241}Am$ (c), and $^{57}Co$ (d); Gen. = generator.

(oscillation of the crystal temperature) causes high stresses in the growing crystals, and consequently the dislocation density increases [4]. An analysis of the Raman-scattering spectra showed [8] that the addition of iodine to the gas phase leads to an ordering of the crystal structure and that the crystals obtained from solutions have a great many defects. The reasons for this, in our view, are the inadequate purity of the crystallization medium (acetone) and the intercalation effect characteristic of layered crystals of the $PbI_2$ and $HgI_2$ type [9].

In order to obtain the detector structures, we separated the $HgI_2$ crystals along the (001) cleavage plane into plates 1-1.5 mm thick, and in order to remove the traces of mechanical damage, we etched the plates in a polishing etchant with a potassium iodide base. After washing for 2-3 min in deionized water, the plates were fitted with Aquadag or palladium resistance contacts.

The resulting detector structures were 0.3-0.7 mm thick and had a sensitive surface area of 2-20 $mm^2$. Depending on the area of the contacts, the current through the detector was 1-100 pA at a displacement voltage of 400-1000 V. Typical volt—ampere characteristics for detector structures using crystals grown by different methods are shown in Fig. 1.

The investigation of the spectrometric properties of the resulting detectors was carried out on a mass-produced spectrometric apparatus (PU-2-5 charge-sensitive preamplifier, BUS2-47 spectrometric amplifier, and AI-256-6 multichannel amplitude analyzer) at 300°K, with a constant signal formation time ($\tau_d = \tau_i = 3.2$ μsec).

Detectors made with crystals grown from solution are characterized by a high noise level and a low (~100-300 V) breakdown voltage. When we irradiated these specimens with γ quanta from $^{241}Am$, we were unable to discover any lines characteristic of this isotope, a fact which confirmed the serious electrical and structural defectiveness of the detectors.

A useful signal was recorded on practically all the crystals grown from the gas phase. The specimens from the first series from gas-phase experiments were characterized by poor assembling of the charge, especially the hole component. The peak for total absorption of γ quanta with an energy of 59.6 keV was very weakly distinguishable. This may be due to the iodine depletion during the purification and growing of the $HgI_2$, as indicated above. Ap-

parently the violation of stoichiometry associated with the removal of iodine from the regions near the surface of the crystal results in a diffusion of the uncompensated Hg atoms into the volume of the crystal. There is a probability of the appearance of an interstitial defect of the $I_{Hg}$ type (Hg in the interstices). According to [6], the interstitial Hg is an effective center for the capture of holes, and the presence of these defects considerably reduces the value of $\mu_p\tau_p$ [$\mu_p$ is the hole mobility, $cm^2/(V\cdot sec)$, $\tau_p$ is the lifetime, sec].

The addition of iodine to the gas phase during the process of growth or purification not only improved the degree of perfection of the crystals [8] but also made it possible to use them for constructing detectors capable of spectrometric measurement of $\gamma$ quanta over a fairly broad energy range. However, the question of the optimal iodine supersaturation for obtaining detector crystals remains open and must be studied further. Of course, the degree of perfection of the crystal and its possibilities for the recording and spectrometric measurement of $\gamma$ quanta are determined not only by its characteristic defects but also by the background impurities and residual impurities of the growth system used. Practically nothing is known about the nature and behavior of the main impurities in $HgI_2$. Therefore, further improvement in the quality of detector $HgI_2$ must come from a study of the composition of the impurity background, improvement of the purification and growing methods, and the discovery and removal of the main sources of impurities.

Figure 2 shows the energy spectra of $\gamma$ quanta of $^{241}Am$ for different working voltages. The detector was irradiated from the negative-electrode side. All the spectra and total-absorption peaks show a low-energy "tail." Its contribution increases with increased $\gamma$-quantum energy. The fact that such a tail is present and that the position of the photopeak changes little as the working voltage increases indicates insufficient assembling of one of the components of the charge. In the case when the dominant contribution to the amplitude of the signal is provided by the electron component of the charge ($E_\gamma = 13.9$ and 17.8 keV with penetration into the crystal to a depth of 50-100 $\mu$m), the collection of the charge is considerably better. This calls into question the assumption that the hole component of the charge is insufficiently assembled. An increase in the displacement voltage leads to an improvement in the collection of the holes and an increase in the total-absorption peak; however, losses in the hole component remain fairly large.

The energy spectra of $^{55}Fe$, $^{109}Cd$, $^{241}Am$, and $^{57}Co$ are shown in Fig. 3. The resolution values obtained for the 5.9, 22.5, 59.6, and 122 keV lines are 1.3, 1.75, 2.0, and 3.5 keV, respectively (PShPV). From the spectra shown it can be seen that in the low-energy region (<10 keV) the use of $HgI_2$ detectors is limited by the noises inherent in the use of the electronic equipment, and in the high-energy region it is limited by the insufficient assembling of the hole component of the charge.

The authors wish to express their gratitude to A. F. Kravchenko for his support and his interest in the work. They also thank T. N. Petrunin for his assistance in the preparation of the detector structures.

LITERATURE CITED

1. H. Scholz, Acta Electron., 17, No. 1, 69 (1974).
2. S. Swierkowski, G. Armantraut, and R. Wichner, IEEE Trans. Nucl. Sci., 21, No. 1, 302 (1974).
3. J. Ponpon et al., ibid., 22, No. 1, 182 (1975).
4. M. Slapa, G. Huth, and W. Seibt, ibid., 23, No. 1, 102 (1976).
5. L. Van den Berg and R. Whited, ibid., NS-25, No. 1, 177 (1978).
6. R. Whited and L. Van den Berg, ibid., NS-27, 148 (1977).
7. É. M. Kiseleva and S. A. Stroitelev, Izv. Sib. Otd. Akad. Nauk SSSR, Ser. Khim. Nauk, No. 12, Issue 5, 162 (1970).
8. V. A. Gaisler et al., in: Proceedings of the Conference on Semiconductor Detectors for Nuclear Radiation, Kiev, October 24-27, 1978, Report No. 18 [in Russian].
9. V. M. Koshkin et al., Fiz. Tekh. Poluprovodn., 18, No. 2, 609 (1976).

# LETTERS

## CONCERNING THE CHOICE OF GRAPHITE FOR STACKING OF HIGH-TEMPERATURE GAS-COOLED REACTORS

Yu. S. Virgil'ev and V. P. Shevyakov

UDC 621.039.532.21

High-temperature gas-cooled reactors (HTGR) have been assuming ever increasing importance, as confirmed by years of operating experience in various countries [1]. The temperature of the graphite stacking of HTGR reaches 400-1200°C and the fluence attains values of $(2-3)\cdot10^{22}$ neutrons/cm$^2$.* Accordingly, only ceramic materials are used in the cores of such reactors: graphite as moderator, reflector, and other structural elements of the reactor core and carbides and oxides of uranium and thorium as fuel. Helium is the coolant. Radiation damage to graphite, however, continues to be one of the most urgent problems, owing to the possibility of considerable macroscopic changes in the shape of the structural elements as well as a reduction of the strength of the materials.

Graphite in HTGR should operate under very demanding conditions. To begin with, it experiences radiation-thermal contraction (compression), which is then replaced by secondary swelling. The latter depends to a very great degree on the conditions of irradiation as well as on the properties of the graphite and is usually accompanied by the formation of microcracks. The microcracks in turn are a cause of secondary changes in the physical properties: a drop in thermal conductivity, strength, etc. Therefore, along with high dimensional stability, the graphite should also possess high physical properties, including strength.

In the present paper we consider the radiation behavior of several forms of graphite in order to assess the service life of the structural elements of the reactor core. Above all, the dimensional stability of the graphite blocks should be ensured so as to eliminate the possibility of their splitting under contraction and breaking under secondary swelling. Table 1 gives the radiation-induced changes in the dimensions of specimens of some grades of graphite [2-4]: the American anisotropic CSF, isotropic RP4, and graphite based on gilsonite coke, and Soviet GMZ graphite and its variant, in which impregnation with pitch and graphitization at 2800°C have been employed.

It is seen from the data presented that the use of anisotropic graphite, similar in properties to the CSF graphite used formerly, is extremely undesirable, since by the end of service the circumferential strain of the reflector reaches +7% if the extrusion axis of the blocks coincides with the radius of the reactor. This means that with a reactor core diameter of 7 m the length of the circumference increases by 1.5 m. With vertical orientation of the axis of the block the circumference "shrinks" by 1.5 m and gaps form between the blocks of the reflector if they are fastened individually to the reactor vessel.

In view of this, various forms of isotropic graphite materials are being developed. Thus, the Sigri company produces graphite from AS 2-500 pitch coke for hexagonal fuel elements and replaceable reflector blocks as well as a special graphite made for AS 12-500 pitch coke for reflector blocks and supporting columns [5]. The use of stronger graphite, along with measures to reduce corrosion due to water vapor entering the helium, will ensure conservation of the serviceability of the graphite stacking. Graphite obtained by isostatic forming is distinguished by isotropy [6] and high dimensional stability under irradiation.

By using high-density, high-strength isotropic carbon material it is possible to solve the problem of fatigue service life, radiation stability, and corrosion [7]. Indeed, the data of Table 1 indicate a higher dimensional stability for isotropic graphite. The serviceability of the blocks in the stacking is also determined by the stresses which arise because of uneven distribution of the temperature and the neutron flux over the cross section of the blocks.

*Here and below the fluence is given for neutrons with E > 0.18 MeV.

Translated from Atomnaya Énergiya, Vol. 48, No. 3, pp. 174-175, March, 1980. Original article submitted November 10, 1978.

0038-531X/80/4803-0195$07.50 

TABLE 1. Relative Change of Length in Specimens of Various Grades of Graphite, %*

| T, °C | Fluence, $10^{22}$ neutrons/cm$^2$ | CSF | RP4 | Gilsonite | GMZ | GMZ-2800 |
|---|---|---|---|---|---|---|
| 700—800 | 2,2 | — | — | — | $\frac{-1,0}{+0,4}$ | $\frac{-0,4}{<0}$ |
| 775—825 | 2,2 | $\frac{-8,0}{+7,0}$ | — | — | — | — |
| 950 | 0,6 | $\frac{-4,0}{+0,2}$ | $\frac{-2,5}{+0,2}$ | $\frac{-0,8}{-0,6}$ | $\frac{-0,6}{-0,3}$ | $\frac{-0,3}{\sim 0}$ |

*In the numerator are values for specimens cut parallel to the extrusion axis and in the denominator, those for perpendicular specimens.

For the most stressed segments of the stacking the operating life of the reflector blocks is limited by both an inadmissible increase in their dimensions and by stresses in the blocks that exceed the allowable values [8]. To ensure the serviceability of the reflector blocks, therefore, it is recommended that graphite with enhanced strength characteristics be used.

Below we give the average values and the variation coefficient of the properties of PXA2N graphite for a HTGR reflector [9] (in the numerator are values for specimens in the direction parallel to the axis of extrusion and in the denominator, those in the perpendicular direction):

| | Average value | Variation coefficient, % |
|---|---|---|
| Density, g/cm$^3$ | 1.794 | 1.2 |
| Strength, kgf/cm$^2$ (1 kgf/cm$^2$ = 98066.5 Pa) | | |
| compression | 803/814 | 15.1/12.5 |
| bending | 314/287 | 19.3/16.9 |
| tension | 248/230 | 21.2/22.7 |
| Modulus of elasticity, $10^5$ kgf/cm$^2$ | 1.14/1.08 | 9.6/9.2 |
| Thermal expansion coefficient, $10^{-6}$ deg$^{-1}$ | 5.09/5.43 | 5.3/3.5 |
| Resistivity, $\Omega \cdot mm^2/m$ ($1\ \Omega \cdot mm^2/m = 10^{-6}\ \Omega/m$) | 9.02/9.53 | 5.7/4.6 |
| Corrosion rate, mg/cm$^2$·h | 0.264 | 58 |

In high-temperature service one of the most important characteristics of graphite is its thermal resistance, which is determined primarily by the thermal conductivity of the material [10]. The latter can be raised by increasing the degree of order of the crystalline structure of the graphite as well as the density of the material.

If they do not cause the immediate fracturing of the graphite, the thermal stresses relax at a fluence of about $2 \cdot 10^{21}$ neutrons/cm$^2$. In the region of secondary swelling, however, the resistance of the graphite to thermal stresses should drop. Under irradiation to a fluence of $4.2 \cdot 10^{22}$ neutrons/cm$^2$ and a temperature of 725°C [11] the thermal resistance drops by 30-65%.

Thus, in principle it is possible to choose graphite materials which ensure a long service life for the elements of the stacking of a HTGR without replacement. These graphites should be isotropic (or nearly so), well graphitized, and sufficiently strong. One possible way of enhancing the serviceability of existing graphite materials is that of one-time or repeated packing with pitch and subsequent high-temperature treatment to 2800°C. This simple procedure, however, may prove to be insufficient to ensure the serviceability of the most highly stressed segments of the stacking. It is necessary, therefore, to pay due attention to the development of new, more serviceable graphite materials [6, 7, 9].

LITERATURE CITED

1. D. Badenig, High-Temperature Gas-Cooled Reactors [Russian translation], Atomizdat Moscow (1975).
2. I. Cox and I. Helm, Carbon, 7, No. 2, 319 (1969).
3. G. Engle and W. Eatherly, High Temp.—High Press., 4, 119 (1972).
4. I. P. Kalyagina et al., At. Energ., 36, No. 3, 212 (1974).
5. INIS Atomindex, 7, No. 13, 248274 (1976).
6. INIS Atomindex, 8, No. 7, 281083 (1978).
7. ERDA En. Res. Abstr., 2, No. 7, 17835 (1977).
8. ERDA En. Res. Abstr., 2, No. 8, 19721 (1977).
9. P. Fieguth, M. Schulte-Oversohl, and R. Fritz, Atomwirt.-Atomtechn., 22, No. 4, 225 (1977).
10. Yu. S. Virgil'ev, At. Energ., 44, No. 1, 89 (1978).
11. W. Cook et al., in: Proc. Twelfth Conf. on Carbon, Pittsburgh (1975), p. 305.

# USE OF THIN FILMS TO STUDY PORE DISTRIBUTION OVER DEPTH OF RANGE OF $Ar^+$ IONS IN NICKEL

A. G. Guglya, V. A. Gusev,
V. F. Zelenskii, B. V. Matvienko,
and I. M. Neklyudov

UDC 539.216.2

Learning the effect of inert gases on the radiation swelling of structural materials, an important scientific and practical problem of reactor materials science, is also of substantial interest in relation to the use of beams of accelerated ions of inert gases to simulate radiation damage.

In the present paper we report on the use of thin films [1] to study radiation-induced porosity in nickel along the trajectory of $Ar^+$ ions with an energy of 2 MeV. The irradiation of monocrystalline nickel thin films (thickness 1000 Å,* initial dislocation density $1.5 \cdot 10^9$ $cm^{-2}$), in stacks of five films, was carried out at T = 600°C to the following dose values: $6.3 \cdot 10^{16}$, $2.7 \cdot 10^{16}$, $2.1 \cdot 10^{16}$, and $7.5 \cdot 10^{15}$ ions/cm² (a dose of $1 \cdot 10^{16}$ ions/cm² corresponds to 8 displ./atom in the region of maximum damage).

The relations obtained between the concentration $\bar{n}$ and the mean side $\bar{d}$ of the pores as well as between the swelling $\Delta V/V$ and the depth of the range of argon in nickel (i.e.,

*1 Å = $10^{-10}$ m (exactly) according to the Systeme Internationale (SI).

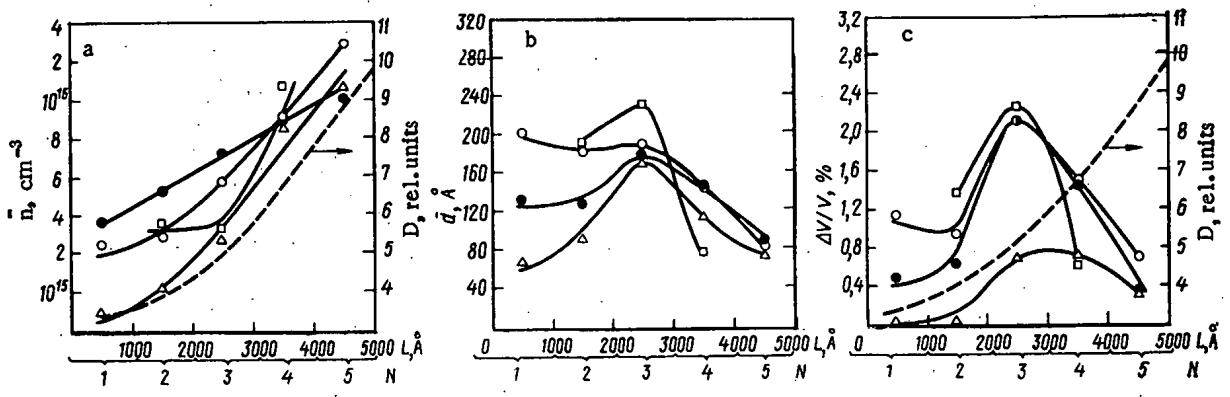


Fig. 1. Dependence of $\bar{n}$, $\bar{d}$, and $\Delta V/V$ on depth of range of $Ar^+$ ions (2 MeV) in nickel irradiated at 600°C at dose of $7.5 \cdot 10^{15}$ (Δ), $2.1 \cdot 10^{16}$ (●), $2.7 \cdot 10^{16}$ (○), and $6.3 \cdot 10^{16}$ ions/cm² (□); ---) calculated dependence of rate of damage generation on depth for $Ar^+$—Ni pair.

Translated from Atomnaya Énergiya, Vol. 48, No. 3, pp. 175-177, March, 1980. Original article submitted January 30, 1979.

0038-531X/80/4803-0197$07.50 

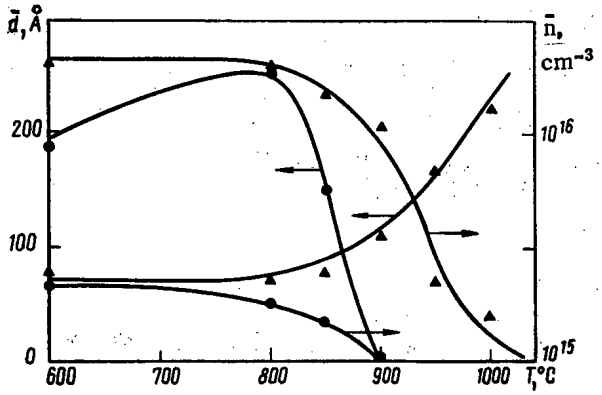


Fig. 2. Size and concentration of pores vs annealing temperature in first (●) and fifth (▲) films of stack.

the number N of films in the stack) indicate (Fig. 1) that with an increase in the depth of ion range the values of $\bar{n}$ increase monotonically while the values of $\bar{d}$ and $\Delta V/V$ reach a maximum in the third film, after which (in the fourth and fifth films) they decrease substantially.

The shape of the curves $\bar{n} = f(N)$ for $N \leqslant 5$ and the curves $\bar{d} = f(N)$ and $\Delta V/V = f(N)$ for $N \leq 3$ are in qualitative agreement with calculation [2]. The decrease in $\bar{d}$ and $\Delta V/V$ in the last two films of the stack clearly is due to the effect of interstitial argon atoms on the process of pore initiation and growth. At an irradiation dose of $1 \cdot 10^{16}$ ions/cm$^2$, the argon concentration in the fourth film is about $1 \cdot 10^{-4}$ atom/atom while in the fifth it is about $8 \cdot 10^{-4}$ atom/atom [3]. At such concentrations the supersaturation with free vacancies begins to diminish, as a result of which there is a decrease in the number of stable nuclei of vacancy pores and an increase in the concentration of nuclei of gas-containing pores. Since the latter have a smaller critical size [5], with a further rise in argon concentration there will likely be an increase in the fraction of fine pores, which may explain the observed decrease in $\bar{d}$ and $\Delta V/V$ in the fourth and fifth films. A similar effect was also observed

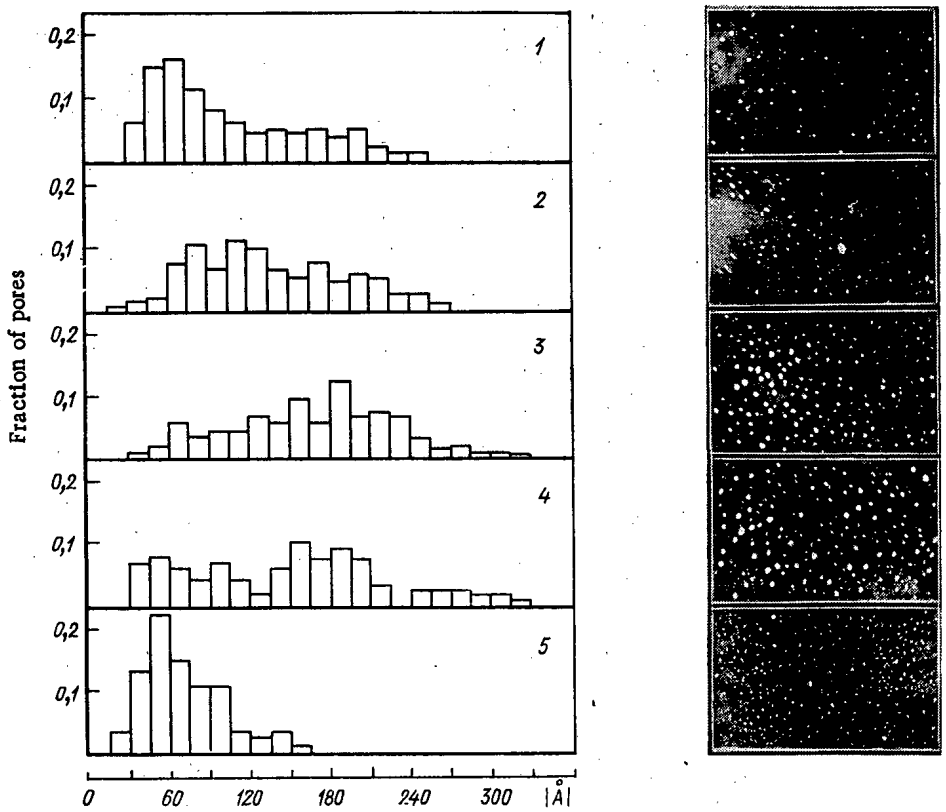


Fig. 3. Pore distribution according to size in five nickel films irradiated with $Ar^+$ ions (E = 2 MeV, T = 600°C, D = $2.1 \cdot 10^{16}$ ions/cm$^2$).

when stainless steel was irradiated with nickel ions [4]. The introduction of 2 · 10⁻⁵ argon atom/atom into the stainless steel reduced swelling by a factor of 3.5 while at an argon concentration of $10^{-4}$ atom/atom it was suppressed altogether.

It can thus be concluded that the nature of the pores observed along the trajectory of $Ar^+$ ions differs: In the first films of the stack these pores are primarily of a vacancy nature while in the other films, of a gas nature. Confirmation of this can be provided by Fig. 2, which illustrates the effect of postirradiation annealing temperature on the density and size of pores in the first and fifth films of the stack. Wherever the argon concentration is low (first film), the pores are completely annealed out at T = 900°C. In the fifth film, where the argon concentration is $10^{-3}$-$10^{-4}$ times higher, the pores are appreciably more resistant to annealing. At some intermediate values of the argon concentration there probably is simultaneous development of both vacancy and gas-filled pores. This is due to the fact that with a particular ratio between the rates at which gas atoms enter and defects form, at first pores predominantly of a vacancy character will form, growing during the process of irradiation. As the irradiation is continued, nuclei of small pores, stabilized by atoms of the gas, will appear.

The distribution of pores according to size will in this case have the shape of a curve with two maxima (Fig. 3, fourth film). Distributions of this kind were observed earlier when "massive" nickel foils were irradiated with $Xe^+$ ions [6].

Thus, irradiation of a stack of thin films makes it possible to determine the characteristics of porosity along the trajectory of bombarding ions and to ascertain the effect of the concentration of the element introduced and the rate at which damage occurs.

## LITERATURE CITED

1. V. F. Zelenskii et al., in: Reactor Materials Science, Proc. Conf. on Reactor Materials Science [in Russian], Vol. 2, Izd. TsNIIatominform, Moscow (1978), p. 20.
2. V. F. Zelenskii et al., in: Reactor Materials Science, Proc. Conf. on Reactor Materials Science [in Russian], Vol. 2, Izd. TsNIIatominform, Moscow (1978), p. 3.
3. V. V. Gann and O. V. Yudin, in: Problems of Atomic Science and Engineering [in Russian], No. 1 (9), Izd. KhFTI Akad. Nauk UkrSSR, Kharkov (1979), p. 37.
4. E. Nelson and J. Hudson, J. Nucl. Mater., 58, 11 (1975).
5. H. Wiedersich, J. Burton, and J. Katz, J. Nucl. Mater., 51, 287 (1977).
6. V. F. Zelenskii et al., At. Energ., 45, No. 1, 61 (1978).

# DIFFUSION OF ACTINIDES AND SOME OF THEIR FISSION PRODUCTS IN HIGH-MELTING bcc METALS

V. N. Zagryazkin

UDC 548.526

Interest in diffusion in high-melting bcc metals (W, Ta, Mo, and Nb) is dictated by the possibility of using these metals and alloys based on them as fuel-element cans operating at a temperature exceeding 1000°C. Published data on uranium diffusion in high-melting metals are contradictory [1-7], the difference in the diffusion coefficients reaching a factor of $10^4$. As far as is known, no systematic studies have been conducted on the diffusion of thorium and plutonium in high-melting metals, and the information about the diffusion of fission products is limited.

To refine the known data and estimate missing information about diffusion in high-melting bcc metals it is appropriate to use generalized correlations [8] associating the diffusion parameters with the process of vaporization, these correlations being of the form

$$D = 0.545a^2\nu \exp\left[-0.35\left(\Delta H_{vap} - T\Delta S_{vap}\right)/RT\right] \exp -0.25\left(\Delta H^*_{vap} - B(1-x)^2\right)/RT\right], \text{ cm}^2/\text{sec}. \quad (1)$$

Here $a$ is the lattice constant, $\Delta H_{vap}$ and $\Delta S_{vap}$ are the heat and entropy of vaporization of the metal-base, B is the interaction energy in the solid solution, $\Delta H^*_{vap}$ is the heat of vaporization of an impurity atom in impurity diffusion or that of the metal-base in self-diffusion, and x is the fraction of impurity atoms. The oscillation frequency $\nu$ is estimated from [8, 9]

$$\nu = 0.415\left[\frac{\Delta H^*_{vap} - B(1-x)^2}{a^2 m}\right]^{1/2}, \text{ sec}^{-1}, \quad (2)$$

where m is the mass of the diffusing atom.

In deriving Eq. (1) it is assumed that diffusion occurs through monovacancies and the entropy of migration in self-diffusion and diffusion of substitutional impurity atoms is much smaller than the entropy of vacancy formation [8]. Comparison with known experimental data showed that the correlations (1) and (2) lead to satisfactory results for both self-diffusion and diffusion of impurities in high-melting bcc metals [8].

Table 1 gives the parameters $D_0$ and $\Delta H$ calculated in [7] for uranium diffusion in high-melting metals with allowance for values of the interaction energy found from known phase diagrams [10]. Comparison of the results of calculation with experiments [1-6] shows that in most cases the calculated diffusion coefficients are higher than the experimental values. A special study of the causes of these discrepancies with the example of uranium diffusion into tungsten, tantalum, and molybdenum from a contacting uranyl foil [7] made it possible to establish that the variable composition of the source makes itself felt here while the results of layered radiometric analysis were processed by the method of a constant source [1, 2] of diffusion.

TABLE 1. Uranium Diffusion Parameters $D_0$ ($cm^2$/sec) and $\Delta H$ (kJ/g·atom) in High-Melting Metals according to Calculated and Experimental Data

| Metal | B, kJ/g·atom | Calc. | | Expt. [7] | |
|---|---|---|---|---|---|
| | | $D_0$ | $\Delta H$ | $D_0$ | $\Delta H$ |
| W | 79 | 0,45 | 399,2 | 0,30 | 399,2 |
| Ta | 60,6 | 0,34 | 379,5 | 0,19 | 366,6 |
| Mo | 48,9 | 0,32 | 341,1 | 0,075 | 341,1 |
| Nb | 1,3 | 0,49 | 372,8 | — | — |

Translated from Atomnaya Énergiya, Vol. 48, No. 3, pp. 177-179, March, 1980. Original article submitted January 30, 1979.

 0038-531X/80/4803-0200$07.50 

TABLE 2. Diffusion Parameters $D_0$ ($cm^2$/sec) and $\Delta H$ (kJ/g·atom) of Actinides and Some of Their Fission Products into High-Melting Metals

| Base | Impurity | B, kJ/g·atom | $D_0$, calc. | $\Delta H$, calc. | $D_0$, expt. | $\Delta H$, expt. | Lit. | $D_{expt}/D_{calc}$ at $0.6T_{mp}$ |
|---|---|---|---|---|---|---|---|---|
| W | W | — | 0,70 | 508,7 | 0,54 | 503,7 | [6] | 1,02 |
| | Th | 92,0 | 0,47 | 417,6 | | | | |
| | Pu | 108,8 | 0,32 | 355,7 | | | | |
| | Y | 108,8 | 0,63 | 377,4 | $6,7 \cdot 10^{-3}$ | 284,7 | [15] | 1,6 |
| | Zr | 60,2* | 0,82 | 430,9 | | | | |
| | Nb | 12,1* | 0,93 | 473,6 | | | | |
| | Mo | 5,4 | 0,87 | 459,8 | 0,3 | 422,2 | [12] | 2,70 |
| | Ru | —22,6* | 0,87 | 464,4 | | | | |
| | Rh | —17,2* | 0,80 | 440,6 | | | | |
| | Pd | 18,8* | 0,62 | 387,5 | | | | |
| | La | 330,5 | 0,18 | 306,4 | | | | |
| Ta | Ta | — | 0,50 | 467,3 | 2,0 | 459,8 | [6] | 6,30 |
| | Th | 75,3 | 0,39 | 397,9 | | | | |
| | Pu | 71,7 | 0,37 | 340,7 | | | | |
| | Y | 200,8 | 0,43 | 330,2 | 0,12 | 301,8 | [15] | 1,56 |
| | Zr | 37,2* | 0,66 | 412,6 | | | | |
| | Nb | 15,9* | 0,74 | 447,7 | 0,36 | 419,7 | [13] | 3,80 |
| | Mo | 4,0* | 0,64 | 436,4 | 0,0018 | 338,6 | [12] | 1,10 |
| | Ru | —175,7* | 0,76 | 478,6 | | | | |
| | Rh | —157,3* | 0,71 | 451,0 | | | | |
| | Pd | —159,8* | 0,61 | 407,5 | | | | |
| | La | 243,5 | 0,26 | 303,9 | | | | |
| Mo | Mo | — | 0,60 | 395,8 | 0,13 | 400,4 | [6] | 0,16 |
| | Th | 75,3 | 0,34 | 356,1 | | | | |
| | Pu | 62,8 | 0,24 | 301,0 | | | | |
| | Y | 63,2 | 0,48 | 322,7 | $1,8 \cdot 10^{-4}$ | 214,4 | [15] | 0,33 |
| | Zr | 27,2* | 0,58 | 373,2 | $1,9 \cdot 10^{-3}$ | 365,7 | [6] | 0,006 |
| | Nb | 3,9* | 0,65 | 408,8 | 14 | 451,4 | [13] | 1,1 |
| | Ru | —23,8* | 0,60 | 398,8 | | | | |
| | Rh | —26,4* | 0,56 | 376,2 | | | | |
| | Pd | —7,1* | 0,45 | 327,7 | | | | |
| | La | 228,4 | 0,24 | 265,6 | | | | |
| Nb | Nb | — | 1,00 | 428,9 | 0,91 | 421,8 | [6] | 1,53 |
| | Th | 87,9 | 0,50 | 372,0 | | | | |
| | Pu | 62,8 | 0,38 | 320,6 | | | | |
| | Y | 65,7 | 0,71 | 339,8 | $1,5 \cdot 10^{-3}$ | 232,4 | [15] | 5,51 |
| | Zr | 28,9* | 0,89 | 395,0 | 0,10 | 376,2 | [14] | 0,44 |
| | Mo | 3,7* | 0,92 | 413,4 | $1,3 \cdot 10^{-2}$ | 349,9 | [6] | 1,43 |
| | Ru | —174,9* | 1,01 | 456,9 | | | | |
| | Rh | —167,4* | 0,93 | 431,0 | | | | |
| | Pd | —149,8* | 0,79 | 382,9 | | | | |
| | La | 229,3 | 0,35 | 285,1 | | | | |

*Data of [11].

Equations (1) and (2) were used to calculate the parameters of the diffusion of thorium, plutonium, and some fission products into high-melting bcc metals. Table 2 at the same time gives the values of the interaction energy B published in [11] and estimated from phase diagrams or by the well-known technique [11]. It can be seen that the calculated and experimental coefficients of volume diffusion at $T = 0.6T_{mp}$ (where $T_{mp}$ is the melting point of the metal-base) differ by a factor of no more than six.

Comparison of the calculated diffusion coefficients shows that the mobility of plutonium in high-melting metals is much higher than that of uranium and thorium. Among the fission products a higher diffusion mobility is possessed by yttrium and lanthanum and a lower coefficient, by molybdenum, ruthenium, and rhodium.

The calculated temperature dependences of the coefficients of volume diffusion are, naturally, tentative and are applicable primarily in the range $(0.5\text{-}0.8)T_{mp}$ where diffusion takes place through monovacancies.

LITERATURE CITED

1. G. B. Fedorov et al., At. Energ., 31, No. 5, 516 (1971).
2. L. V. Pavlinov, A. I. Nakonechnikov, and V. N. Bykov, At. Energ., 19, No. 6, 521 (1965).
3. G. Taylor, Thesis Nucl. Sci. Abstrs., 21, No. 23, 4528 (1967).
4. E. Schwegler and F. White, J. Mass-Spectrom. Ion Phys., 1, 191 (1968).
5. A. V. Yurgens, A. G. Abdullin, and A. A. Tsvetaev, Physicochemical Problems of Crystallization [in Russian], Izd. Kazakh. Gos. Univ., Alma-Ata (1969), p. 185.
6. G. B. Fedorov and E. A. Smirnov, Diffusion in Reactor Materials [in Russian], Atomizdat, Moscow (1978).
7. V. N. Zagryazkin et al., in: Proc. Conf. Thermodynamics of Nuclear Materials 1974, Vol. 2, IAEA, Vienna (1975), p. 193.
8. V. N. Zagryazkin, B. V. Ushakov, and G. Ya. Meshcheryakov, Izv. Akad. Nauk SSSR, Ser. Met., No. 2, 156 (1975).
9. C. Wert and C. Zener, Phys. Rev., 76, 1169 (1949).
10. M. Hansen and K. Anderko, Constitution of Binary Alloys, McGraw-Hill, New York (1961).
11. L. Kaufman and H. Bernstein, Computer Calculation of Phase Diagrams, Academic Press (1970).
12. E. V. Borisov, P. L. Gruzin, and S. V. Zemskii, in: Protective Coatings on Metals [in Russian], No. 2, Nauchnaya Mysl', Kiev (1968), p. 104.
13. J. Asquil, in: Diffusion in Body-Centered-Cubic Metals [Russian translation], Metallurgiya, Moscow (1969), p. 254.
14. G. G. Ryabova and P. L. Gruzin, in: Metallurgy and Metal Science of Pure Metals [in Russian], No. 3, Atomizdat, Moscow (1961), p. 120.
15. R. M. Al'tovskii et al., Corrosion Properties of Yttrium [in Russian], Atomizdat, Moscow (1969).

# NITROGEN DETERMINATION IN MIXED URANIUM—PLUTONIUM FUEL AFTER $^{14}N(\alpha, p\gamma)$ REACTION

V. I. Melent'ev and V. V. Ovechkin

UDC 539.166.3.17

In the development of fast reactors as reactors for the future consideration is being given to fuel elements based on mixed nitride and uranium—plutonium fuel. In view of this it becomes necessary to reliably monitor the content of nitrogen on which the physicomechanical properties of such fuel elements depend. Known methods of chemical and spectral determination of nitrogen in a mixed uranium—plutonium fuel is based on destruction of the specimens, which is not always applicable because of the problem of regeneration of high-activity wastes and possible contamination of apparatus and production premises with them.

It was shown in [1] that it is possible to determine impurities of light elements, ranging from lithium to calcium, in mixtures with α-active $^{238}Pu$ by using a scintillation

TABLE 1. Results of Nitrogen Determination in U + Pu Alloys, wt.%

| Mass of specimen, g | (α, pν) method | Kjeldahl method | Mass of specimen, g | (α, pν) method | Kjeldahl method |
|---|---|---|---|---|---|
| 1,075 | 7,7±0,4 | 7,5 | 0,951 | 5,5±0,3 | 5,91 |
| 1,972 | 7,5±0,4 | 7,46 | 0,989 | 2,6±0,3 | 2,58 |
| 3,843 | 7,5±0,4 | 7,42 | 0,992 | 1,9±0,2 | 1,79 |
| 0,973 | 6,5±0,4 | 6,52 | 0,991 | 3,0±0,2 | 3,14 |
| 0,951 | 6,0±0,4 | 5,91 | 0,989 | 2,4±0,2 | 2,21 |
| 0,995 | 3,6±0,3 | 3,57 | 0,503 | 3,3±0,2 | 3,49 |
| 0,988 | 4,6±0,3 | 4,58 | 0,430 | 3,8±0,2 | 3,86 |
| 0,973 | 6,5±0,4 | 6,52 | | | |

Translated from Atomnaya Énergiya, Vol. 48, No. 3, pp. 179-180, March, 1980. Original article submitted March 12, 1979.

 0038-531X/80/4803-0202$07.50 

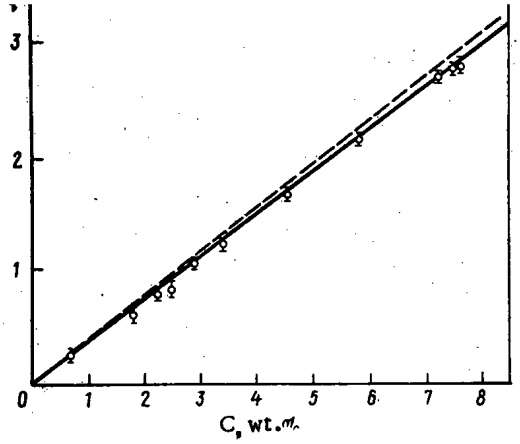


Fig. 1. Dependence of q on nitrogen content in specimen: O) experiment; ---) linear shape of dependence q = f(C).

detector to detect γ-rays produced in the interaction of α-particles with nuclei of the light elements. Another paper [2] reported the characteristics of the analytic method with the use of a Ge(Li) detector for determining nitrogen, fluorine, and sodium impurities in $^{239}$Pu.

The objective of the present paper is to extend this method of analysis to mixed nuclear fuel, consisting of plutonium and uranium. As in [2], a Ge(Li) detector was used to detect γ-rays emitted in the (α, pγ) reaction in nitrogen (E = 871 keV).

Specimens of mixed fuel based on U (80%) and Pu (20%) with a mass of 0.5 to 3.8 g were placed in thin-walled stainless-steel containers inside sealed glass weighing bottles filled with dry argon. In the measurements the weighing bottle was placed on the Ge(Li) detector, covered with a lead filter with a thickness of 1.5 mm to prevent the apparatus being overloaded by intense low-energy γ-radiation from the plutonium.

The nitrogen concentration C was determined from the ratio q of the area of the nitrogen peak (871 keV) to the area of two peaks (756 + 771 keV) of intrinsic $^{239}$Pu γ-radiation by using the calibration relation q = f(C), obtained by measuring control specimens of U + Pu fuel with a mass of 0.25 g. The nitrogen content in the control specimens after the measurements was determined by the Kjeldahl method (the error of the analysis was roughly ±1%). The results of measurements in the range from 0.5 to 7.7 wt.% are shown in Fig. 1.

During the measurements of the analyzed specimens we introduced corrections for the contribution of other α-active radiators: $^{241}$Am and $^{140}$Pu, which were determined from the areas of the α-ray peaks with energies of 722 and 687 keV, respectively. For specimens with highly enriched uranium (in $^{235}$U) we included the small contribution from α-active fission products of $^{232}$U according to the γ-ray peak with an energy of 860 keV from $^{208}$Tl. The energy resolution of the α-ray spectrometer (∿5 keV in the region of 870 keV) and a quite high counting rate made it possible to take such corrections into account accurately.

Let us note that for a finely ground mixture of an α-emitter and other elements with a known concentration the analytic expression for q = f(C) given in [2] can be used if necessary. By this method we made analyses of alloys (20% $^{239}$Pu and 80% U with 90% enrichment in $^{235}$U); the results of the determinations are given in Table 1 along with the results of analysis by the Kjeldahl method.

The error of analysis was calculated in accordance with [3] by

$$\varepsilon = \pm t_{\alpha, N} v_N \overline{C}\, 10^{-2}\, n^{-1/2}, \qquad (1)$$

where $t_{\alpha,N}$ is Student's coefficient for a fiducial probability of α = 95% and N determinations carried out when finding $v_N$. The root-mean-square error of $v_N$ found for N ≥ 20 was 10-7 rel.% for a nitrogen concentration ranging from 3.5 to 7.5 wt.%. The limit of detection of nitrogen was found from the formula

$$\eta = 165\,(Q_b + q_0 P)^{1/2}\,(q' P)^{-1}, \qquad (2)$$

where $Q_b$ is the background number of detector pulses in the region of the photopeak of energy 871 keV; $q'$ and $q_0$, the numbers of pulses recorded, respectively, from 1 g of nitrogen and 1 g of Pu + U alloy not containing nitrogen; and P, the mass of the specimen.

As a result of measurements for 60 min on the control specimen (20% Pu + 80% U, with respect to metal) with a nitrogen concentration of 3.49 wt.% we found that $\eta = 0.05$ wt.%. Since $\eta \sim (Pt)^{-1/2}$, where t is the measuring time, upon increasing t to 4 h and the mass of the specimen to 5 g we may expect to have $\eta = 0.01$ wt.%.

With an increase in the relative plutonium content, the number of interacting α-particles will grow and this should result in a lowering of the detection limit. In particular, for a specimen consisting mainly of $^{239}Pu$, according to the results of measurements of plutonium nitride we got $\eta = 3.5 \cdot 10^{-3}$ wt.% (the mass of the specimen was 5 g and the measuring time was 4 h).

Thus, by a nondestructive method based on γ-ray spectrometry with a Ge(Li) detector it is possible to determine the nitrogen content in a mixed nuclear fuel.

LITERATURE CITED

1. J. McKibben, Nucl. Appl., 4, No. 4, 260 (1968).
2. V. V. Ovechkin, V. I. Melent'ev, and V. F. Gorbunov, Radiokhimiya, 18, No. 1, 152 (1976).
3. R. I. Alekseev and Yu. I. Korovin, Handbook of Computations and Processing of Results of Quantitative Analysis [in Russian], Atomizdat, Moscow (1972).

# OBTAINING ASSESSMENT DATA ON EQUALLY PROBABLE INTRAGROUP SECTIONS FOR PROTECTION CALCULATIONS FROM BASIC LIBRARIES BY THE MONTE-CARLO METHOD

V. E. Kolesov and N. A. Solov'ev

UDC 539.125.523.348:621.039.538

When designing the protection of nuclear apparatus by the Monte-Carlo method, the group-constant method often proves inadequate for the purpose. In such cases we need more detailed information on the interactions between the radiation and the material. At the same time, it is extremely difficult to use basic libraries of estimates directly, due on the one hand to the vast quantity of information on nuclear data, amounting sometimes to several million words for one isotope alone, and on the other hand to the limited capabilities of present day computers. This has had the effect of stimulating the search for new methods and approaches for preparing nuclear data that would enable us to solve problems connected with the degree of accuracy that can be achieved.

Ref. [1] proposes a method involving probability tables which enables us to take the resonance structure of the section into account correctly during the calculations, when comparing small amounts of stored information. Such tables have been calculated on the basis of the energy dependence of the section and enable us to organize the calculations easily by the Monte-Carlo method. This method is close in conception to the well-known subgroup method [2, 3].

The present paper proposes that the full and partial sections be described in groups with the aid of a set of equally probable values, which have been arrived at by averaging out the corresponding sections with respect to energy in nonintersecting intervals with a given weighing function. Each of these intervals includes only those energy points at which the value of the full section deviates least from its average. The data are best represented in the form of equally probable intragroup values in regions within which the resonances are unresolved. However, this method can also be used successfully in a resonance region. The proposed method of taking the resonance structure of the sections into consideration enables us to reduce the calculation time by the Monte-Carlo method, compared to the time involved in using probability tables. It would therefore be an effective way of designing protection. The initial data for obtaining equally probable sections are taken from libraries of assessment data [4, 5].

Deriving Accumulated Probability Functions for Sections. If we introduce probability density function $p(\sigma)$ in the energy interval $\Delta E$, then the average of the whole section function can be calculated by means of the formula [2]

$$\langle g(\sigma)\rangle = \int p(\sigma)\, g(\sigma)\, d\sigma.$$

When calculating the transit of the nuclear radiation by the Monte-Carlo method, our problem reduces to that of expressing $\sigma$ as a function of the accumulated probability:

$$F(\sigma) = \int_{\sigma_{\min}}^{\sigma} p(x)\, dx.$$

Let us choose an ascending series for the whole section

$$\sigma_0 = \sigma_{\min},\ \sigma_1 = k\sigma_0,\ \sigma_2 = k^2\sigma_0,\ \ldots,\ \sigma_i = k^i\sigma_0,\ \ldots,\ \sigma_I = \sigma_{\max} \tag{1}$$

where k is a constant whose value determines the accuracy and structure of the representation of the section, $k > 1$; $\sigma_{\min}$, the minimum section in the interval $\Delta E$; and $\sigma_{\max}$, the maximum

Translated from Atomnaya Énergiya, Vol. 48, No. 3, pp. 180-182, March, 1980. Original article submitted March 23, 1979.

0038-531X/80/4803-0205$07.50  

section in the interval ΔE. With such a construction, the number of terms in the series can be determined from

$$I = [\ln(\sigma_{max}/\sigma_{min})/\ln k] + 1, \tag{2}$$

where [ ] signifies the nearest integer below the given quantity.

In addition to series (1), we shall construct series for the partial processes of scattering, capture and, where appropriate, fission:

$$\sigma_0^r = \sigma_{min}^r\ \overline{\sigma}_1^r,\ \overline{\sigma}_2^r,\ \ldots,\ \overline{\sigma}_i^r,\ \ldots,\ \sigma_I^r = \sigma_{max}^r, \tag{3}$$

where $\overline{\sigma}_i{}^r$ is the arithmetic mean of the partial section, the section being taken for all the energy points at which the whole section equals $\sigma_i$. Series (3) will also diverge and $\sigma_i = \sum_r \overline{\sigma}_i^r$, provided the following conditions are satisfied:

the interference between the partial processes does not lead to a large shift in the position of the whole-section peaks, i.e., the shift is no greater than half the width of the partial section;

the sum of the partial sections at each energy point equals unity.

A breach of the first condition could lead to ambiguity of the accumulated probability function for the partial sections in the individual intervals. We can overcome these difficulties by using average characteristics in such intervals.

We shall postulate that series (1) and consequently series (3) generate a system of I subgroups, and that the i-th subgroup corresponds to the summated energy interval $D_i$, at the points of which the whole section satisfies the relationship

$$\sigma_{i-1} \leqslant \sigma(E) \leqslant \sigma_i. \tag{4}$$

The following quantities also apply to the i-th subgroup:

$$\begin{cases} \overline{\sigma}_i^r = \int\limits_{D_i} \sigma^r(E) f(E)\, dE \Big/ \int\limits_{D_i} f(E)\, dE; \\ \overline{\sigma}_i = \int\limits_{D_i} \sigma(E) f(E)\, dE \Big/ \int\limits_{D_i} f(E)\, dE; \end{cases} \tag{5}$$

$$P_i = P(\sigma_{i-1} \leqslant \sigma \leqslant \sigma_i) = P(\overline{\sigma}_{i-1}^r \leqslant \sigma^r \leqslant \overline{\sigma}_i^r) = \int\limits_{D_i} f(E)\, dE \Big/ \int\limits_{\Delta E} f(E)\, dE, \tag{6}$$

where f(E) is the spectral function; $P_i$ is the subgroup probability. We can see that $\sum_{i=1}^{I} P_i = 1;\ \overline{\sigma}_i = \sum_r \overline{\sigma}_i^r$. The distribution function of the accumulated probability at the individual points in relation to the section equals

$$F_i = F(\sigma_i) = F(\sigma_i^r) = P(\sigma_{min} \leqslant \sigma \leqslant \sigma_i) = P(\sigma_{min}^r \leqslant \sigma^r \leqslant \sigma_i^r) = \sum_{m=1}^{i} P_m;\quad F(\sigma_0) = F(\sigma_0^r) = 0. \tag{7}$$

The accumulated probability distribution function can be found by other means. Let us choose a number M for some specified reason and then find the value

$$S = \frac{1}{M} \int\limits_{\Delta E} f(E)\, dE. \tag{8}$$

Let us now find a series of energy points

$$E_0,\ E_1,\ \ldots,\ E_i,\ \ldots,\ E_M \tag{9}$$

such that $E_0 = E_{min}$ and $E_i$ is determined by the series of solutions to the equation

$$\int\limits_{E_{i-1}}^{E_i} f(E)\, dE = S, \tag{10}$$

where i = 1, ..., M.

Let us say that series (9) generates a system of equally probable intervals. It is clear that the average section in the i-th interval will be equal to

$$\bar{\sigma}_i = \frac{1}{S}\int_{E_{i-1}}^{E_i} \sigma(E) f(E)\, dE;$$

$$\bar{\sigma}_i^r = \frac{1}{S}\int_{E_{i-1}}^{E_i} \sigma^r(E) f(E)\, dE,$$

where i = 1, ..., M. Let us arrange series (11) in ascending order:

$$\bar{\sigma}_1 \leqslant \bar{\sigma}_2 \leqslant \ldots \leqslant \bar{\sigma}_{j-1} \leqslant \bar{\sigma}_j \leqslant \bar{\sigma}_{j+1} \leqslant \ldots \leqslant \bar{\sigma}_M. \tag{13}$$

Let us reduce series (12) in accordance with series (13). Series (12) will also be progressive when the conditions listed earlier are satisfied. The accumulated probability distribution function at points $\bar{\sigma}_j$ and $\bar{\sigma}_j{}^r$ equals

$$F(\sigma_0 = \sigma_{\min}) = F(\sigma_0^r = \sigma^r{}_{\min}) = 0;$$

$$F_j = P(\sigma_{\min} \leqslant \sigma \leqslant \bar{\sigma}_j) = P(\sigma_{\min}^r \leqslant \sigma^r \leqslant \bar{\sigma}_j^r) = j/M;$$

$$j = 1, \ldots, M, \tag{14}$$

where $\sigma_{\min}$ and $\sigma_{\min}^r$ are the minimum whole and partial sections in interval ΔE.

The Utilization of Data in Monte-Carlo Calculations. The information obtained in calculations by the Monte-Carlo method can be used in two ways: by generating average values or by generating sections as functions of the accumulated probability. The average values of the whole and partial sections can be calculated in the form of a set of equally probable values by means of the formula

$$\frac{1}{N}\,\bar{\sigma}_l^r = \bar{\sigma}_m^r P_m \left(F_m - \frac{l-1}{m}\right)(F_m - F_{m-1}) + \sum_{i=m+1}^{k} \bar{\sigma}_i^r P_i + \bar{\sigma}_{k+1}^r P_{k+1}(l/N - F_k)/(F_{k+1} - F_k), \tag{15}$$

where $\bar{\sigma}^r{}_\gamma$ is the whole section, scattering section, capture section, and fissure section (if applicable) that are equally probable over the interval ΔE; $\gamma$ is the number of equally probable sections in the progressive series; N is the number of equally probable sections; m and k are found in accordance with the condition $(l-1)/N \leqslant F_h \leqslant l/N$, $m = \min h$, $k = \max h$.

If we are obtaining the values of series (12), and M is a multiple of N, then the equally probable sections can be determined as the arithmetic means of W values:

$$\bar{\sigma}_l^r = \frac{1}{W}\sum_{i=(l-1)W+1}^{lW} \bar{\sigma}_i^r, \quad W = M/N. \tag{16}$$

More accurate results can be achieved by generating sections with respect to the distribution of probability intervals. To avoid having to store the values of the distribution functions of all the points obtained during the calculation in the memory of a computer, we propose specifying only certain points throughout the section, and employing either interpolation or a polynomial approximation to the curve between these chosen points. In general, we can also avoid storing the values of functions, if the sections are specified at points that correspond to the values of the distribution function

$$F_l = (l-1)/N \quad \text{for } l = 1, \ldots, N+1.$$

In this case, the probability is 1/N that a neutron in region ΔE will have a section in the interval from $\sigma_\gamma{}^r$ to $\sigma^r{}_{\gamma+1}$ during the generation. Within this interval, we can assume that the section is distributed uniformly, i.e., a linear interpolation of F(σ) between the points $\sigma_\gamma{}^r$ and $\sigma^r{}_{\gamma+1}$ is valid.

The proposed method has been realized in a FORTRAN-IV program for a type ES-1030 computer. The program employed the data from libraries [4, 5].

LITERATURE CITED

1. L. Levitt, Nucl. Sci. Eng., 49, 450 (1972).
2. M. N. Nikolaev and V. V. Filippov, At. Energ., 15, 493 (1963).
3. V. F. Khokhlov and M. N. Nikolaev, in: Problems of Nuclear Science and Technology, Series Nuclear Constants, No. 8, Part 2 [in Russian], Atomizdat, Moscow (1972), p. 119.
4. K. Parker, Report AWRE 0-70/63 (1963).
5. R. Howerton, Report UCID-16376 (1973).

# HELIUM BLISTERING AND HYDROGEN ABSORPTION BY PT-7M AND PT-3V TITANIUM ALLOYS

V. M. Gusev, M. I. Guseva,
E. S. Ionova, N. G. Lemke,
V. I. Syshchikov, P. A. Fefelov,
B. B. Chechulin, and O. I. Chelnokov

UDC 539.12.04:621.039.616

One of the main physical processes responsible for the erosion of the first wall in tokamak devices is that of sputtering of the wall material by ions (or atoms) of hydrogen and helium isotopes.

In the energy range of interest low values of the coefficient of sputtering by light ions are characteristic of titanium [1, 2], which is a component of a number of promising materials for the first wall of fusion reactors or for coating it [3]. It was established earlier [4] that when titanium is bombarded with high-energy $D^+$ ions there is anomalously deep penetration of the deuterium into the titanium and embrittlement of the surface layer. It was also found that $TiH_2$ is formed in the process of ion bombardment [5, 6]. Titanium alloys have practically the same sputtering coefficients as titanium does [7] while differing favorably in respect to mechanical properties. In particular, titanium alloys with aluminum and zirconium (PT-7M) and with aluminum and vanadium (PT-3V) are characterized by high strength and plasticity at an elevated temperature. Saturation with hydrogen at $T \geq 300°C$ results in the formation of a solid solution and does not cause embrittlement of the alloys [8]. These alloys possess satisfactory resistance to neutron irradiation and also have the necessary technological properties. In the present paper we give the results of investigations both on hydrogenation of PT-7M and PT-3V alloys during irradiation with $H^+$ ions with an energy of 10 keV at a temperature of about 120 and 300°C as well as on the helium blistering of these alloys.

Specimens of PT-7M and PT-3V alloys ($30 \times 30 \times 17$ mm) were irradiated with 10-keV $H^+$ ions in an ILU-1 ion accelerator [9] at 120 and 300°C until a dose of $10^{18}$-$3 \cdot 10^{20}$ ion·cm$^{-2}$ was attained. As a control, an identical specimen screened from the beam by diaphragms was mounted along with the irradiated specimen in the same holder. The content of the hydrogen introduced was determined by spectral analysis of both surfaces of the irradiated and control specimens. The hydrogen concentration in the original specimens was 0.003-0.004 wt.%.

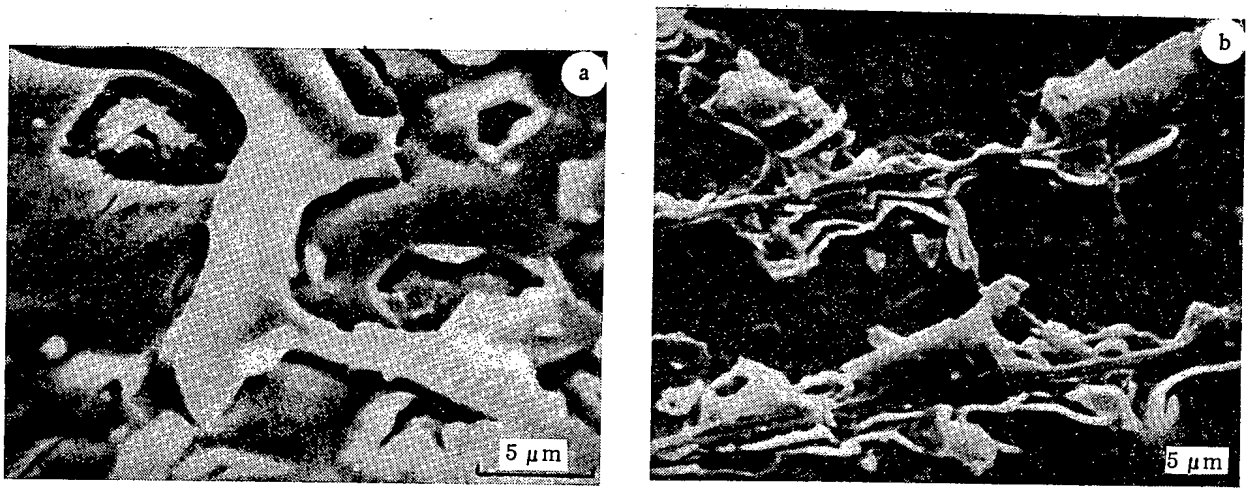


Fig. 1. Surface of PT-3V (a) and PT-7M (b) titanium alloys after irradiation with 100-keV $He^+$ ions at dose of $6 \cdot 10^{18}$ cm$^{-2}$ ($T_{irr} = 120°C$).

Translated from Atomnaya Énergiya, Vol. 48, No. 3, pp. 182-183, March, 1980. Original article submitted April 23, 1979.

 0038-531X/80/4803-0208$07.50 

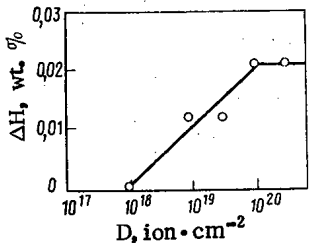


Fig. 2

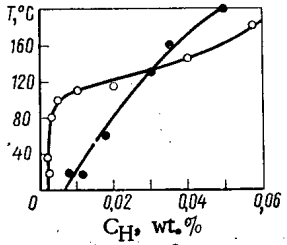


Fig. 3

Fig. 2. Dependence of hydrogen content in PT-7M alloy on dose of irradiation with 10-keV $H^+$ ions at 120°C.

Fig. 3. Limiting solubility of hydrogen in PT-7M (○) and PT-3V (●) alloys at various temperatures.

The microstructure of the transverse microsection was studied with an optical microscope in polarized light. The surface of the targets for studying helium blistering was polished mechanically and chemically. The topography of the surface of the targets after irradiation was examined in a Stereoskan-180 scanning electron microscope.

Figure 1 shows the topography of PT-3V and PT-7M alloys after irradiation with $He^+$ ions. The number of layers scaled off was 6 and 3 for PT-3V and PT-7M, respectively, which gave an erosion rate of 0.1 and 0.7 atom/ion, respectively, and attested to the decisive effect of the alloying additives introduced.

The microstructure of the transverse microsection of PT-7M irradiated with $H^+$ ions under various conditions contains clearly visible titanium hydride precipitates, which are arranged primarily along grain boundaries. Comparison of the microstructures indicates an anomalously deep penetration of hydrogen ions into the titanium. At a dose of $3\cdot10^{19}$ ion·$cm^{-2}$ hydrides are present in a layer with a thickness of 0.35-0.4 mm and at a dose of $10^{20}$ ion·$cm^{-2}$ they are distributed over the entire cross section of the specimen. The observed depth of hydrogen penetration is roughly $10^4$ times the range of the bombarding 10-keV ions, which apparently is attributable to radiation-stimulated diffusion. After irradiation at 300°C the structure of the alloy displays only single hydride precipitates arranged over the grain boundaries near the irradiated surface.

The results of spectral analyses to determine the quantity of implanted hydrogen when $T_{irr} = 120°C$ are given in Fig. 2. The maximum hydrogen concentration of 0.021 wt.% corresponds to a capturing coefficient of 0.93, the hydrogen being distributed approximately uniformly over the cross section of the specimen. When the dose is increased to $3\cdot10^{20}$ ion·$cm^{-2}$, the metal is observed to be saturated with hydrogen, which is in agreement with data on the solubility of hydrogen in the alloy studied (Fig. 3). At $T_{irr} = 300°C$ the hydrogen concentration in the alloy decreases and at a dose of $10^{20}$ ion·$cm^{-2}$ about 60% of the implanted hydrogen leaves the target as the result of thermal diffusion (diffusion coefficient in PT-7M at 300°C is $5\cdot10^{-8}$ $cm^{-2}\cdot sec^{-1}$).

The alloy PT-3V was less inclined to interact chemically with hydrogen. At $T_{irr} = 120°C$ hydride precipitates can be detected only in individual specimens and at 300°C there are practically no hydrides. When PT-3V was irradiated with $H^+$ ions at 300°C no cracking or embrittlement of the surface, which are characteristic of titanium [4, 5], were observed up to a dose of $10^{20}$ ion·$cm^{-2}$. The surface relief formed is typical of sputtering of a polycrystal by high doses of high-energy ions. This allows Ti—Al—V to be considered as a promising alloy for use as a coating on the first wall and the divertor of fusion reactors.

The authors express their gratitude to V. V. Orlov for his constant interest in the work.

LITERATURE CITED

1. M. Guseva and Yu. Martinenko, J. Nucl. Mater., 63, 241 (1976).
2. D. Mattox and D. Sharp, Sand 78-1029 (1978).

3. V. M. Gusev et al., Preprint IAÉ-2545, Moscow (1975).
4. O. Ionts and R. Strehlow, J. Appl. Phys., 33, 2902 (1962).
5. J. Bohdansky et al., J. Nucl. Mater., 63, 1976 (1976).
6. G. McCracken et al., Brit. J. Appl. Phys., 18, 919 (1967).
7. K. Gusev et al., in: Proc. Seventh Int. Conf. on Atomic Collisions in Solids, Moscow (1977), pp. 1, 100.
8. I. V. Gorynin et al., in: Proc. All-Union Conf. on Engineering Problems of Fusion Reactors [in Russian], NIIÉFA, Leningrad (1977), p. 187.
9. V. M. Gusev et al., Prib. Tekh. Eksp., 4, 19 (1969).

# ENERGY CHARACTERISTIC OF SILICON NEUTRON ACCIDENT DOSIMETERS

V. V. Golub

UDC 539.12.08

Experimental investigations of the effect of monoenergetic neutrons on MP 111 and MP 115 silicon transistors and the results reported in [1-4] show (Figs. 1, 2) that the sensitivity of a silicon neutron detector is proportional to the neutron d-kerma — the component of the specific neutron kerma related to the production of structural defects in silicon, i.e.

$$s(E_n) = md(E_n),$$

where m is a proportionality factor.

The function $s(E_n)$ fluctuates considerably. It does not vary with neutron energy in exactly the same way as the specific neutron tissue kerma $k(E_n)$, but does show the same general trend. Normalization of $s(E_n)$ and $k(E_n)$ shows that an attempt to determine an accident dose by silicon detectors will inevitably overestimate the contribution of neutrons of one energy and underestimate the contribution of neutrons of another energy. This means that the possibility of measuring an accident dose with silicon devices, as noted in the literature (e.g. in [1]), is feasible only for sufficiently broad neutron spectra. Since the overestimates and underestimates cannot completely cancel one another for an arbitrary broad neutron spectrum $\varphi(E_n)$, a systematic error will arise in measuring the dose. The value of the sensitivity s for a neutron spectrum $\varphi(E_n)$ can be related to its specific tissue kerma $k[\varphi(E_n)]$

$$s[\varphi(E_n)] = m\frac{d[\varphi(E_n)]}{k[\varphi(E_n)]}k[\varphi(E_n)] = mMk(\varphi)$$

in terms of a function M, over a range of values of which a quantitative estimate of this error is determined. Sets of neutron spectra compiled specifically to test methods of measuring doses are given in [5, 6]. Judging by the scatter of values of M, it can be estimated with a 95% confidence interval that for the neutron spectra of these sets the error under consideration arising because of the approximate tissue-equivalence of a silicon dosimeter is ±18%. This range will be about 1.5 times smaller if the theoretical [9]

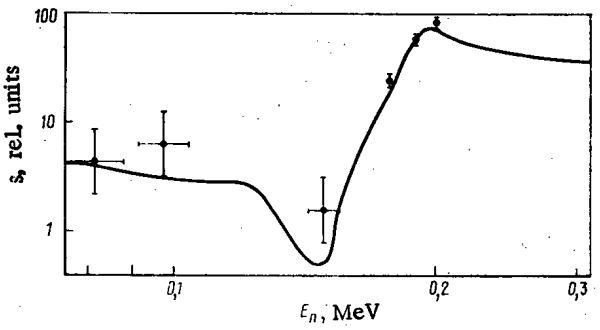


Fig. 1. Sensitivity of silicon neutron accident dosimeter in the energy range <0.3 MeV: ●) experimental data obtained by bombarding MP 111 and MP 115 transistors; ——) function $d(E_n)$. Here and in Fig. 2, 1 rel. unit = 1 keV·b.

Translated from Atomnaya Énergiya, Vol. 48, No. 3, pp. 183-184, March, 1980. Original article submitted May 3, 1979; revision submitted July 10, 1979.

 0038-531X/80/4803-0210$07.50 

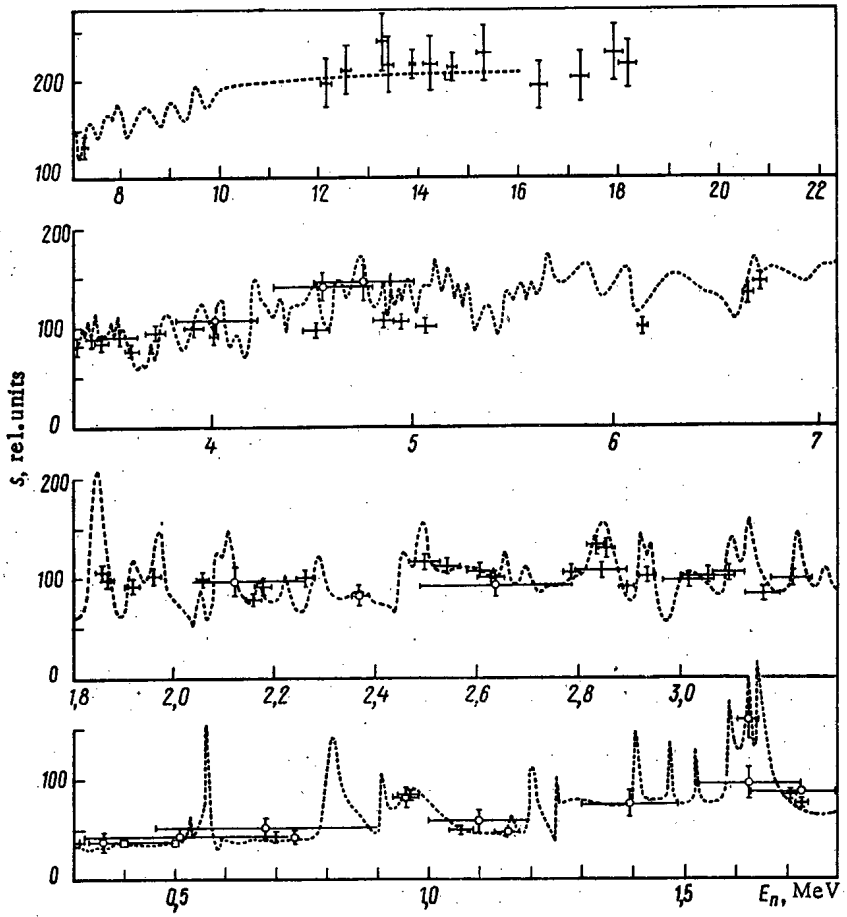


Fig. 2. Sensitivity of silicon neutron accident dosimeter in energy range >0.3 MeV: ...) function $d(E_n)$; +, □, ○) experimental data obtained by bombarding MP 111 and MP 115 transistors, high-frequency transistors [4], and wide-base diiodes [2, 4] respectively.

instead of the experimental [7, 8] values of the energy losses of ions in elastic atomic collisions are used to calculate the d-kerma.

Such an error is substantially smaller than the total error admissible in the measurement of an accident dose [6]. This is the basis for assuming that in many cases a silicon accident dosimeter is tissue-equivalent to a good approximation.

LITERATURE CITED

1. V. I. Shashkin and Yu. V. Kondratenkov, At. Tekh. Rubezhom, No. 6, 35 (1977).
2. R. Speers, IEEE Trans. Nucl. Sci., NS-15, No. 5, 9 (1968).
3. J. Lohkamp and J. McKenzie, IEEE Trans. Nucl. Sci., NS-22, No. 6, 2319 (1975).
4. W. van Amtwerp and J. Youngblood, IEEE Trans. Nucl. Sci., NS-24, No. 6, 2521 (1977).
5. V. V. Golub et al., Preprint FÉI-462, Obninsk (1974).
6. H. Ind and S. Makra, Compendium of Neutron Spectra in Criticality Accident Dosimetry, IAEA, Vienna (1978).
7. A. Grob et al., Nucl. Instrum. Methods, 132, 273 (1976).
8. B. D. Wilkins et al., Nucl. Instrum. Methods, 92, 381 (1971).
9. J. Lindhard et al., K. Dan. Vidensk. Selsk. Mat.-Fys. Medd., 33, No. 10 (1963).

# FEATURES OF STANDARDIZATION OF PLUTONIUM ISOTOPE MIXTURE FORMED IN NUCLEAR POWER REACTORS

R. Ya. Sayapina, V. I. Bad'in,
R. Ya. Sit'ko, and S. V. Petrov

UDC 621.039.8:614.8

Spent fuel elements of power reactors, as is well known, contain a large quantity of β- and γ-emitting fission products and transuranium elements (the plutonium build-up may come to about 10 kg per ton of nuclear fuel). Returning the uranium and plutonium to the power cycle after reprocessing of spent fuel elements is one of the important conditions for the future development of nuclear power. A great deal of practical experience has been accumulated throughout the world in ensuring and monitoring radiation safety during work with plutonium. However, the specific isotopic composition of the plutonium which builds up in fuel elements significantly changes the traditional approach to the evaluation of the radiation hazard from that radionuclide.

It is well known that with an increase in the degree of burn-up of the nuclear fuel the mixture of plutonium isotopes becomes richer in heavy isotopes, especially $^{241}$Pu, which is a low-energy β-emitter with 1870 times the activity of $^{239}$Pu per unit weight. The $^{241}$Pu content in fuel elements may amount to 10-12 wt.% [1, 2]. The radiotoxicity of the composition of the plutonium isotope mixture formed in a thermal reactor at a burn-up of 30 (MW·day)/kg (see Table 1) is determined by both $^{241}$Pu and the α-active isotopes of plutonium. When this mixture enters the respiratory organs there is one unit of maximum permissible intake (MPI) of $^{241}$Pu (4) per unit of MPI of the sum of α-active plutonium isotopes.

It thus follows that monitoring of the intake of plutonium isotopes into the body, which is traditionally done according to the α-active radionuclides, is inadequate for plutonium extracted from fuel elements. In addition to this, measurement of the activity of low-energy β-radiation ($E_{av} \approx 5$ keV) against the background of α-radiation and residual fission-fragment products entails certain methodological difficulties.

In the present paper we propose a method which makes it possible to avoid continuous monitoring of β-activity and to compensate its value by lowering the MPI of α-active plutonium isotopes by a factor K, proceeding from the familiar formula for the mixture:

$$\mathrm{MPI}_m = 1/\Sigma \frac{P_i}{\mathrm{MPI}_i}, \quad (1)$$

where $\mathrm{MPI}_m$ is the maximum permissible intake of the mixture of radionuclides; $P_i$, the relative content of the i-th radionuclide in the mixture with respect to activity, in fractions; and $\mathrm{MPI}_i$, the maximum permissible intake of the i-th radionuclide.

Rearranging Eq. (1), we get a relation from which we can calculate the value of K:

$$\frac{\mathrm{MPI}_\alpha}{\mathrm{MPI}_m P_\alpha} = 1 + \frac{\mathrm{MPI}_\alpha P_\beta}{\mathrm{MPI}_\beta P_\alpha} = K. \quad (2)$$

TABLE 1. Isotopic Composition of Plutonium at Burn-Up of 30 (MW·day)/kg in Thermal Reactors of Atomic Power Plant

| Content | $^{238}$Pu | $^{239}$Pu | $^{240}$Pu | $^{241}$Pu | $^{242}$Pu |
|---|---|---|---|---|---|
| By weight, g/kg of fuel | 0,11 | 5,5 | 2,64 | 1,16 | 0,45 |
| By activity, Ci/kg of fuel (Bc/kg) | 1,85 ($6{,}85\cdot10^{10}$) | 0,336 ($1{,}24\cdot10^{10}$) | 0,6 ($2{,}22\cdot10^{10}$) | 132 ($488{,}4\cdot10^{10}$) | $1{,}75\cdot10^{-3}$ ($6{,}48\cdot10^{7}$) |

Translated from Atomnaya Énergiya, Vol. 48, No. 3, p. 185, March, 1980. Original article submitted May 18, 1979; revision submitted July 3, 1979.

 0038-531X/80/4803-0212$07.50 

Here, $MPI_\alpha$ is the maximum permissible intake, as regulated by radiation safety standard NRB-76, for the sum of α-active isotopes $^{238}Pu$, $^{239}Pu$, $^{240}Pu$, and $^{242}Pu$; $MPI_m P_\alpha$, the sought value of the MPI for the α-active fraction of the mixture of plutonium isotopes; $P_\alpha$, the relative contribution of the sum of α-active isotopes of plutonium, in fractions; $MPI_\beta$, the maximum permissible intake of $^{241}Pu$ as regulated by NRB-76; and $P_\beta$, its relative contribution.

It follows from Eq. (2) that in order to obtain the sought value of MPI for the α-active fraction of the mixture of plutonium isotopes the value of $MPI_\alpha$ as regulated by radiation safety standards must be reduced by a factor of K. For soluble compounds of plutonium the MPI for each α-active isotope varies slightly, from $2.4 \cdot 10^{-3}$ μCi/yr (88.8 Bc/yr) to $2.1 \cdot 10^{-3}$ μCi/yr (77.7 Bc/yr). For the mixture presented in Table 1 the MPI is $2.28 \cdot 10^{-3}$ μCi/yr (84.4 Bc/yr) while for $^{241}Pu$ it is 0.11 μCi/yr (4070 Bc/yr) [3] and K can be found from

$$K = 1 + 0.02\,(\beta/\alpha), \tag{3}$$

where $\beta/\alpha = P_\beta/P_\alpha$ is the ratio of the β-activity of $^{241}Pu$ to the α-activity of the sum of plutonium isotopes; 0.02 is the value of the ratio $MPI_{\Sigma\alpha}$ ($^{238-242}Pu$)/$MPI_\beta$ ($^{241}Pu$).

Bearing in mind that the ratio of the permissible intake of the sum of active plutonium isotopes to that of $^{241}Pu$, equal to 0.02, depends little on the isotopic composition of the plutonium (the error in the determination of the value of 0.02 does not exceed 10%), Eq. (3) can be used for any mixture of plutonium isotopes.

For the mixture of plutonium isotopes given in Table 1,

$$K = 1 + 50 \cdot 0{,}02 = 2, \tag{4}$$

i.e., safety conditions will be maintained if the actual intake of α-active plutonium isotopes is half the value of the MPI as regulated for them by the radiation safety standards.

LITERATURE CITED

1. N. S. Babaev, N. L. Poznyakov, and D. F. Strelkov, At. Energ., 45, No. 4, 267 (1978).
2. D. Deonogi, Nucl. Technol., 18, 80 (1973).
3. Radiation Safety Standards NRB-76 [in Russian], Atomizdat, Moscow (1978).

# PHYSICAL ASPECTS OF INJECTING SYSTEM FOR LARGE TOKAMAKS AND OPEN TRAPS

A. I. Krylov, V. V. Kuznetsov, and N. N. Semashko

UDC 621.039.647

In recent years an intensive study has been made of the possibility of constructing thermonuclear reactors with injection, in which the thermonuclear reaction would be sustained by the introduction of high-power streams of atoms (tens and hundreds of MW). Several schemes for reactor-tokamaks designed for injection have been proposed [1]. One of them is based on the fact that until they are thermalized, injected high-energy deuterons promote thermonuclear reactions as the result of collision with ions of the tritium plasma-target (two-component reactor) [2]. The optimum of the particle energy lies in the range 200-400 keV. In another scheme, injection can be used to create in the reactor conditions for igniting the thermonuclear reaction [3]. The large geometrical dimensions of the tokamaks necessitates the use of beams with a long range for the particles injected into the plasma, i.e., necessitates injection of high-energy atoms (400 keV or more).

The transformation of negative ions with such an energy into neutral particles occurs with an efficiency $\eta = 0.6$-$0.8$, depending on the type of target [4, 5], whereas the efficiency of transformation of positive ions into atoms at the same energy is substantially lower. Therefore, the energy efficiency of an injector using negative ions at high energies is substantially higher than one with positive ions (Fig. 1).

Two methods have been developed for obtaining powerful beams of negative ions: by extracting negative ions directly from gas-discharge plasma as, e.g., in surface-plasma sources [6, 7], and by double recharging of positive ions in alkali–metal vapors [8, 9]. An unquestionable advantage of the first method is the great simplicity of the scheme. To date, however, ion beams have been obtained in pulses no more than milliseconds in length. With the second method the pulse duration has been extended to seconds and there are not difficulties of a fundamental nature which would hinder the construction of stably operating injectors whereas the prospects of the first method are not as bright.

The general scheme of an injector of fast deuterium atoms with an energy of 400-600 keV incorporates a source of positive low-energy deuterium ions (5-10 keV), a charge-exchange target for obtaining negative ions, a system for additionally accelerating the negative ions to the required energy, and a target for transforming the negative ions into atoms. The comparatively low energy of the positive ions is due to the fact that the yield of negative ions is maximum at this energy. For targets of various alkali metals this yield reaches 0.12-0.25 [10, 11].

Figure 2 shows the diagram of the module of an injector using negative deuterium ions. Several separate modules are combined into an injector with a total power of 30-40 MW in the atomic beams. The source produces and shapes a beam of positive ions with a current of the order of 100 A and a current density of up to 0.25 A/cm$^2$. As the first charge-exchange target use was made of a supersonic jet of sodium vapor [8] in which the yield of negative ions is 0.12 for a beam of $D_1^+$ with an ion energy of $\sim$7 keV. When account is taken of the

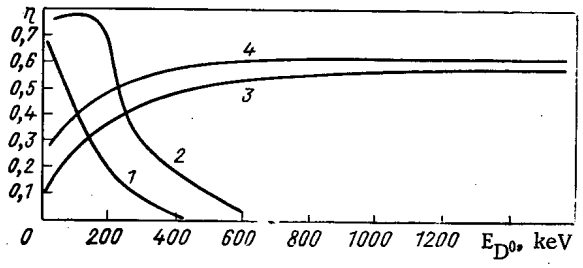


Fig. 1. Efficiency of deuterium-atom injector vs energy: 1) injector with positive ions; 2) injector with positive ions and energy recuperation (90% efficiency); 3, 4) injector using negative ions obtained by recharging in cesium and sodium, respectively.

Translated from Atomnaya Énergiya, Vol. 48, No. 3, pp. 186-187, March, 1980. Original article submitted May 18, 1979.

 0038-531X/80/4803-0214$07.50 

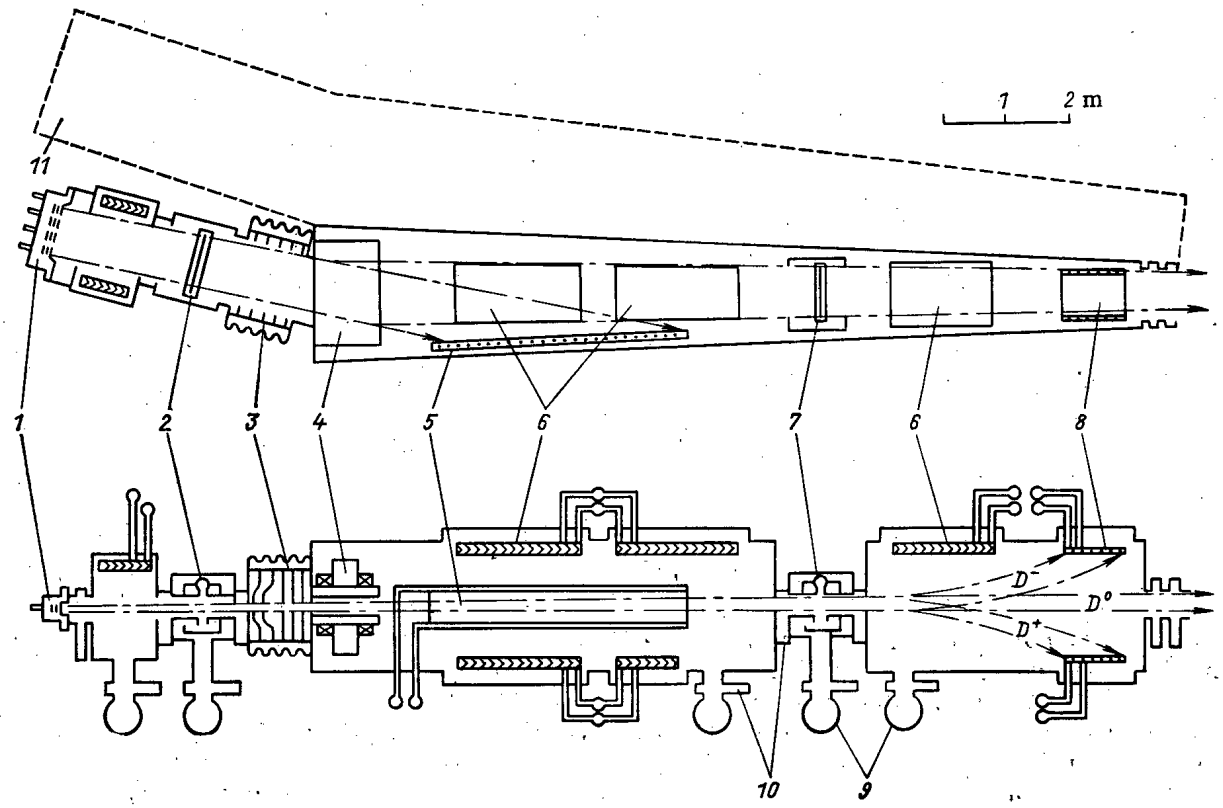


Fig. 2. Module of injector of deuterium atoms with energy of 400-600 keV: 1) source of positive ions; 2) sodium charge-exchange target; 3) system for additional acceleration; 4) bending magnet; 5) receiver of 10-keV atoms; 6) cryogenic evacuation panels; 7) lithium stripping target; 8) receivers of 400-600-keV ions; 9) vacuum fore-pumping system; 10) vacuum locks; 11) adjacent module of injector.

$D_2^+$ and $D_3^+$ ions which are present in the beam and which, upon traversing the target, dissociate into ions of lower energy and undergo charge exchange, the overall yield of negative ions reaches 0.18 (Fig. 3). The supersonic jet also serves as a vacuum lock, setting up a pressure drop between the regions in which positive and negative ions are moving, and partially pumps off the gas flowing from the source.

The system for additional acceleration, placed inside a high-voltage insulator, is a series of heated electrodes. The potential distribution over the electrodes, on the one hand, ensures high-voltage strength and, on the other hand, creates as long-focus a system as possible.

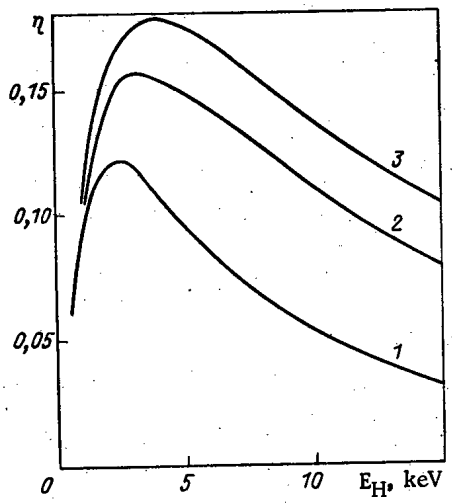


Fig. 3. Yield of negative ions vs energy during charge exchange of $H^+$ ion beams with various component compositions: 1) $H_1^+$ = 100%; 2) $H_1^+$ = 70%, $H_2^+$ = 20%, $H_3^+$ = 10%; 3) $H_1^+$ = 60%, $H_2^+$ = 20%, $H_3^+$ = 20%.

A magnet, installed after the system of additional acceleration, turns the beam of negative ions through a small angle and directs it at the entrance aperture of the thermonuclear device. The neutral particles formed in the target are admitted by a special current receiver. The pressure of the residual gas in this region should not exceed $1.33 \cdot 10^{-3}$ Pa so as not to cause large losses of the beam of $D^-$ ions. This space should also be shielded against scattered magnetic fields of the device.

If the target for stripping negative ions is one of the best developed targets based on alkali-metal vapor, then it is desirable to choose lithium for the working substance since it ensures the highest yield of atoms ($\sim$0.65) [11] and a very low loss of vapor such that the thermonuclear device will have the minimum quantity of impurities with low charge. The remaining charged components of the beam consist of roughly equal numbers of positive and negative charged particles. The charged components can be removed from the atomic beam both by the magnetic scattering field from the current of the plasma filament of the tokamak and by a special magnetic field. The efficiency of the injector can increase sharply if a plasma target is used [5].

## LITERATURE CITED


1. D. Jassby, Nucl. Fusion, 17, 309 (1977).
2. F. Furth et al., Phys. Rev. Lett., 32, 1176 (1974).
3. L. A. Artsimovich, Nucl. Fusion, 12, 215 (1972).
4. B. A. D'yachkov, Zh. Tekh. Fiz., 38, 1250 (1968).
5. G. I. Dimov et al., Yadernyi Sintez, 15, 551 (1975).
6. G. Dimov, in: Proc. Symp. Production of Neutral and Negative Hydrogen Ions and Beams, Brookhaven (1977), BNL-50727, p. 170.
7. K. Prelec et al., in: Proc. Symp. Production of Neutral and Negative Hydrogen Ions and Beams, Brookhaven (1977), BNL-50727, p. 111.
8. N. Semashko et al., in: Proc. Symp. Production of Neutral and Negative Hydrogen Ions and Beams, Brookhaven (1977), BNL-50727, p. 170.
9. E. Hooper, in: Proc. Symp. Production of Neutral and Negative Hydrogen Ions and Beams, Brookhaven (1977), BNL-50727, p. 161.
10. B. A. D'yachkov and V. N. Zimenko, At. Energ., 24, No. 1, 18 (1968).
11. E. Hooper, UCRL-81830 (1978).
12. N. N. Semashko et al., in: Proc. Second Conf. Engineering Problems of Thermonuclear Fusion, Vol. II, Leningrad (1977).

# POSSIBLE CONTROL OF NEUTRON FLUX BY MOLECULAR LAYERED COMPOUNDS

I. G. Gverdtsiteli, A. G. Kalandarishvili, S. D. Krivonosov, V. A. Kuchukhidze, and B. A. Mskhalaya

UDC 621.039.515

In reactor operation it is necessary to ensure the required neutron spectrum and the value and profile of the energy distribution. Many technical solutions have been proposed for controlling the neutron flux in a reactor, among them, controlling the reactor by means of channels filled with neutron absorbers of substances in various states of aggregation [1-5].

In the present paper we consider the possibility of employing channels filled with neutron-transparent layered structures with a neutron-absorbing substance whose content is determined by the constant of a two-phase equilibrium reaction which is temperature-dependent. The layered compound is formed when various elements or chemical compounds interact with a substance which has a layered structure, such a pyrolytic graphite [6] or the dichalcogenides of transition metals [7].

The possibility in principle of realizing this method is shown in Fig. 1. The device [8, 9] constitutes two coaxial cylinders of stainless steel. The inner cylinder 1, which is connected with reservoir 2 filled with absorbing material 3, contains block 4 of the neutron-transparent matrix of a layered compound with a particular orientation of the crystallographic axes, held by spring 5 in the direction of expansion. The second cylinder 6 holds electric heaters 7, 8 for controlling the temperature of the layered compound and the absorbing material. The length of the ampul is determined by the height of the reactor core 9 while the diameter can vary within wide limits.

Let us evaluate how effectively this device functions when use is made of a layered compound based on pyrolytic graphite with alkali metals. The choice of layered compound is dependent upon good knowledge of the parameters of the given layered compounds, which facilitates calculations. As the alkali metal is introduced into the pyrolytic graphite, the thermal-neutron absorption cross section of the layered compound increases monotonically in proportion to the weight concentrations of the alkali metal in the graphite; this provides continuously variable control of the neutron flux.

Let us consider the case when the orientation of the crystallographic c axis of the pyrolytic graphite, with a thickness of 1 cm, is parallel to the height of the reactor core. The neutron-flux attenuation factor was calculated from [10]

$$\Phi/\Phi_0 = \gamma = \exp(-\Sigma_a d), \quad (1)$$

TABLE 1. Neutron-Flux Attenuation Factor of Layered Compound of Pyrolytic Graphite with Alkali Metal

| Compound | A | | B | | C | |
|---|---|---|---|---|---|---|
| | Cs | $^{40}$K | Cs | $^{40}$K | Cs | $^{40}$K |
| $C_8Me$ | 0,80 | 0,55 | 0,67 | 0,38 | 0,83 | 0,57 |
| $C_{10}Me$ | 0,83 | 0,62 | 0,73 | 0,48 | 0,83 | 0,57 |
| $C_{12}Me$ | 0,86 | 0,67 | 0,77 | 0,53 | 0,83 | 0,57 |
| $C_{24}Me$ | 0,91 | 0,78 | 0,88 | 0,72 | 0,91 | 0,75 |
| $C_{36}Me$ | 0,93 | 0,83 | 0,92 | 0,81 | 0,94 | 0,83 |
| $C_{48}Me$ | 0,94 | 0,86 | 0,93 | 0,85 | 0,95 | 0,87 |
| $C_{60}Me$ | 0,95 | 0,89 | 0,95 | 0,88 | 0,96 | 0,89 |
| $C_{72}Me$ | 0,96 | 0,91 | 0,96 | 0,90 | 0,97 | 0,91 |

Translated from Atomnaya Énergiya, Vol. 48, No. 3, pp. 187-189, March, 1980.

0038-531X/80/4803-0217$07.50 

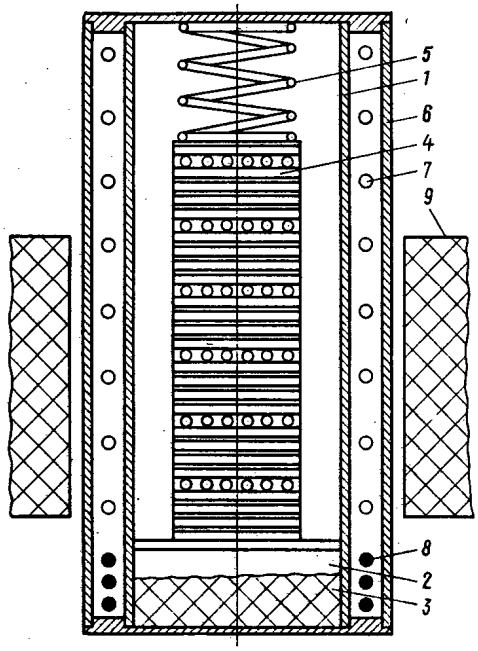


Fig. 1. Scheme of the device of a channel with a layered compound for controlling a neutron flux.

where $\Phi_0$ and $\Phi$ are the neutron fluxes in front of and behind the layered compound; $\gamma$, the flux attenuation factor; $\Sigma_a$, the macroscopic cross section for absorption of thermal neutrons by the layered compound, $cm^{-1}$; and d, the thickness of the layered compound, cm. Let us suppose that when the pyrolytic graphite interacts with the alkali metal the latter is homogeneously distributed over the volume of the layered compound. Then [10]

$$\Sigma_a = \frac{\rho_a}{100}\left(\frac{\sigma_1 N}{A_1}\eta_1 + \frac{\sigma_2 N}{A_2}\eta_2\right), \quad (2)$$

where $\rho_a$ is the density of the given phase of the layered compound, $g/cm^3$; $\sigma_1$ is the microscopic absorption cross section of the graphite, 3.73 mb; $A_1$ is the atomic weight; $\eta_1$ is the weight content of pyrolytic graphite, %; $\sigma_2$, $A_2$, and $\eta_2$ are the analogous characteristics of the alkali metal, $\sigma_2 = 28$ b for Cs and 70 b for $^{40}K$; and N is Avogadro's number. The density and weight contents are determined by the phase of the layered compound.

The attenuation factors for layered compounds of pyrolytic graphite with cesium and the isotope $^{40}K$ for various stable phases are given in part A of Table 1. If the matrix of the layered compound is made up of plates with crystallographic c axis perpendicular to the height of the reactor core, the neutron-flux attenuation factor can be evaluated either with the assumption of homogeneity (see part B of Table 1) or with the assumption of heterogeneity. In the latter case the layered compound is in the form of two plates: pyrolytic graphite with a thickness of 1 cm and a plate of absorbing material of variable thickness, equal to the difference between the values of the thicknesses of the layered compound and the matrix.

The attenuation factors in the heterogeneous approach, which were calculated from a formula similar to Eq. (1), are given in part B of Table 1. The maximum attenuation factor of the layered compound with a matrix of unit thickness for the system pyrolytic graphite—alkali metal is 0.38 and is realized by using the isotope $^{40}K$. Layered compounds of pyrolytic graphite with rubidium isotopes, $^{39}K$, and $^{41}K$ give an attenuation factor of more than 0.99 in all cases considered.

An increase in the control efficiency can be attained by using layered compounds of pyrolytic graphite with cadmium bromide [11] and boron chloride [12]. The results of calculations for a layered compound of pyrolytic graphite with cadmium bromide show that when the geometric dimensions are increased by 0.1, 0.2, 0.3, 0.4, and 0.5 cm the attenuation factor is, respectively, 0.017, $3\cdot10^{-4}$, $4\cdot10^{-6}$, $6\cdot10^{-8}$, and $8\cdot10^{-10}$.

It is proposed to try this method of control on the VVR-M reactor.

LITERATURE CITED

1. M. V. Pasechnik et al., Ukr. Fiz. Zh., 7, No. 1, 3 (1962).
2. R. R. Ionaitis and B. N. Tyunin, At. Tekh. Rubezhom, No. 5, 15 (1973).

3. P. T. Potapenko, At. Tekh. Rubezhom, No. 6, 22 (1975).
4. P. T. Potapenko, At. Energ, 44, No. 4, 363 (1978).
5. F. M. Arinkin et al., At. Energ., 45, No. 5, 377 (1978).
6. Yu. M. Novikov and M. E. Vol'pin, Usp. Khim., 40, No. 9, 1569 (1971).
7. L. M. Bulaevskii, Usp. Fiz. Nauk, 116, No. 3, 449 (1975).
8. I. G. Gverdtsiteli et al., Inventor's Certificate No. 658993, Class G21C7/06 (1978).
9. I. G. Gverdtsiteli et al., Inventor's Certificate No. 658992, Class G21C7/06 (1978).
10. L. R. Kimel' and V. P. Mashkovich, Protection against Ionizing Radiations (Handbook) [in Russian], Atomizdat, Moscow (1966).
11. C. Balestreri et al., C. R. Acad. Sci., Ser. C, No. 7, 279 (1974).
12. R. Croft, Research, No. 10, 23 (1957).

# ENERGY DISTRIBUTION OF FAST NEUTRONS IN THE F-1 URANIUM—GRAPHITE REACTOR

V. A. Kanareikin, V. M. Tyryshkin, and V. S. Yuzgin

UDC 621.039.512:45

The first uranium—graphite reactor in Eurasia, the F-1, is now frequently used to produce the special state-standard-unit neutron-flux density [1]. However, a reliable standard neutron-flux density is not the only information needed to solve a number of problems involving the effect of radiation on materials. Actually, the effect on a material of a given flux density of neutrons is determined by their energy distribution. This is why, for example, in calibrating threshold detectors in a reactor in order to employ them later in experiments involving the irradiation of materials it is necessary to take account of the energy spectrum of the neutrons, particularly the fast neutrons, activating the detectors.

Accordingly, the neutron spectrum in the 0.1 to 10 MeV range was calculated in the middle of a channel passing through the center of the F-1 reactor core. This is one of the channels used for the activation of detectors being calibrated. The calculation was performed for a nominal reactor power of 24 kW using a program for solving the adjoint neutron transport equation by the Monte-Carlo method. This program has been successfully used to determine the fast neutron flux density in the MR reactor [2] and in water-cooled water-moderated reactors.

Taking account of certain differences between the calculational model and the actual reactor, the flux density of neutrons with energies above 3 MeV calculated at the center of a horizontal channel of the F-1 reactor is in good agreement with the experimental value of $2.6 \cdot 10^{12}$ neutrons/$m^2 \cdot$sec [1].

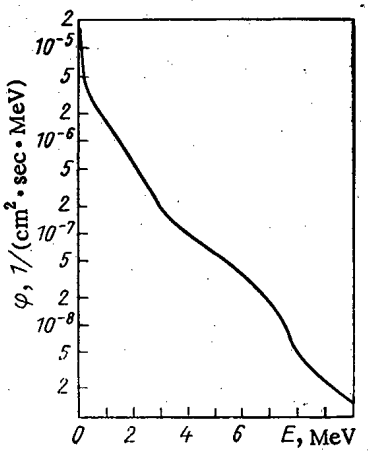


Fig. 1. Differential energy density of neutron flux at center of a horizontal channel of the F-1 reactor. The spectrum is normalized to one neutron with energy above 0.1 MeV produced in the core.

Translated from Atomnaya Énergiya, Vol. 48, No. 3, p. 189, March, 1980. Original article submitted May 28, 1979.

0038-531X/80/4803-0219$07.50 

The differential energy density of the neutron flux is shown in Fig. 1. The standard statistical error does not exceed 2.5% of the calculated values in the 0.1-0.5 MeV neutron energy range, 4% in the 0.5-7.5 MeV range, and 6.5% in the 7.5-10 MeV range.

It is interesting to compare the cross sections for the activation of certain threshold detectors in the standard neutron field of the F-1 reactor and in other reactors, taking account of the fast neutron spectra. Thus, the cross sections for the activation of $^{103}$Rh and $^{115}$In averaged over the spectrum above 0.1 MeV in the F-1 reactor are $3.7 \cdot 10^{-1}$ and $7.3 \cdot 10^{-2}$ b, respectively, while in the MR research reactor [2] analogous values when using rhodium and indium foils as detectors would have to be taken equal to $5.6 \cdot 10^{-1}$ and $1.4 \cdot 10^{-1}$ b.

Thus, detectors calibrated in the F-1 reactor and later used in experiments on the properties of materials performed in the MR reactor can lead to errors of ~40-50% in the estimate of the flux density and fluence of neutrons with energies above 0.1 MeV. It should be noted that the cross sections for the activation of rhodium, averaged over the neutron spectra above 0.8 MeV in the F-1 and MR reactors, are approximately the same ($\sim 9.5 \cdot 10^{-1}$ b). This result agrees with [3].

Both the activation cross sections and the effective cross sections for material damage, averaged over the neutron energy, depend on the spectrum shape. Thus, the cross sections for defect production in iron and zirconium, which are components of the fuel element cladding, averaged over the neutron spectrum above 0.1 MeV in the F-1 reactor, are 4.9 and 3.7 displacements/g, and in the MR reactor 7.2 and 4.7 displacements/g.

LITERATURE CITED

1. É. F. Garapov et al., At. Energ., 42, 286 (1977).
2. V. M. Tyryshkin and V. S. Yuzgin, At. Energ., 43, 289 (1977).
3. R. D. Vasil'ev, E. I. Grigor'ev, and V. P. Yaryna, in: Metrology of Neutron Radiation at Reactors and Accelerators [in Russian], Vol. 1, Standartov, Moscow (1972), p. 200.

# APPROXIMATION OF LIMITING CONTROL IN OPTIMIZATION OF XENON TRANSIENT PROCESSES

V. I. Pavlov and V. D. Simonov

UDC 621.039.562

The trajectory abcd in Fig. 1 illustrates the character of a transient xenon process during three-phase optimal control of reactor power before that power is reduced [1]. The segments ab and cd are the phases of allowable minimum and nominal reactor power, $U_{min}$ and $U_{nom}$. At points b and c the power jumps from $U_{min}$ to $U_b$ and from $U_c$ to $U_{nom}$. Segment bc is the phase of limiting control, during which the power is continuously reduced from $U_b$ to $U_c$ according to a law ensuring that the $^{135}Xe$ concentration is kept at the highest allowed level, which is specified by the curve $X^{(2)} = X_{max}^{(2)}$. Clearly, such limiting control is difficult to implement in practice.

An attempt to approximate continuous control by relay control has been reported [2]. In order to ensure that the duration of the limiting control does not increase by more than 8%, the power has to be switched from nominal to minimum and vice versa at intervals of about 5 min. Such control is hardly simpler than continuous control.

A substantial simplification can be attained by replaced continuous control with piecewise-continuous control, corresponding to the final state of the reactor on the limiting line. Then phases ab and cd of optimal control do not suffer any changes and limiting control will consist in the stepped decrease in power from $U_b$ to $U_c$.

Since the trajectory which emerges from the point b and corresponds to the control $U(t) = U_b$ and the trajectory arriving at point c with the control $U(t) = U_c$ are both tangent to the straight line $X^{(2)} = X_{max}^{(2)}$ at points b and c, respectively, with one-step approximation of the limiting control switching the power from $U_b$ to $U_c$ at the point of intersection of these trajectories prevents the inadmissible over-poisoning of the reactor. Such discussions make it possible to find the trajectory for any number of steps. As an example Fig. 1 schematically shows the trajectory of limiting control approximated by one (blc), two (b234c), and three (b56789c) power steps.

With n steps it is possible to employ, e.g., the following sequence of reactor power control: $U_m = U_b - \frac{U_b - U_c}{n} m$ $(m = 0, 1, \ldots, n)$. The choice of the number of power steps in each concrete situation is determined by the necessary accuracy of approximation. The extension of the phase of limiting control through the replacement of the continuous control

TABLE 1. Extension of Phase of Limiting Control with Stepped Approximation, %

| ρ, % | $U_T/U_{nom}$ | No. of power steps | | | |
|---|---|---|---|---|---|
| | | 1 | 2 | 3 | 4 |
| 0,9 | 0 | 95,2 | 8,2 | 3,0 | 1,8 |
| | 0,1 | 82,3 | 5,4 | 1,9 | 1,2 |
| | 0,2 | 35,7 | 3,2 | 1,4 | 0,9 |
| | 0,3 | 6,6 | 1,5 | 0,8 | 0,4 |
| 1,3 | 0 | 12,2 | 2,5 | 1,1 | 0,6 |
| | 0,1 | 6,3 | 1,2 | 0,7 | 0,3 |
| | 0,2 | 2,1 | 0,5 | 0,2 | 0,1 |
| | 0,3 | 0,8 | 0,2 | 0,1 | < 0,1 |
| 1,7 | 0 | 3,2 | 0,7 | 0,3 | 0,2 |
| | 0,1 | 1,1 | 0,2 | 0,1 | < 0,1 |
| | 0,2 | 0,2 | 0,1 | < 0,1 | < 0,1 |
| | 0,3 | < 0,1 | < 0,1 | < 0,1 | < 0,1 |

Translated from Atomnaya Énergiya, Vol. 48, No. 3, p. 190, March, 1980. Original article submitted June 26, 1979.

0038-531X/80/4803-0221$07.50  

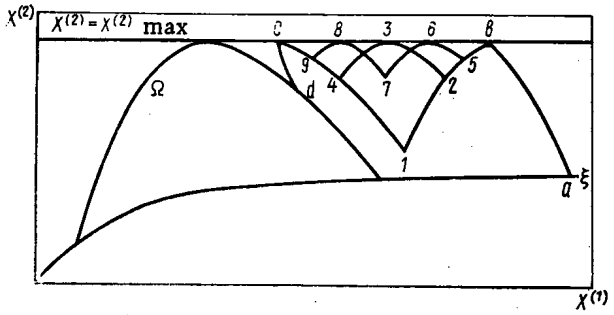


Fig. 1. Variation of iodine and xenon concentration, $X^{(1)}$ and $X^{(2)}$, under three-phase control of reactor power: ξ) curve of equilibrium states; Ω) curve of variation of poisoning for $U(t) = U_T$ (tangent to $X^{(2)} = X_{max}^{(2)}$).

by piecewise-continuous control depends not only on the number of power steps but also on the properties of the reactor, the operational reactivity margin ρ, and the level $U_T$ to which the reactor power should be reduced.

As follows from the data of Table 1, calculated for a reactor of the VVÉR type (water-moderated water-cooled power reactor) [3] with $\rho \geq 0.9\%$ and three power steps, the phase of the limiting control is extended by no more than 3% even when preparations are being made to shut down the reactor. A reactivity margin above 1.5% allows us to confine ourselves to one-stage approximation for this purpose.

LITERATURE CITED

1. A. P. Rudik, Nuclear Reactors and the Pontryagin Maximum Principle [in Russian], Atomizdat, Moscow (1971).
2. A. S. Gerasimov, At. Energ., 44, No. 5, 452 (1978).
3. S. A. Vasil'ev et al., Kernenergie, 21, No. 3, 72 (1978).

# NEW RUSSIAN JOURNALS

## IN ENGLISH TRANSLATION

### BIOLOGY BULLETIN

*Izvestiya Akademii Nauk SSSR, Seriya Biologicheskaya*

The biological proceedings of the Academy of Sciences of the USSR, this prestigious new bimonthly presents the work of the leading academicians on every aspect of the life sciences—from micro- and molecular biology to zoology, physiology, and space medicine.

Volume 7, 1980 (6 issues) . . . . . $195.00

### SOVIET JOURNAL OF MARINE BIOLOGY

*Biologiya Morya*

Devoted solely to research on marine organisms and their activity, practical considerations for their preservation, and reproduction of the biological resources of the seas and oceans.

Volume 6, 1980 (6 issues) . . . . . $115.00

### WATER RESOURCES

*Vodnye Resursy*

Evaluates the water resources of specific geographical areas throughout the world and reviews regularities of water resources formation as well as scientific principles of their optimal use.

Volume 7, 1980 (6 issues) . . . . . $215.00

### HUMAN PHYSIOLOGY

*Fiziologiya Cheloveka*

A new, innovative journal concerned *exclusively* with theoretical and applied aspects of the expanding field of human physiology.

Volume 6, 1980 (6 issues) . . . . . $195.00

### SOVIET JOURNAL OF BIOORGANIC CHEMISTRY

*Bioorganicheskaya Khimiya*

Features articles on isolation and purification of naturally occurring, biologically active compounds; the establishment of their structure, methods of synthesis, and determination of the relation between structure and biological function.

Volume 6, 1980 (12 issues) . . . . . $245.00

### SOVIET JOURNAL OF COORDINATION CHEMISTRY

*Koordinatsionnaya Khimiya*

Describes the achievements of modern theoretical and applied coordination chemistry. Topics include the synthesis and properties of new coordination compounds; reactions involving intraspheral substitution and transformation of ligands; complexes with polyfunctional and macromolecular ligands; complexing in solutions; and kinetics and mechanisms of reactions involving the participation of coordination compounds.

Volume 6, 1980 (12 issues) . . . . . $255.00

### THE SOVIET JOURNAL OF GLASS PHYSICS AND CHEMISTRY

*Fizika i Khimiya Stekla*

Devoted to current theoretical and applied research on three interlinked problems in glass technology; the nature of the chemical bonds in a vitrifying melt and in glass; the structure-statistical principle; and the macroscopic properties of glass.

Volume 6, 1980 (6 issues) . . . . . $145.00

### LITHUANIAN MATHEMATICAL JOURNAL

*Litovskii Matematicheskii Sbornik*

An international medium for the rapid publication of the latest developments in mathematics, this quarterly keeps western scientists abreast of both practical and theoretical configurations. Among the many areas reported on in depth are the generalized Green's function, the Monte Carlo method, the "innovation theorem," and the Martingale problem.

Volume 20, 1980 (4 issues) . . . . . $175.00

### PROGRAMMING AND COMPUTER SOFTWARE

*Programmirovanie*

Reports on current progress in programming and the use of computers. Topics covered include logical problems of programming; applied theory of algorithms; control of computational processes; program organization; programming methods connected with the idiosyncracies of input languages, hardware, and problem classes; parallel programming; operating systems; programming systems; programmer aids; software systems; data-control systems; IO systems; and subroutine libraries.

Volume 6, 1980 (6 issues) . . . . . $115.00

### SOVIET MICROELECTRONICS

*Mikroelektronika*

Reports on the latest advances in solutions of fundamental problems of microelectronics. Discusses new physical principles, materials, and methods for creating components, especially in large systems.

Volume 9, 1980 (6 issues) . . . . . $160.00

**Send for Your Free Examination Copy**

PLENUM PUBLISHING CORPORATION, 227 West 17th Street, New York, N.Y. 10011
In United Kingdom: 88/90 Middlesex Street, London E1 7EZ England
Prices slightly higher outside the U.S. Prices subject to change without notice.